First measurement of the $K^+ \to \pi^+ \nu\bar{\nu}$ decay with the NA62 experiment at CERN

Dissertation
zur Erlangung des Grades

"Doktor der Naturwissenschaften"

am Fachbereich Physik, Mathematik und Informatik
der Johannes Gutenberg-Universität
in Mainz

Radoslav Ivanov Marchevski
Geboren in Svishtov, Bulgaria

Mainz 2018

Date of the exam: 19.02.2019

Preface

The measurement presented here has been accepted for publication in a peer-reviewed journal:

- "First search for $K^+ \to \pi^+ \nu\bar{\nu}$ using the decay-in-flight technique", accepted for publication in *Physics Letters B PLB-D-18-01825R1.*

The NA62 collaboration usually requires more than one independent analysis for a publication. The author of this thesis is one of the two main authors and one of the two main persons responsible for the analysis work of the above publication. He has carried out the analysis independently of the other main analysis. Both analyses obtained the exact same result. The work has been carried out by the author within the NA62 collaboration, which is an international collaboration of more than 350 scientists and engineers from 31 institutes in 15 countries. This implies the usage of common software used to analyse the data from the NA62 experiment. Both the collection of the data and the development of the common software used to analyse them result from the effort of many current and former collaboration members. The author presented the results for the first time to a public audience at the *Moriond EW 2018* conference in La Thuile, Italy. A more technical and detailed description of the analysis procedure is available internally to the NA62 collaboration.

Abstract

The decay $K^+ \to \pi^+ \nu\overline{\nu}$ with a very precisely predicted branching ratio of 8.4×10^{-10} is one of the best candidates to reveal indirect effects of new physics at the highest mass scales. The NA62 experiment at CERN SPS is designed to measure the branching ratio of the $K^+ \to \pi^+ \nu\overline{\nu}$ decay with a decay-in-flight technique, novel for this channel. The search for the $K^+ \to \pi^+ \nu\overline{\nu}$ decay is presented in this thesis, based on a sample of about 10^{11} K^+ decays collected in 2016 by the NA62 experiment. The Single Event Sensitivity is found to be 3×10^{-10} corresponding to about 0.26 $K^+ \to \pi^+ \nu\overline{\nu}$ and 0.15 background events expected. The analysis has revealed one candidate event compatible with the expectations. Interpreting the candidate as background leads to a 95% CL upper limit of 1.4×10^{-9} on the $K^+ \to \pi^+ \nu\overline{\nu}$ branching ratio. Prospects for future developments are also reviewed.

Zusammenfassung

Der Zerfall $K^+ \to \pi^+ \nu\overline{\nu}$ mit einem sehr genau vorhergesagten Verzweigungsverhältnis von 8.4×10^{-10} ist einer der besten Kandidaten, um indirekte Effekte neuer Physik auf höchsten Massenskalen zu finden. Das NA62-Experiment am CERN SPS wurde entwickelt, um das Verzweigungsverhältnis des $K^+ \to \pi^+ \nu\overline{\nu}$-Zerfalls mit einer für diesen Kanal neuartigen *Decay-in-flight*-Technik zu messen. Die Suche nach dem $K^+ \to \pi^+ \nu\overline{\nu}$-Zerfall wird in dieser Arbeit mit einem Datensatz von etwa 10^{11} K^+-Zerfällen im Jahr 2016 mit dem NA62-Experiment aufgezeichnet wurden, durchgeführt. Die Single-Event-Sensitivität ist 3×10^{-10} und entspricht etwa 0.26 $K^+ \to \pi^+ \nu\overline{\nu}$- und 0.15 Hintergrundereignissen. Die Analyse findet einen Kandidaten und ist mit dem Erwartungen vereinbar. Wenn man den gefundenen Kandidaten als Untergrund interpretiert, führt dies zu einer Obergrenze vom 1.4×10^{-9} bei 95% CL auf das $K^+ \to \pi^+ \nu\overline{\nu}$-Verzweigungsverhältnis. Aussichten für zukünftige Entwicklungen werden ebenfalls dargestellt.

Contents

1 Introduction

Kaons have played a key role in the understanding of particle physics, from their discovery[1] in 1947 until today, when rare kaon decays are still providing valuable insights about low-energy physics. Particularly interesting are the decays $K^+ \to \pi^+ \nu\overline{\nu}$ and $K_L^0 \to \pi^0 \nu\overline{\nu}$, often referred to as the golden modes of flavour physics, because they are theoretically clean and allow for very precise theoretical predictions. Due to quadratic GIM suppression (Section 1.2) the branching ratio for both modes is of order 10^{-11}. If significant deviations with respect to the Standard Model are present in any of the branching ratios this will be a clear sign of New Physics.

The KOTO experiment using beam from the J-PARC accelerator complex in Japan aims to measure the neutral mode, while the NA62 experiment located in the North Area of the CERN accelerator complex in Switzerland uses a decay-in-flight technique to measure the charged mode with 10% precision. The two measurements, when available, will provide important constraints on the flavour dynamics of new physics.

This work describes the first measurement of the branching ratio of the $K^+ \to \pi^+ \nu\overline{\nu}$ decay with the data collected in 2016 by the NA62 experiment at CERN. In the following chapter the necessary theoretical tools needed to understand the $K^+ \to \pi^+ \nu\overline{\nu}$ process are discussed.

1.1 Electroweak interactions

The Standard Model (SM) of particle physics proposed by Glashow[2], Weinberg[3] and Salam[4] describes the interactions between three generations of quarks and leptons. The model is based on the gauge group $SU(3)_C \otimes SU(2)_L \otimes U(1)_Y$ spontaneously broken down to $SU(3)_C \otimes U(1)_Q$ by the Higgs mechanism[5,6]. Here Y and Q denote the weak hypercharge and the electric charge generators. $SU(3)_C$ is the group of the strong interactions mediated by eight massless gluons and described by quantum chromodynamics (QCD). The electroweak interaction, represented by the $SU(2)_L \otimes U(1)_Y$ group, is mediated by the $W^{\pm}$, Z^0, γ. It is useful to recall some properties of the electroweak interactions that can be found in any standard particle physics book[7,8].

The left-handed quarks and leptons are arranged in three generations of $SU(2)_L$ doublets

$$\begin{pmatrix} u \\ d' \end{pmatrix}_L \qquad \begin{pmatrix} c \\ s' \end{pmatrix}_L \qquad \begin{pmatrix} t \\ b' \end{pmatrix}_L \tag{1.1}$$

$$\begin{pmatrix} \nu_e \\ e \end{pmatrix}_L \qquad \begin{pmatrix} \nu_\mu \\ \mu \end{pmatrix}_L \qquad \begin{pmatrix} \nu_\tau \\ \tau \end{pmatrix}_L \tag{1.2}$$

with the corresponding right-handed fields transforming as singlets under $SU(2)_L$ transformations. The primes are discussed in Section 1.2.

The electroweak interactions are mediated by the massive gauge bosons $W^\pm$ and Z^0 and the photon γ. These interactions can be summarized by the Lagrangian

$$\mathcal{L}_{\text{int}} = \mathcal{L}_{\text{CC}} + \mathcal{L}_{\text{NC}}, \tag{1.3}$$

where

$$\mathcal{L}_{\text{CC}} = \frac{g_2}{2\sqrt{2}} \left(J^+_\mu W^{+\mu} + J^-_\mu W^{-\mu} \right) \tag{1.4}$$

describes the charged current interactions and

$$\mathcal{L}_{\text{NC}} = e J^{\text{em}}_\mu A^\mu + \frac{g_2}{2\cos\Theta_W} J^0_\mu Z^\mu \tag{1.5}$$

the neutral current interactions. Here e is the QED coupling constant, g_2 is the $SU(2)_L$ coupling constant and Θ_W is the Weinberg angle. The currents are given as

$$J^+_\mu = (\bar{u}d')_{V-A} + (\bar{c}s')_{V-A} + (\bar{t}b')_{V-A} + (\bar{\nu_e}e')_{V-A} + (\bar{\nu_\mu}\mu')_{V-A} + (\bar{\nu_\tau}\tau')_{V-A}, \tag{1.6}$$

$$J^{\text{em}}_\mu = \sum_f Q_f \bar{f} \gamma_\mu f, \tag{1.7}$$

$$J^0_\mu = \sum_f \bar{f}\gamma_\mu (T^f_3 - 2Q_f \sin\Theta_W{}^2 - T^f_3 \gamma_5) f, \tag{1.8}$$

where Q_f and T^f_3 denote the electromagnetic charge and the third component of the weak isospin of the left-handed fermions f. The $V-A$ subscript stands for the $\gamma^\mu(1-\gamma_5)$ structure of the weak interaction. The relevant electroweak charges Q and Y and the third component of the weak isospin T_3 for the quarks and leptons in the SM are collected in Table 1.1.

The charged current processes mediated by the $W^\pm$ bosons are flavour violating with the strength of the violation given by the weak coupling constant g_2, which at low energies is effectively related to the Fermi constant by

$$\frac{G_F}{\sqrt{2}} = \frac{g_2^2}{8M_W^2}. \tag{1.9}$$

	ν_L^e	e_L^-	e_R^-	u_L	d_L	u_R	d_R
Q	0	-1	-1	2/3	-1/3	2/3	-1/3
T_3	1/2	-1/2	0	1/2	-1/2	0	0
Y	-1	-1	-2	1/3	1/3	4/3	-2/3

Table 1.1: *Electroweak charges QY and the third component of the weak isospin T_3 for the quarks and leptons in the Standard Model.*

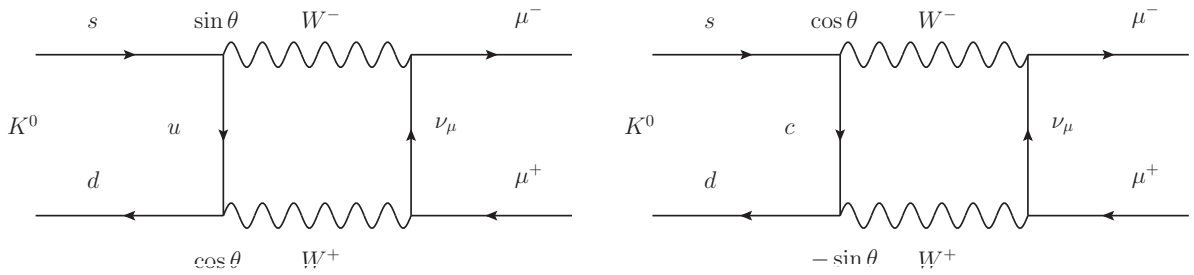

Figure 1.1: *Two contributions to the $K_L \to \mu^+\mu^-$ process: u-quark (left) and c-quark (right).*

The neutral currents mediated by the photon γ and the Z^0 are flavour conserving.

1.2 Quark mixing

In the early 1960s Cabibbo realized that the weak eigenstates of the known quarks with charge $-1/3$ are not the mass eigenstates d and s, but a linear combination rotated by an angle θ

$$d' = d\cos\theta + s\sin\theta. \tag{1.10}$$

This idea was later extended by Glashow, Iliopoulos and Maiani (GIM)[10] by introducing a (2×2) matrix V' and adding a new up-type quark from symmetry considerations. The modified charged current Lagrangian for two generations of quarks then takes the form

$$\mathcal{L}_{\text{int}} = (\bar{u},\, \bar{c})\gamma^\mu W_\mu^\pm \,(1+\gamma_5)\, V' \begin{pmatrix} d \\ s \end{pmatrix} \tag{1.11}$$

The mechanism was necessary to explain the anomalously low $K_L \to \mu^+\mu^-$ branching ratio of about $7 \cdot 10^{-9}$ [(11)] observed at that time. Adding the newly proposed c-quark gives two Feynman diagrams contributing to the decay rate (Figure 1.1). Both diagrams are proportional to $\cos\theta\sin\theta$, but have opposite signs and cancel. However, the cancellation is not perfect due to the mass difference between the u and the c quarks and the residual amplitude is different from 0, but still heavily suppressed.

The mixing matrix was then extended to a (3×3) unitary matrix by Kobayashi and Maskawa[12]

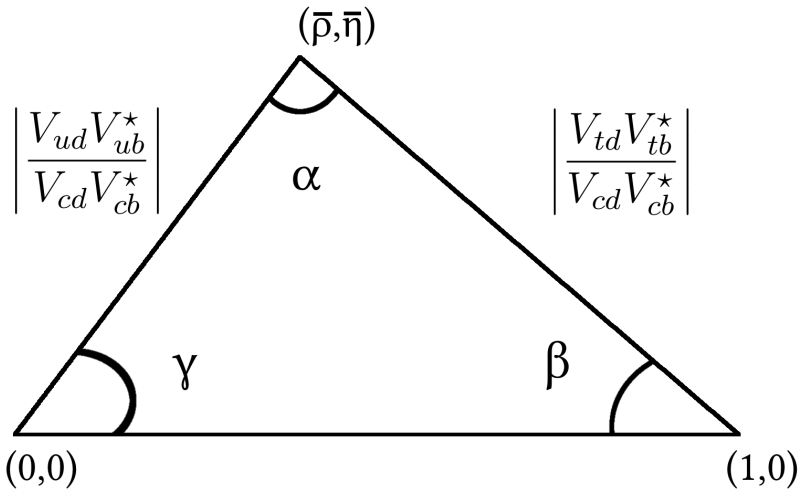

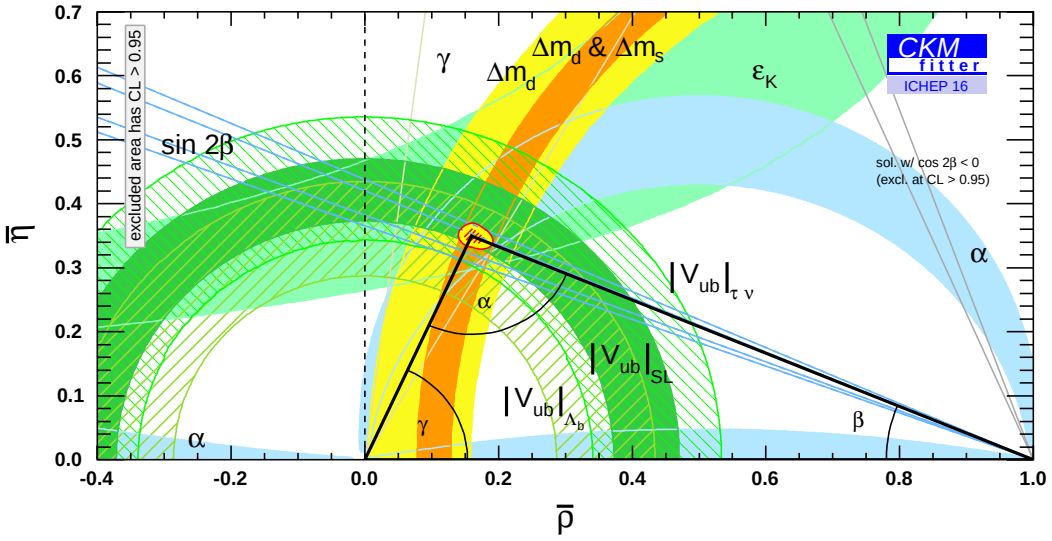

Figure 1.2: *Top: Sketch of the unitarity triangle constructed from* (1.14)*. Bottom: Constraints in the* $(\bar{\rho}, \bar{\eta})$ *plane taken from the CKM fitter collaboration*[9]*.*

to include a third generation of quarks, namely the top (t) and the bottom (b),

$$V_{\mathrm{CKM}} = \begin{pmatrix} V_{ud} & V_{cd} & V_{td} \\ V_{us} & V_{cs} & V_{ts} \\ V_{ub} & V_{cb} & V_{tb} \end{pmatrix} . \tag{1.12}$$

It can be parametrized by 3 real parameters and one complex phase. It is known experimentally that the CKM elements exhibit a hierarchical pattern with the diagonal elements being close to unity, the elements $|V_{us}|$ and $|V_{cd}|$ being of order 0.2, $|V_{cb}|$ and $|V_{ts}|$ of order $4 \cdot 10^{-2}$ and $|V_{ub}|$ and $|V_{td}|$ of order $5 \cdot 10^{-3}$. In the Wolfenstein parametrization[13] each parameter is expanded as a power series in the small parameter $\lambda = |V_{us}|$ reflecting the hierarchy of the CKM elements

$$V_{\mathrm{CKM}} = \begin{pmatrix} 1 - \lambda^2/2 & \lambda & A\lambda^3 (\rho - i\eta) \\ -\lambda & 1 - \lambda^2/2 & A\lambda^2 \\ A\lambda^3 (1 - \rho - i\eta) & -A\lambda^2 & 1 \end{pmatrix} + \mathcal{O}(\lambda^4). \tag{1.13}$$

Here λ, A, ρ are the real parameters and η the complex phase responsible for CP violation in the SM. The unitarity of the CKM matrix ($V_{\mathrm{CKM}} V_{\mathrm{CKM}}^{\dagger} = V_{\mathrm{CKM}}^{\dagger} V_{\mathrm{CKM}} = 1$) imposes 9 conditions on the elements $\sum_j V_{ij} V_{jk}^{\star} = \delta_{ik}$. The six vanishing combinations can be represented as triangles in the complex plane, of which those obtained from multiplying two neighbouring rows or columns are nearly degenerate. The unitarity relation

$$V_{ud} V_{ub}^{\star} + V_{cd} V_{cb}^{\star} + V_{td} V_{tb}^{\star} = 0. \tag{1.14}$$

is particularly interesting, because all sides of the corresponding complex triangle are of $\mathcal{O}(\lambda^3)$ and is commonly referred to as "the" unitarity triangle (UT) after rescaling by a factor $1/\left(V_{cd} V_{cb}^{\star}\right)$ (Figure 1.2-top). The sides of the unitarity triangle are given by

$$\left| \frac{V_{ud} V_{ub}^{\star}}{V_{cd} V_{cb}^{\star}} \right| = \sqrt{\bar{\rho}^2 + \bar{\eta}^2} \quad \text{and} \quad \left| \frac{V_{td} V_{tb}^{\star}}{V_{cd} V_{cb}^{\star}} \right| = \sqrt{(1 - \bar{\rho})^2 + \bar{\eta}^2}. \tag{1.15}$$

Here the parameters $\bar{\rho} = \rho(1 - \lambda^2/2)$ and $\bar{\eta} = \eta(1 - \lambda^2/2)$ are the coordinates in the complex plane of the apex of the triangle with the other two being (0,0) and (1,0). The experimental status of the UT is shown in Figure 1.2-bottom.

An important goal of flavour physics is to overconstrain the CKM elements, by measuring each element using different techniques. This provides a robust validation of the flavour sector of the SM, because sources of new physics can modify the flavour structure of the SM and induce deviations from the CKM mixing matrix. The most recent reviews of the present status of the CKM matrix can be found in[11,14].

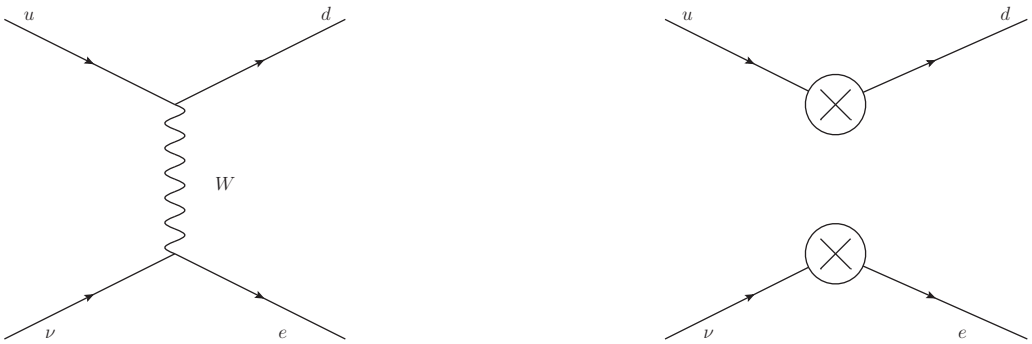

Figure 1.3: *β-decay at quark level in the full (left) and effective (right) theory.*

1.3 Weak interactions at low energies

Weak decays of hadrons are mediated through the weak interaction of their quark constituents. The strong interactions of quarks, binding them into hadrons, are characterized by a typical hadronic energy scale of the order of 1 GeV. At the kaon mass scale, the heavy W boson mediating the weak interaction can be therefore integrated out and the interaction of the quarks can be described using an effective low energy theory. The effective hamiltonian of this theory can be written as[15]

$$\mathcal{H}_{eff} = \frac{G_F}{\sqrt{2}} \sum_i V^i_{\mathrm{CKM}} C_i(\mu) Q_i(\mu), \tag{1.16}$$

where G_F is the Fermi constant extracted from muon decay; $Q_i(\mu)$ are the local four-fermion operators at the scale μ governing the decay in question; $C_i(\mu)$ are the Wilson coefficients[16,17], functions of the heavy masses (M_Z, M_W, m_t, m_b, and $m_c > \mu$), which together with the CKM factors V^i_{CKM} describe the strength with which a given operator enters the hamiltonian.

As an example one can consider the effective hamiltonian of the β-decay (Figure 1.3)

$$\mathcal{H}_{eff} = \frac{G_F}{\sqrt{2}} V_{ud} \left[\bar{u}\gamma_\mu \left(1-\gamma_5\right) d\right] \left[\bar{e}\gamma^\mu \left(1-\gamma_5\right) \nu_e\right]. \tag{1.17}$$

In this case the Wilson coefficient is equal to unity and the local operator is a product between two $V-A$ currents (the two objects in the square brackets). The effective Hamiltonian in (1.17) represents the Fermi theory for β-decays[18,19]. The expression (1.16) can be regarded as a generalization of the Fermi Theory to include all known quarks and leptons as well as their strong and electroweak interactions in the Standard Model.

While the Feynman diagrams with full W, Z and top-quark propagators represent the picture at very short distance scales $\mathcal{O}(M_W, M_Z, m_t)$, the true picture of a decaying hadron with masses $\mathcal{O}(m_b, m_c, m_K)$ is more properly described by effective point-like vertices represented by the local operators Q_i. The Wilson coefficients C_i can then be regarded as coupling constants associated to these effective vertices. The series in (1.16) is known under the name of operator product expansion (OPE)[16,17]. In the general case the structure of the local operators is much more complicated than that of the β-decay, owing to the interplay between electroweak and strong interactions. The operators can be classified according to their Dirac structure, color structure

and the type of quarks and leptons participating for a given decay.

The coefficients $C_i(\mu)$ summarize the physics contributions from scales higher than μ, which due to the asymptotic freedom of QCD can be calculated in a regime where μ is much larger than the hadron physics scale ($\mathcal{O}(1\text{ GeV})$) and the interaction is perturbative. In that regime C_i include contributions from the top-quark and the W- and Z-bosons, as well as from other heavy particles in extensions of the SM. At higher orders in the electroweak coupling contributions from the neutral Higgs boson are also possible. Consequently $C_i(\mu)$ depend on m_t and of the masses of possible new particles predicted by physics models beyond the Standard Model (BSM).

The value of the scale parameter μ can be chosen arbitrarily. Usually the contributions to the decay amplitude for a given process is separated into short-distance part at scales much larger than μ and a long-distance part at scales lower than μ. The typical choice for μ is the mass of the decaying hadron. For kaon decays, however, the choice $\mu = \mathcal{O}(m_K)$ is not appropriate, because the QCD is not perturbative in that regime and $\mu = \mathcal{O}(1 - 2\text{ GeV})$ is used instead. To match the physics scale of the weak process ($\mathcal{O}(M_W)$) with 5 active quarks flavours (the top-quark is too heavy) to the low energy ($\mathcal{O}(\mu)$) where only the u, d and s quarks are active one must run the strong coupling α_s down to the scale μ using renormalization group methods[20,21,22,23,24].

One can construct the decay amplitude for a given process using the effective Hamiltonian H_{eff}. Let's take as an example the transition of a K meson ($M = K$) to a final state $F = \pi\nu\overline{\nu}$. This decay is described by the local operator

$$Q(\mu) = [\bar{s}\gamma^{\mu}(1-\gamma_5)\,d]\,[\bar{\nu}\gamma(1-\gamma_5)\nu] \tag{1.18}$$

and the decay amplitude can be written as

$$A(M \to F) = \langle F\,|H_{eff}|\,M\rangle = \frac{G_F}{\sqrt{2}} V_{\mathrm{CKM}} C(\mu) \langle F\,|Q(\mu)|\,M\rangle, \tag{1.19}$$

where $\langle F\,|Q(\mu)|\,M\rangle$ is the hadronic matrix elements of $Q(\mu)$ between the initial and the final state. The matrix element similarly to $C(\mu)$ depends on the scale μ and summarizes the physics contribution to the amplitude $A(M \to F)$ at scales lower than μ.

A very important feature of (1.19) is that the calculation of the decay amplitude $A(M \to F)$ is divided into two parts: the short-distance (perturbative) part of the coupling $C(\mu)$ and the long-distance (non-perturbative) part of the matrix element $\langle Q(\mu)\rangle$. The physics scale μ separates the two contributions. By evolving the scale from $\mu = \mathcal{O}(M_W)$ down to lower values one simply transforms the physics contributions at scales higher than μ from the hadronic matrix element to $C(\mu)$. Since no information is lost in this process the amplitude can not depend on the arbitrary parameter μ, so the μ dependence of $C(\mu)$ cancels the one of $\langle Q(\mu)\rangle$.

The computation of the matrix element $\langle Q(\mu)\rangle$ involves long-distance effects, therefore non-perturbative approaches like lattice QCD[25] and chiral perturbation theory (CHPT)[26,27] are needed. Those approaches work particularly well in semi-leptonic decays, where the final state consists of only one hadron and chiral perturbation theory gives good predictions.

A comprehensive review on the theoretical treatment of weak hadron decays can be found in[15]. Recent reviews on kaon decays in the SM can be found in[28,29].

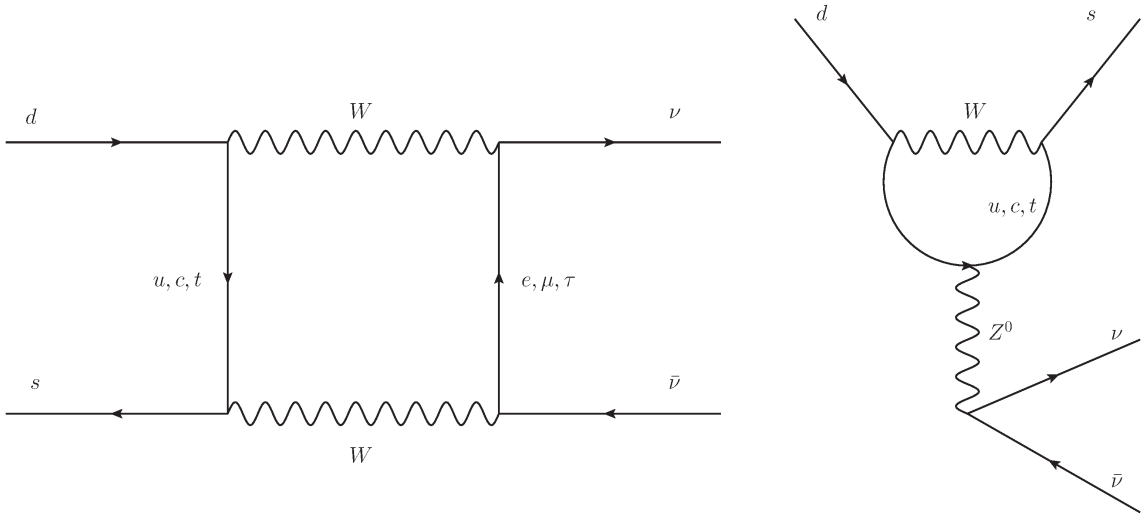

Figure 1.4: *Box (left) and Z-Penguin (right) diagrams for the $K^+ \to \pi^+ \nu\bar{\nu}$ decay.*

1.4 The $K^+ \to \pi^+ \nu\bar{\nu}$ decay

The $K^+ \to \pi^+ \nu\bar{\nu}$ decay is a FCNC transition transforming an s-quark to a d-quark and a neutrino-antineutrino pair. In the SM it is dominated by Z^0 penguin and box diagrams shown in Figure 1.4. The history of the theoretical and experimental efforts towards this decay is rich and dates back to the late 60s (Figure 1.5). The theoretical progress was heavily influenced by the improvements of our knowledge of the SM parameters and the improvement of the experimental results.

The first SM computation of the $K^+ \to \pi^+ \nu\bar{\nu}$ decay was made in 1969 when the quark sector of the SM consisted of only u, d and s quarks and yielded an upper limit of 5×10^{-5} on the branching ratio. The FCNC suppression via the GIM mechanism[10] and the discovery of the c-quark[46,47] in the mid 70s had a major impact on the prediction, bringing it down to the $10^{-9} - 10^{-10}$ level. No further progress was made until the late 80s when the $B^0 - \overline{B^0}$ mixing was discovered[48,49], which hinted that the top-quark mass is in the $50 - 100$ GeV range and allowed the possibility to compute the relevant contribution to the amplitude. However, the uncertainties were still large and sizable improvements came only after the discovery of the top-quark[50] at Fermilab in 1995, establishing the rate to be of order 10^{-10}. The last major step in reducing the uncertainty was the extraction of the decay matrix element from $K^+ \to l^+ \pi^0 \nu_e$ decays and relating it to the $K^+ \to \pi^+ \nu\bar{\nu}$ decay using the isospin symmetry between the π^0 and π^+. In the following decade the precision increased when higher order QCD and electroweak correction became available, making the $K^+ \to \pi^+ \nu\bar{\nu}$ decay one the most precisely computed FCNC processes involving quarks. The results of the most recent theoretical computations on the $K^+ \to \pi^+ \nu\bar{\nu}$ decay[36] are discussed in the following.

The master formula for the branching ratio can be written summing over the three neutrino

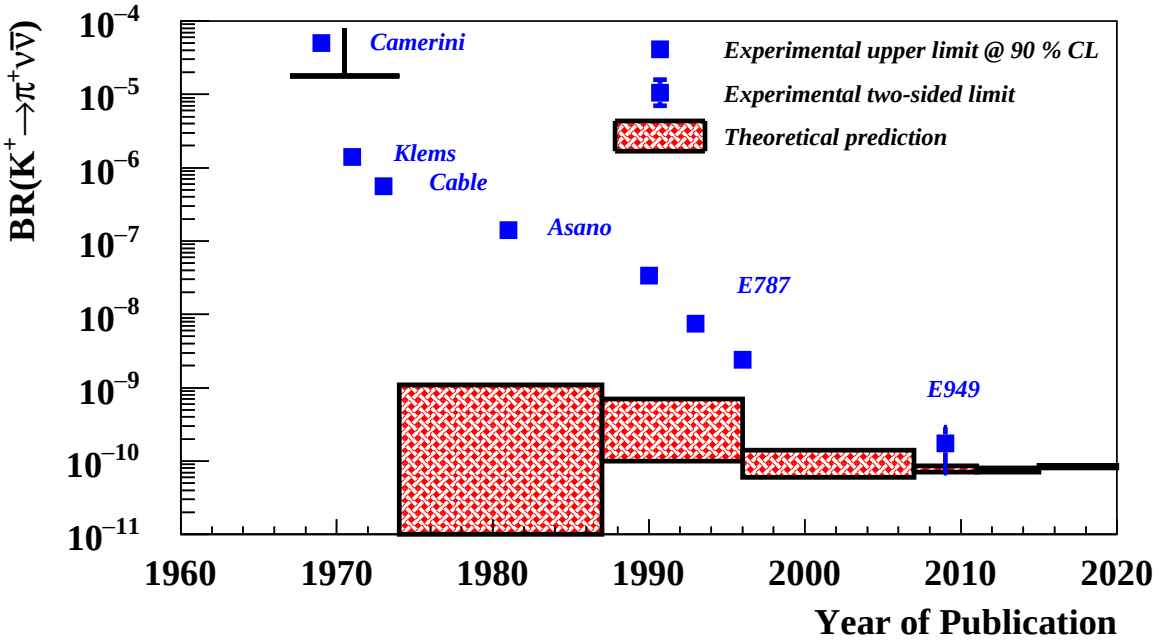

Figure 1.5: *History of the theoretical and experimental efforts directed towards the* $K^+ \to \pi^+ \nu\overline{\nu}$ *decay. The red hatched rectangles depict the theoretical results and uncertainties during the last 50 years. The major theoretical improvements are quoted, from left to right,* [30,31,32,33,34,35,36]*. The experimental limits are shown with blue squares and are quoted, from left to right,* [37,38,39,40,41,42,43(44,45)]*. All experimental results are produced using a stopped kaon technique.*

flavors as

$$\mathcal{B}\left(K^+ \to \pi^+ \nu\overline{\nu}\right) = k_+(1+\Delta_{EM}) \cdot \left[\left(\frac{Im\ \lambda_t}{\lambda^5}\ X(x_t)\right)^2 + \left(\frac{Re\ \lambda_c}{\lambda}\ (P_c(X)+\delta P_{c,u}) + \frac{Re\ \lambda_t}{\lambda^5}\ X(x_t)\right)^2\right]. \tag{1.20}$$

Here $k_+ = (5.173 \pm 0.025) \cdot 10^{-11} \left[\frac{\lambda}{0.225}\right]^8$ is the hadronic matrix element extracted from semi-leptonic $K^+ \to l^+ \pi^0 \nu_l$ ($l = \mu,\ e$) decays[34], corrected for isospin-breaking effects; $\Delta_{EM} = -0.003$ is the electromagnetic radiative correction to k_+; $x_t = m_t^2/M_W^2$; $\lambda_i = V_{is}^* V_{id}$ and $\lambda = |V_{us}|$ are factors involving the CKM matrix elements; $X(x_t)$ is the loop function representing the top-quark contribution; $P_c(X)$ and $\delta P_{c,u}$ summarize the charm- and u- quark contributions.

Due to the quadratic GIM mechanism the FCC contributions of an up-type quark running in the loops are suppressed by a factor $x_q = m_q^2/m_W^2$. The top-quark has the dominant contribution to the branching ratio due to its large mass $m_t \approx 173$ GeV/c^2 [(11)], while the charm- and up-quarks with masses 1.3 GeV/c^2 and 2.2 MeV/c^2 [(11)] are doubly suppressed.

The top-quark contribution is $X(x_t) = 1.48 \pm 0.01$ including two-loop electroweak corrections[35] and NLO QCD corrections[51]. The short distance charm-quark and long distance charm- and up-quark contributions are $P_c(X) = 0.365 \pm 0.012$ and $\delta P_{c,u} = 0.04 \pm 0.02$, respectively,

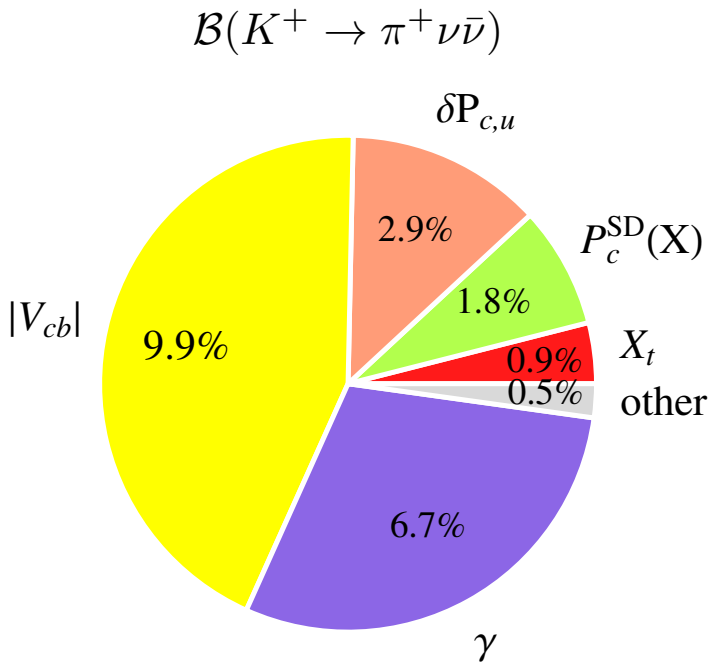

Figure 1.6: *Error budget of the $K^+ \to \pi^+ \nu\bar{\nu}$ branching ratio*[36].

based on the detailed analyses including electroweak corrections[52] and NNLO QCD corrections computed in the framework of chiral perturbation theory[53,54]. The apparent sensitivity of $\mathcal{B}(K^+ \to \pi^+ \nu\bar{\nu})$ to λ is spurious as both $P_c(X)$ and $\delta P_{c,u}$ terms are $\sim \lambda^{-4}$ so the λ dependence of k_+ is cancelled to a large extent.

Assuming that the SM is valid at tree-level[36] the CKM matrix can be determined using only the tree-level observables $|V_{ub}|$, $|V_{cb}|$, $|V_{us}|$ and the CKM angle γ. This assumption is on solid ground, because New Physics (NP) beyond the SM seems to be separated from the electroweak scale and the CKM matrix determination should not be polluted by NP contributions. The relevant quantities λ_t and λ_c involving CKM input can then be expressed using only tree-level measurements

$$Re\lambda_t = |V_{ub}||V_{cb}| \cos\gamma (1 - 2\lambda^2) + (|V_{ub}^2 - |V_{cb}|^2)\lambda \left(1 - \frac{\lambda^2}{2}\right); \tag{1.21}$$

$$Im\lambda_t = |V_{ub}||V_{cb}| \sin\gamma; \tag{1.22}$$

$$Re\lambda_c = -\lambda \left(1 - \frac{\lambda^2}{2}\right). \tag{1.23}$$

The CKM angle $\gamma = (73.2^{+6.3}_{-7.0})^\circ$ and the λ parameter $\lambda = |V_{us}| = 0.2252(9)$ are taken from the PDG[11]. A weighted average between the exclusive and inclusive determinations of $|V_{ub}|$ and $|V_{cb}|$ is computed in[36] to

$$|V_{ub}|_{\text{avg}} = (3.88 \pm 0.29) \times 10^{-3}, \quad |V_{cb}|_{\text{avg}} = (40.7 \pm 1.4) \times 10^{-3}. \tag{1.24}$$

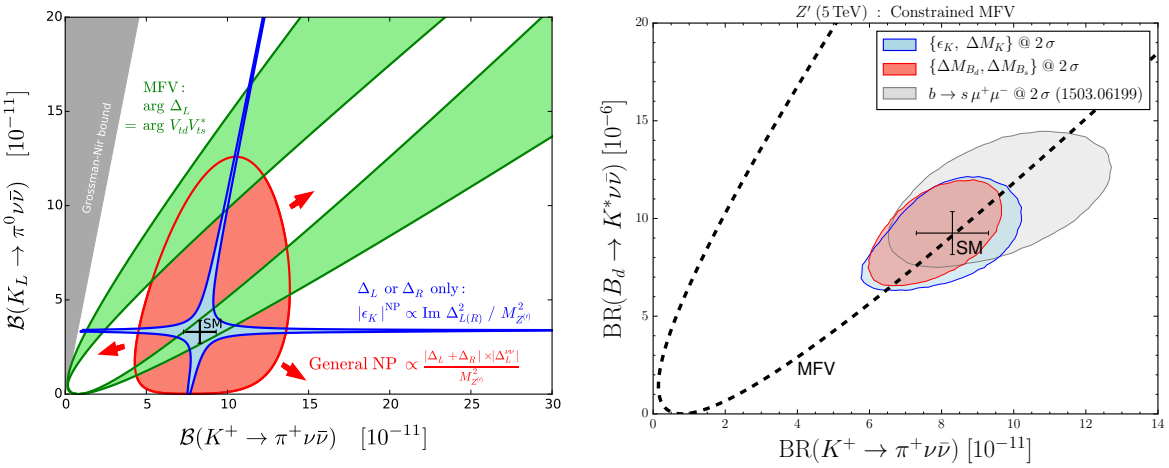

Figure 1.7: *Left: correlations between the $\mathcal{B}(K^+ \to \pi^+ \nu\overline{\nu})$ and $\mathcal{B}(K_L \to \pi^0 \nu\overline{\nu})$ decays. The expanding red region illustrates the lack of correlation for models with general LH and RH NP couplings. The green region shows the correlation present in models obeying constrained MFV. The blue region shows the correlation induced by the constraint from kaon mixing (ϵ_K) if only LH or RH couplings are present. Right: Allowed ranges for $K^+ \to \pi^+ \nu\overline{\nu}$ versus $B_d \to K^\star \nu\overline{\nu}$ for a 5 TeV Z' model with constrained MFV. Constraints from kaon mixing (blue), B mixing and $b \to s\mu\mu$ transition (grey) are shown at 2σ confidence level. Plots are taken from*[55].

The above expressions can be directly inserted in (1.20) to determine the branching ratio

$$\mathcal{B}(K^+ \to \pi^+ \nu\overline{\nu}) = (8.4 \pm 1.0) \times 10^{-11}. \tag{1.25}$$

The uncertainty is dominated by the uncertainties on the CKM parameters $|V_{cb}|$ and γ (Figure 1.6) and is dominated by the discrepancies between the exclusive and inclusive determination of $|V_{cb}|$ and the large errors on γ. The largest theoretical uncertainty is due to poor knowledge of the long-distance $\delta P_{c,u}$ contribution and amounts to about $\pm 3\%$.

It is convenient to parametrize the expression in (1.20) as

$$\mathcal{B}(K^+ \to \pi^+ \nu\overline{\nu}) = (8.4 \pm 0.3) \times 10^{-11} \cdot \left[\frac{|V_{cb}|}{40.7 \times 10^{-3}}\right]^{2.8} \left[\frac{\gamma}{73.2^\circ}\right]^{0.708}, \tag{1.26}$$

to separate the theoretical from the parametric uncertainty. Future improvements on the knowledge of $|V_{cb}|$ and γ will reduce the uncertainty on the branching ratio dramatically.

BSM scenarios

The $K^+ \to \pi^+ \nu\overline{\nu}$ process is among the most promising places to search for non-standard signals in flavour physics. The specific CKM suppression ($\sim |V_{us}|^5$) also allows tests of the flavour structure of the NP involved. Many BSM scenarios are possible including numerous new parameters. To compare branching ratio predictions one has to choose benchmark models with specific

constraints. Even in models with Minimal Flavour Violation (MFV), where the CKM matrix is the only source of quark mixing and CP violation, the $K^+ \to \pi^+ \nu\overline{\nu}$ decay still provides useful information, since the SM contribution can be predicted accurately.

Different correlations between SM observables are also possible, which can impose constraints on the allowed range of the branching ratio in simplified new physics models. As an example one can take a model reviewed in[55], with a new heavy gauge boson Z' generating tree-level FCNCs. In the most general case one can predict the correlations between the $K^+ \to \pi^+ \nu\overline{\nu}$ and $K_L \to \pi^0 \nu\overline{\nu}$ decays for different values of $M_{Z'}$ and the Z' couplings $\Delta_{L,R}$ (Figure 1.7-left). Further imposing the MFV hypothesis and constraints from $b \to s\mu^+\mu^-$ transitions, ΔM_{B_d}, $\Delta M_{B_s}, \Delta M_K$ and ϵ_K one can also correlate $K^+ \to \pi^+ \nu\overline{\nu}$ and $B_d \to K^\star \nu\overline{\nu}$ decays (Figure 1.7-right). A review of models involving heavy gauge bosons can be found in[56].

Other models have recently become available involving lepton flavour non-universality[57,58], which assume that the new physics can be coupled only to the third generation of quarks and leptons. Those models are motivated by the recently observed anomalies in the B sector[59,60], and can also explain why no significant excesses with respect to the SM have been observed in the kaon sector so far[61].

The $K^+ \to \pi^+ \nu\overline{\nu}$ decay is treated in many other BSM frameworks, among which the most notable involving extra dimensions[62], littlest Higgs[63], minimal supersymmetric models[64,65] and leptoquarks[66,67].

Nowadays rare decays are the key to understand new physics and to disentangle between different models through correlations between observables. A precise measurement of the $K^+ \to \pi^+ \nu\overline{\nu}$ branching ratio that will be provided by the NA62 experiment in the future, together with improved constraints from the $K_L \to \pi^0 \nu\overline{\nu}$ decay and the B sector is one of the most exciting tasks in flavour physics.

2

The NA62 experiment

The NA62 experiment is a fixed target experiment located in the CERN north area. The experiment uses a decay-in-flight technique to measure the decay $K^+ \to \pi^+ \nu\overline{\nu}$. With an integrated flux of $\mathcal{O}(10^{13})$ kaon decays and an acceptance of about 5% NA62 aims to collect about 20 signal events by the end of 2018, assuming the SM branching ratio. The description of the experimental setup is based on the NA62 detector paper[68], where the complete NA62 experimental setup and detector performances can be found. This thesis focuses on the analysis of the data collected in 2016.

2.1 Kaon beam line (K12)

The primary proton beam is extracted at 400 GeV/c from the CERN SPS accelerator and directed to a 400 mm long, 2 mm diameter beryllium target (T10), located in a tunnel connecting the SPS to the underground experimental hall. During a SPS spill of about 3 s effective duration a secondary beam is created from the interaction of the protons with the T10 target at 0 production angle. The particle rate in the NA62 positive secondary hadron beam (K12) is 750 MHz, of which about 6% is from K^+, leading to 5 MHz of K^+ decays in the 65 m long decay region.

The schematic layout of the K12 beam line is shown in Figure 2.1. The beam is focused using a triplet of quadrupole magnets (Q1, Q2, Q3), followed by a front-end achromat (A1) to select a beam of positively-charged particles with 75 GeV/c central momentum and a 1% rms momentum bite. Inside A1, the beam passes through a set of holes in two motorized and water-cooled beam-dump units, TAX1 and TAX2, to make the momentum selection while absorbing the remaining primary proton beam and unwanted secondary particles. The achromat is followed by a triplet of quadrupoles (Q4, Q5, Q6) used to refocus the beam in the vertical plane and to make it parallel with limited width in the horizontal plane. The drift-space between these quadrupoles is occupied by two collimators (C1, C2), which redefine the vertical and horizontal

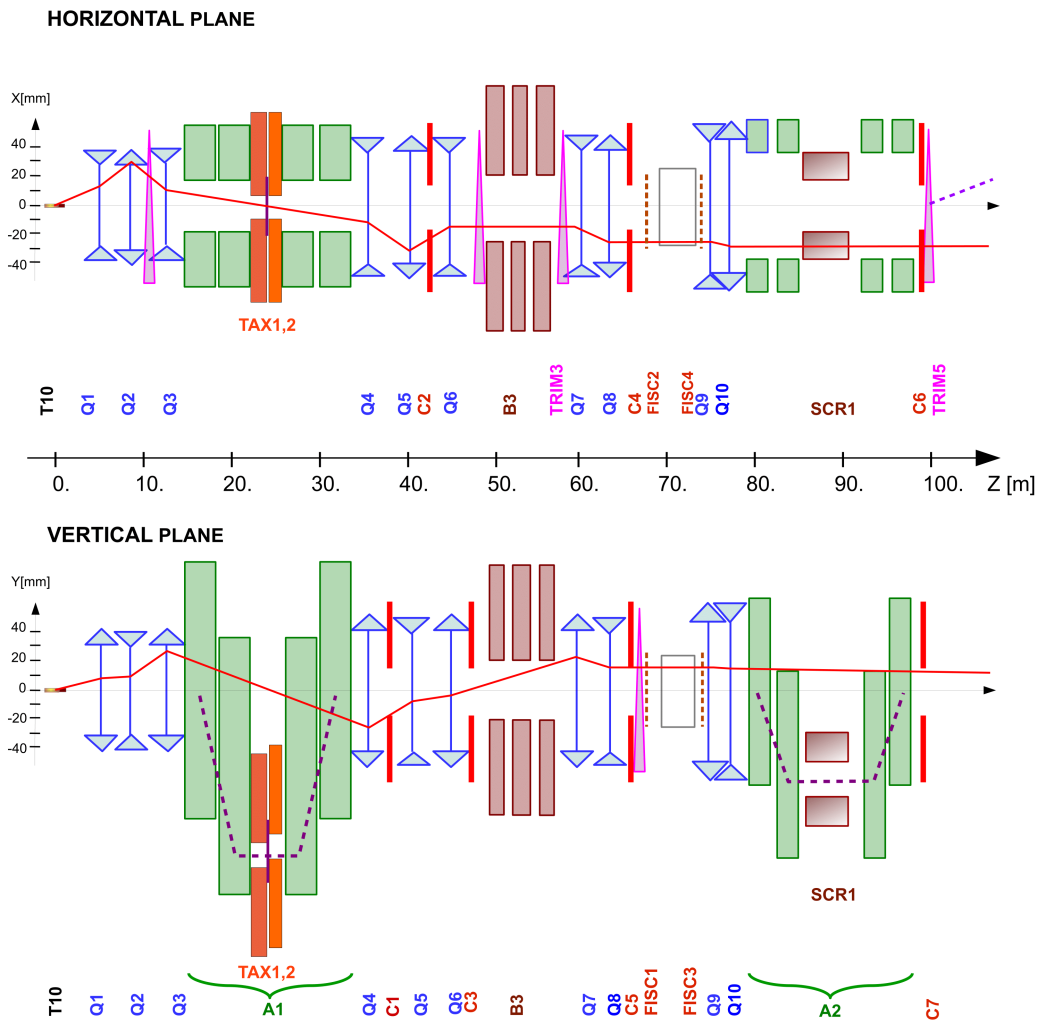

Figure 2.1: *Schematic layout and optics of the high-intensity positive hadron beam from the T10 target to the entrance of the decay region*[68]*. In each view, the solid line corresponds to the trajectory of a particle leaving the target from the centre at nominal momentum and at the angle indicated. The dashed line indicates the trajectory of an initially on-axis 75 GeV/c momentum particle.*

acceptance of the transmitted beam. A subsequent collimator (C3) redefines the beam at the second focus in the vertical plane.

After the initial focusing, the K12 beam is directed towards the NA62 detector. The scale and reference system for the experimental layout are displayed in Figure 2.2. The beam line defines the z axis with its origin at the kaon production target and beam particles travelling in the positive direction, the y axis points vertically up, and the x axis is horizontal and directed to form a right-handed coordinate system.

A differential Cherenkov counter[69] (KTAG) is used to identify the K^+ particles. The KTAG is preceded by two quadrupoles (Q7, Q8), as well as by horizontal and vertical cleaning collimators (C4, C5) to absorb particles in the tails of the beam.

Following the KTAG, a doublet of weakly-focusing quadrupoles (Q9, Q10) guides the beam through the tracking and momentum-measurement stage, shown schematically in Figure 2.3, and determine the beam divergence and size through the apertures of the downstream detectors.

The beam tracking system, GigaTracker (GTK), consists of three stations, each composed of silicon pixel detectors installed in the beam vacuum. The stations are arranged so that the space between GTK1 and GTK3 is occupied by a second achromat (A2), composed of four, vertically-deflecting, dipole magnets. The return yokes of the third and fourth magnets, as well as a toroidally-magnetized iron collimator SCR1, deflect muons which leave the beam in the momentum-dispersed section between the second and third magnet of the achromat. GTK2 is located in the same section, just after the magnetic collimator SCR1, where the 75 GeV/c beam has a parallel, downward displacement of $\Delta y = 60$ mm with respect to the beam axis and hence a dispersion of 0.6 mm per percent $\Delta p/p$. The GTK3 station, located at 102.4 m from the target, marks the entrance plane at the beginning of the decay region. The cleaning collimators (C6, C7) preceding GTK3 are intended to intercept background outside the beam acceptance.

In addition, a horizontal steering magnet (TRIM5) is used to deflect the beam towards positive x by an angle of $+1.2$ mrad. This angle is adjusted so that the subsequent -3.6 mrad deflection towards negative x, due to the downstream spectrometer magnet MNP33, directs the beam back through the central aperture of the LKr calorimeter.

The decay region is contained in the first 60 m of a large 117 m long tank, starting 102.4 m downstream of the target. The tank is evacuated to a residual pressure of $\sim 10^{-6}$ mbar. It hosts 11 LAV detectors and the four spectrometer STRAW chambers, and consists of 19 cylindrical sections made of steel or stainless steel. The vacuum tank is closed off at its downstream end by a thin aluminium window (2 mm thickness), separating the tank from the neon gas of the 17 m long RICH counter.

The RICH detector is followed by a system of charged hodoscope counters constructed from scintillator strips and tiles. The counters provide a time resolution of 150 ps, which is precise enough to define the reference trigger time for other detectors.

Two hadronic calorimeters (MUV1, MUV2) and, behind 80 cm of iron, a plane of scintillating tiles (MUV3) form the pion/muon identification system.

Additional counters (MUV0, HASC) installed at optimized locations provide hermetic coverage for charged particles produced in multi-track kaon decays.

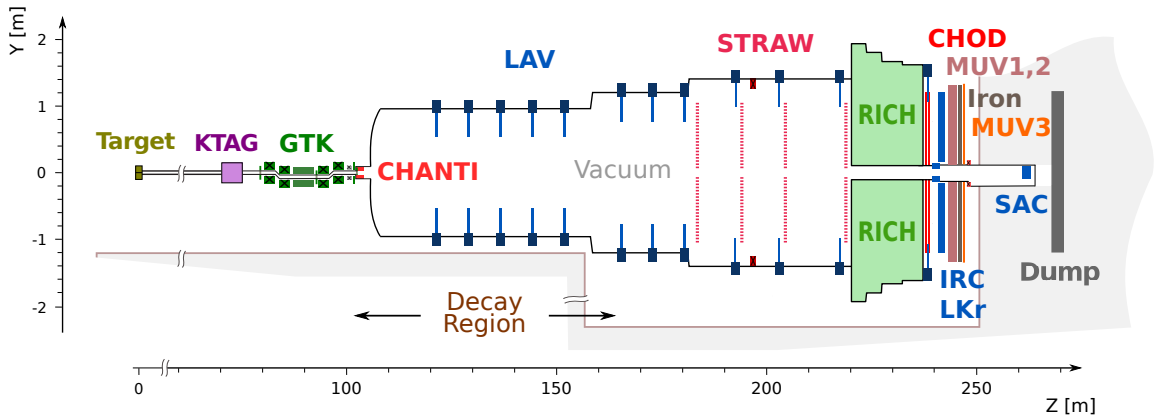

Figure 2.2: *Schematic vertical section through the NA62 experimental setup*[68]*. The main elements for the detection of the K^+ decay products are located along a 150 m long region starting 121 m downstream of the kaon production target. Useful K^+ decays are detected in a 65 m long decay region. Most detectors have an approximately cylindrical shape around the beam axis. An evacuated passage surrounding the beam trajectory allows the intense (750 MHz) flux of un-decayed beam particles to pass through without interacting with detector material before reaching the dump.*

2.2 Kaon Tagger (KTAG)

The K^+ mesons, constituting 6% of the beam are identified using the Kaon Tagger (KTAG). Through-going particles produce Cherenkov light in the gaseous radiator volume of the detector allowing to discriminate kaons, pions and protons in unseparated charged-particle beams. This requires the beam to be parallel to the z axis with an angular beam divergence below 100 μrad in each plane, and the angular alignment of the detector and beam axis to be of a similar accuracy.

In the NA62 configuration of 2016, the KTAG with its gas volume of 0.94 m^3 is filled with nitrogen gas (N_2) at 1.75 bar at room temperature. This represents, with the KTAG windows, a total of 3.5×10^{-2} X_0 of material in the path of the beam. The radiator gas is kept at room temperature. The pressure in the KTAG is chosen so that only light from the desired particle type, K^+, passes through an annular diaphragm of fixed central radius and varying radial aperture. The light is focused to exit the vessel through eight quartz windows and then focused onto eight spherical mirrors. The mirrors reflect the light radially outwards into eight light boxes (referred to as sectors), where light guides transport the light to photomultipliers. The typical time resolution achieved by the KTAG detector is 70 ps.

2.3 Beam spectrometer (GTK)

The GTK has been designed to measure the momentum of the 75 GeV/c beam particles to 0.2% precision and their direction, dx/dz and dy/dz, at the exit of the achromat to 16 μrad precision. The high beam rate (750 MHz and up to 1.5 MHz/mm^2 around the detector centre) requires a hit time resolution better than 200 ps[70].

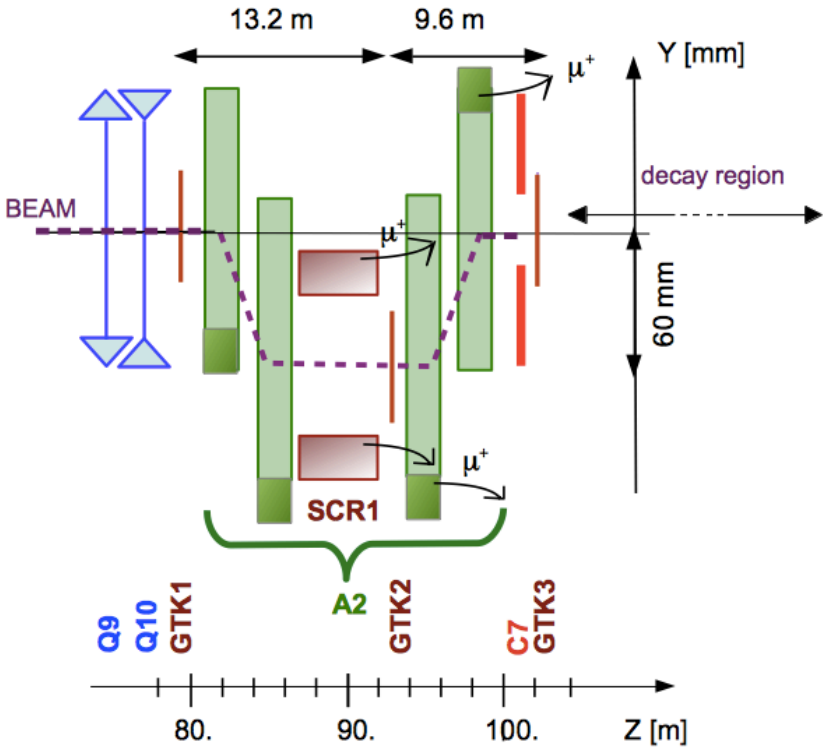

Figure 2.3: *Schematic layout of the beam tracking and momentum measurement in the second achromat (A2)*[68]*. The beam is deflected vertically by 60 mm and returned to its nominal direction after the momentum measurement. Muons are swept away by the magnetized scraping collimator SCR1 and the return yokes of the last two magnets of the achromat (dark shaded areas).*

Each station is a hybrid silicon detector consisting of 18 000 pixels of 300 × 300 μm^2 area each, arranged in a matrix of 200 × 90 elements corresponding to a total area of 62.8 × 27 mm^2. The material budget for each of the three stations is chosen to be less than 0.5% X_0, corresponding to a silicon thickness of about 500 μm.

The detector size and composition is optimized to obtain the desired momentum resolution of 0.2% and to suppress multiple Coulomb scattering. Reducing the multiple scattering has two main advantages: it improves the angular resolution and reduces the background produced by interactions in the last GTK station, where the products are not swept away by a magnetic field.

2.4 Charged anti-counter (CHANTI)

The CHANTI is composed of six consecutive square hodoscope stations 300 × 300 mm^2 in cross section with a 95 × 65 mm^2 hole in the centre to leave room for the beam. The first station is placed 28 mm downstream of GTK3, and the distance between each station and the next one approximately doubles for successive stations, so that the angular region between 49 mrad and 1.34 rad is covered hermetically for particles generated on GTK3. GTK3 and all CHANTI stations are located inside the same vacuum vessel.

The stations are made of scintillator bars of triangular cross section read out with fast wavelength-shifting (WLS) fibres coupled to silicon photomultipliers (SiPMs). Each station has two planes, with the bars oriented vertically and horizontally to form X and Y views. Particles incident from the front of the detector generally traverse two bars. Each of the six stations consists of 48 bars, adding to a total of 288 bars. A more detailed description of the CHANTI detector can be found in the CHANTI detector paper[71].

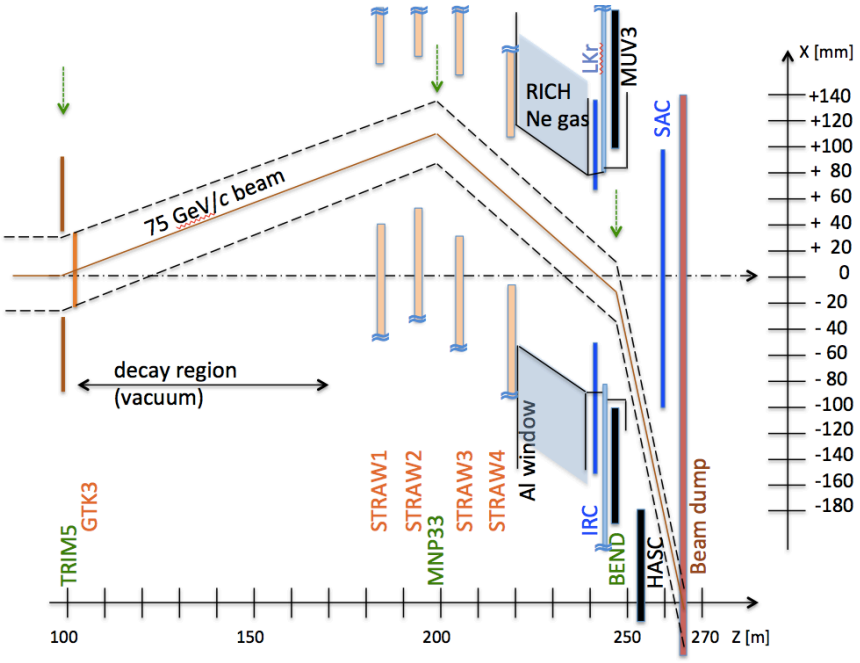

Figure 2.4: *Close view of the beam line layout through the decay region and the detectors in the (x, z) plane*[68]*. At the entrance of the decay region the beam has a horizontal angle of +1.2 mrad, the beam is then deflected in the spectrometer magnet MNP33 by −3.6 mrad to match the central aperture of the LKr calorimeter. After MUV3, the dipole magnet BEND deflects charged particles associated with the beam away from the SAC and sends them into the beam dump. The dashed lines correspond to the two sigma width of the beam profile. The vertical arrows indicate the bending centre of each magnet. Note the different scales of the two axes.*

2.5 Straw spectrometer (STRAW)

Downstream of the decay region, the STRAW tracker measures the trajectories and momenta of the charged products of K^+ decays. It extends over a length of 35 m along the beam line, starting $\sim$ 20 m after the decay region. The tracker includes two pairs of straw tracking chambers on either side of the large aperture dipole magnet (MNP33). The chambers cover the full acceptance outside a 118 mm diameter material-free passage around the beam path. The dipole magnet provides a horizontal momentum kick of 270 MeV/c, deflecting the 75 GeV/c beam by −3.6 mrad, so as to converge to, and then cross the undeviated axis at a point 2.8 m downstream of the centre of the LKr calorimeter.

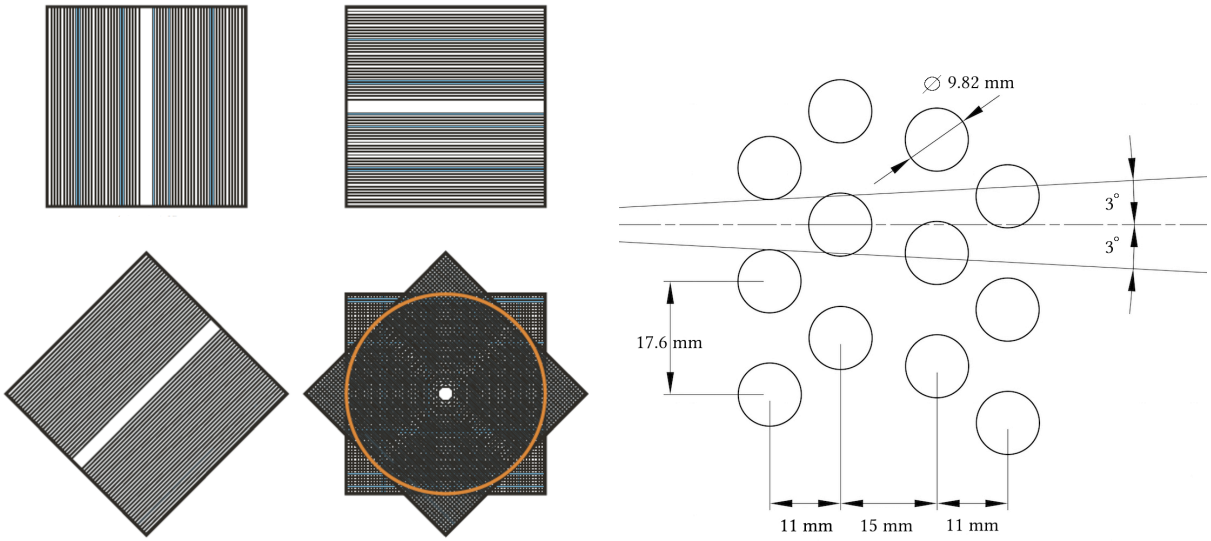

Figure 2.5: *Left: One straw chamber is composed of four views (X, Y, U, V) and each view measures one coordinate. Near the middle of each view a few straws are left out forming a free passage for the beam. Right: The straw geometry is based on two double layers per view with sufficient overlap to guarantee at least two straw crossings per view and per track, as needed to solve the left-right ambiguity. The ±3° angle corresponds to the angular range of tracks produced in kaon decays and detected within the geometrical acceptance of the spectrometer. Pictures taken from*[68]

The modules are designed to minimize multiple scattering and to give uniform space resolution over the full active area. The straw chambers are constructed of ultra-light material and are installed inside the vacuum tank. The total amount of material in the spectrometer corresponds to 1.8% X_0.

Each straw chamber contains 1792 straws of 9.82 mm diameter and 2160 mm length and is composed of two modules. One module contains two views measuring X (0°), Y (90°) and the other module contains the U (−45°) and V (+45°) views (Figure 2.5). The gas inside the straws is a mixture of 70% Ar and 30% CO_2 at atmospheric pressure. The straws are operated in the vacuum of the decay tank. The chamber active area is a circle of 2.1 m outer diameter centred on the longitudinal z axis.

Each view has a gap of about 12 cm without straws near the centre, such that, after overlaying the four views, an octagon shaped hole of 6 cm apothem is created for the beam passage. As the beam has an angle of +1.2 mrad and −3.6 mrad in the horizontal plane, upstream and downstream of the magnet, respectively (Figure 2.4), this hole is not centred on the z axis, but has offsets (along the x direction) for each chamber. High detection redundancy is provided through a straw arrangement with four layers per view, which guarantees at least two hits per view, i.e. $8 - 12$ hits per track per chamber (Figure 2.5). Due to the 12 cm gap without straws in each view, the number of hits per chamber is not evenly distributed over the detector surface.

The maximum drift time in the straws is approximately 140 ns and both leading and trailing edges of the signal are read out. The leading edge is used to measure the drift time which gives

Photon-veto detector	Angular coverage [mrad]	Design inefficiency
LAV	$8.5 - 50$	10^{-4} for $E_\gamma > 200$ MeV
LKr	$1 - 8.5$	10^{-3} for $E_\gamma > 1$ GeV 10^{-5} for $E_\gamma > 10$ GeV
IRC, SAC	$0 - 1$	10^{-4} for $E_\gamma > 5$ GeV

Table 2.1: *Characteristics of the NA62 photon-veto detectors.*

the lateral position of a track crossing a straw using the correlation between the radial distance (R) and the wire-drift time (R-t correlation). Because the maximum drift time in a cylindrical tube is the same for all tubes, the trailing edge gives a measurement of the absolute time of a hit and can be used to aggregate hits belonging to the same track.

Information from the trailing edge of the straw signal is used to calculate the time of the track. For tracks traversing all four chambers, the average number of straws per track is 27 and the track time resolution is found to be about 5 ns. The track momentum resolution of the straw spectrometer is

$$\frac{\sigma(P)}{P} = 0.30\% \oplus 0.005\% \cdot P, \tag{2.1}$$

where P is expressed in GeV/c. The track angular resolution decreases from 60 μrad at 10 GeV/c to 20 μrad at 50 GeV/c momentum.

2.6 Photon-veto system (PV)

A system of photon-veto detectors provides hermetic coverage for photons produced in the decay region and propagating at angles up to about 50 mrad with respect to the detector axis. Four different types of counters are used, listed below from larger to smaller angular coverage:

- a series of 12 annular Large-Angle photon Veto detectors (LAV);
- the Liquid Krypton electromagnetic calorimeter (LKr);
- the Intermediate-Ring (IRC) and Small-Angle (SAC) calorimeters.

The angular coverage of these detector systems and the photon detection efficiencies required for the $K^+ \to \pi^+\nu\overline{\nu}$ analysis are summarized in Table 2.1.

Large-angle veto system (LAV)

The ring-shaped large-angle photon vetoes are placed at 11 positions along the vacuum volume (Figure 2.2) while the 12th station is located about 3 m upstream of the LKr calorimeter and is operated in air. The LAV detectors provide full geometric coverage for photons from decays within the decay volume emitted at angles from 8.5 to 50 mrad with respect to the NA62 z axis.

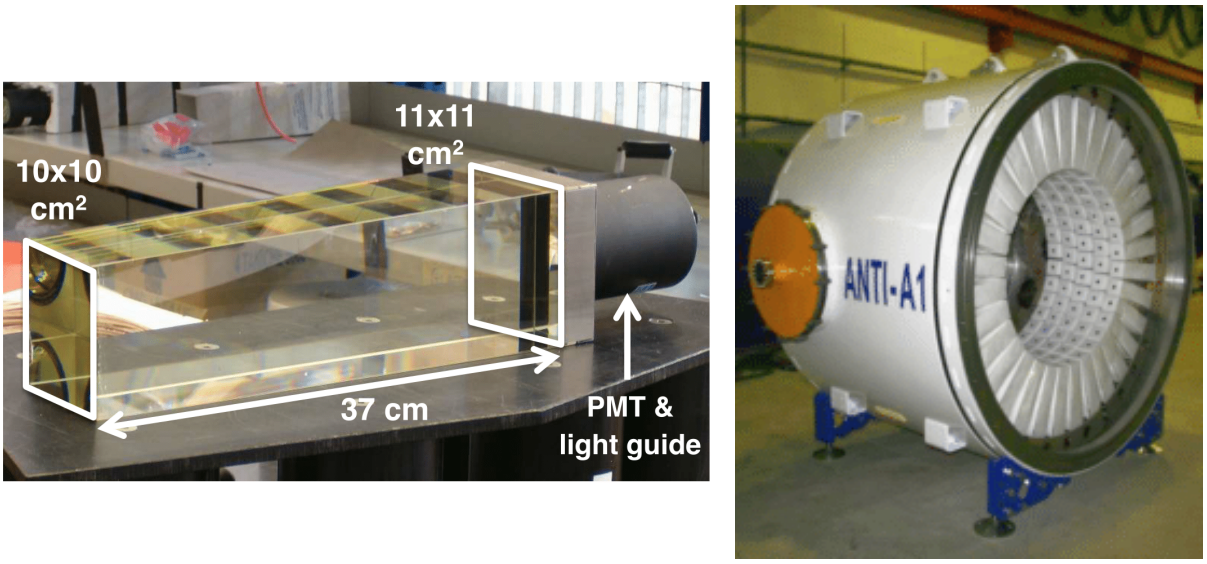

Figure 2.6: *Left: A module from the OPAL calorimeter, without wrapping and with reinforcement plates at the interface between the glass and the steel flange. Right: Completed LAV1 station before insertion in the beam line. Pictures taken from*[68].

The NA62 LAV detector reuses lead-glass blocks recycled from the OPAL electromagnetic calorimeter barrel[72]. The modules consist of blocks of lead glass (75% PbO). Electromagnetic showers in the lead glass are detected via the Cherenkov light produced. The front and rear faces of the blocks measure about 10×10 cm^2 and 11×11 cm^2 , respectively. The blocks are 37 cm in length and each block is read out at the back side by a 76 mm diameter photomultiplier (PM), which is optically coupled via a 4 cm long cylindrical light guide.

A LAV station is made by arranging these modules around the perimeter of the sensitive volume of the experiment, with the blocks aligned radially to form an inward-facing ring (Figure 2.6). Multiple rings are used in each station in order to provide the depth required for the efficient detection of incident particles. The modules in successive rings are staggered in azimuth while the rings are spaced longitudinally by about 1 cm.

Particles incident on any station are intercepted by blocks in at least three rings, for a total minimum effective depth of 21 X_0. Most incident particles are intercepted by four or more blocks (at least 27 X_0). The time resolution for 1 GeV photons is about 1 ns.

Liquid Krypton calorimeter (LKr)

NA62 reuses the former NA48 liquid krypton calorimeter, which is fully described in the NA48 detector paper[73]. The LKr is a quasi-homogeneous calorimeter filled with about 9000 litres of liquid krypton at 120 K, housed inside a cryostat. The calorimeter extends from the beam pipe ($r \approx 8$ cm) to a radius of 128 cm; its depth is 127 cm, corresponding to 27 X_0. The sensitive area is about 7 m^3 divided into 13248 longitudinal cells with a cross section of about 2×2 cm^2. The cells are formed by Cu-Be electrodes aligned along the longitudinal axis of the experiment, and with a zig-zag shape to avoid inefficiencies when a particle shower is very close to the anode (Figure 2.7). The signals are read out by boards with fast analog-to-digital converters (FADC)

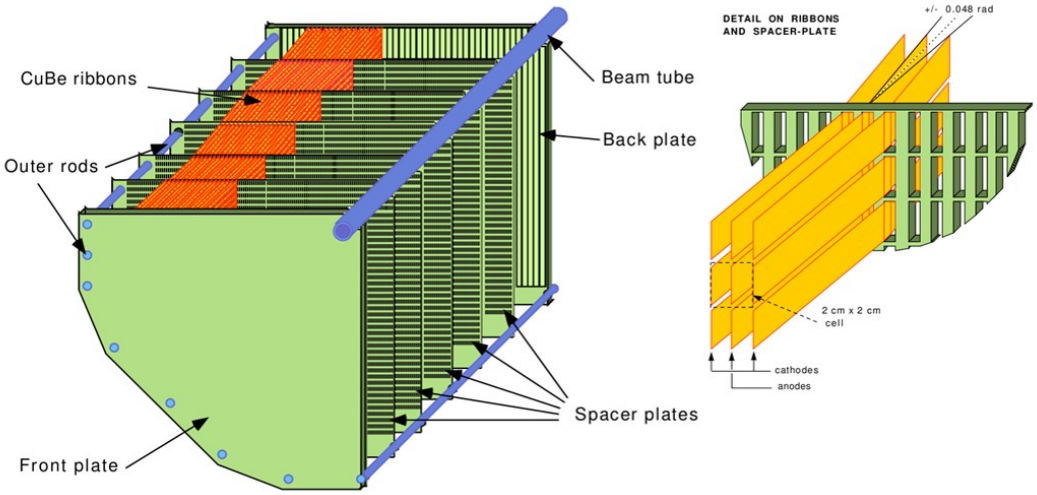

Figure 2.7: *Left: Schematic of the calorimeter structure (one quadrant). Right: Detail of the calorimeter cells. Pictures taken from*[68].

providing the magnitude and time of the energy deposit.

Clusters are defined as the sum of the energy in all the cells in a box around a peak in time and space. The cluster energy is then the sum of energies in each cell and its position in the center of gravity of the cluster, computed as the weighted sum of the coordinates of each cell with the energy deposited in it. The spatial resolution measured in a 3×3 box can be parametrized as:

$$\sigma_y = \sigma_x = \left(\frac{4.2}{\sqrt{E[\mathrm{GeV}]}} \oplus 0.6 \right) \ \mathrm{mm}, \tag{2.2}$$

where the first term is given by the statistical fluctuation of the particles in the shower and the second one is due to the size of the cells. In the NA62 setup the energy resolution is degraded with respect to the value reported in the NA48 detector paper[73], mainly due to the presence of a non-linear energy response and of extra material upstream of the calorimeter. For a typical energy of about 20 GeV the spatial resolution is 1.1 mm in each coordinate. The energy resolution for an 11×11 box is:

$$\frac{\sigma(E)}{E} = \frac{4.8\%}{\sqrt{E[\mathrm{GeV}]}} \oplus \frac{11\%}{E[\mathrm{GeV}]} \oplus 0.9\%, \tag{2.3}$$

with the usual parametrization containing a statistical term, whose main contribution is the lateral leakage of the shower outside the box, a noise term due to the electronics and a constant term accounting for non-linearity and calibration effects.

Intermediate-ring calorimeter (IRC)

The intermediate-ring calorimeter shown in Figure 2.8-left is a lead/scintillator shashlyk calorimeter in the shape of an eccentric cylinder surrounding the beam pipe upstream of the LKr. The detector has an outer diameter of 290 mm and is centered on the z axis. The central bore has

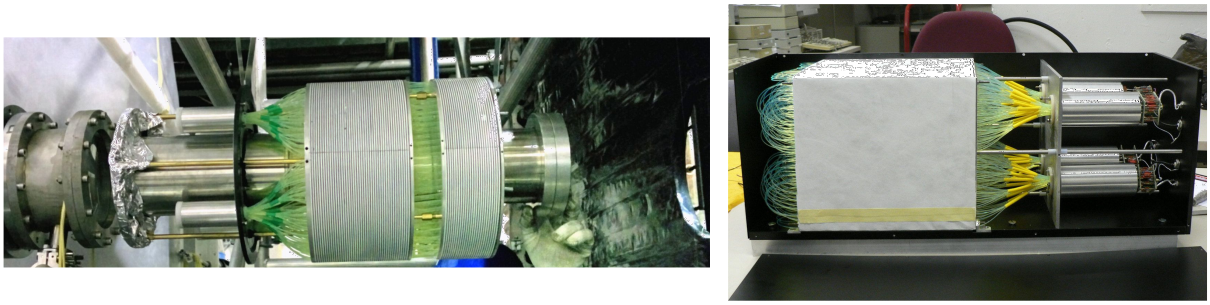

Figure 2.8: *Left: Picture of the IRC during installation, prior to wrapping for light tightness. The upstream and downstream modules are clearly visible with the beam incident from the right. Right: Picture of the SAC after completion of assembly. Pictures taken from*[68].

a diameter of 120 mm with an offset of 12 mm towards positive x to account for the beam deflection by the spectrometer magnet (Figure 2.4).

The IRC is divided into two longitudinal modules, with the upstream and downstream modules of 89 and 154 mm depth, respectively. The modules are spaced by 40 mm. To minimize the material in front of the sensitive volume, the IRC incorporates the corresponding segment of the beam vacuum tube as its inner support cylinder.

The upstream and downstream modules contain 25 and 45 ring-shaped layers, respectively. Each layer consists of a 1.5 mm thick lead absorber and a 1.5 mm thick scintillator plate. The total depth for both modules is 19 X_0.

The four channels of the IRC are read out using both TDC and FADC systems.

Small-angle calorimeter (SAC)

The small-angle calorimeter shown in Figure 2.8-right consists of 70 plates of lead and 70 plates of injection-molded plastic scintillator, both with transverse dimensions of 205 × 205 mm^2 and a thickness of 1.5 mm. The scintillation light is read out by 240 1 mm diameter WLS fibres. Each fibre is bent into a U shape and threaded through two holes, allowing readout of both ends at the back of the detector. Because the scintillator plates have no transverse segmentation, the four readout channels are optically connected, and the SAC is effectively a single-channel detector with a total depth of 19 X_0 and energy resolution of

$$\frac{\sigma(E)}{E} = \frac{8.8\%}{\sqrt{E[\text{GeV}]}} \oplus \frac{7.1\%}{E[\text{GeV}]}. \tag{2.4}$$

The detector is installed inside the beam vacuum towards the end of the beam pipe after the dipole magnet, which deflects the remaining charged particles to the beam dump (Figure 2.4). To guarantee that photons incident on the SAC along the z axis do not traverse the detector along a WLS fibre for more than 10 cm (half of the active length) without encountering any of the lead converters, the SAC is aligned at a 23 mrad angle to the z axis in the horizontal plane.

The four channels of the SAC are read out using both TDC and FADC systems.

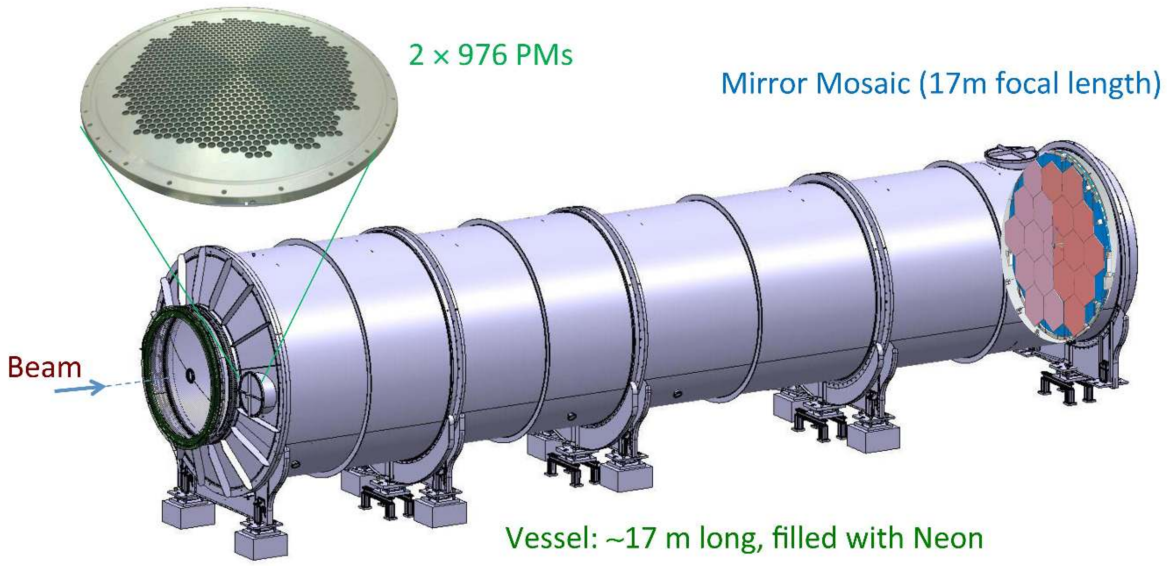

Figure 2.9: *Schematic view of the RICH detector[68]: the hadron beam enters from the left and travels throughout the length of the detector in an evacuated beam pipe. A zoom on one of the two disks accommodating the light sensors (PMs) is shown on the left; the mirror mosaic is made visible through the neon container (vessel) on the right.*

2.7 Ring imaging Cherenkov counter (RICH)

The RICH detector is designed to separate pions from muons between momenta of 15 and 35 GeV/c providing a muon suppression factor of at least 100 as part of the O(10^7) overall rejection factor needed for the $K^+ \to \pi^+\nu\overline{\nu}$ measurement. In order to have full efficiency for a 15 GeV/c momentum pion, the threshold should be about 20% smaller or 12.5 GeV/c, corresponding to $(n-1) = 62\times10^{-6}$. This matches almost exactly the refractive index at atmospheric pressure and room temperature of neon gas that has been chosen as radiator medium. The RICH measures the pion crossing time with a resolution of about 100 ps, thus providing a possible reference time for charged tracks.

The RICH radiator is a 17.5 m long cylindrical vessel filled with neon gas (Figure 2.9). The vessel consists of four sections of gradually decreasing diameter and different lengths. At the upstream end the vessel is about 4.2 m wide to accommodate the photomultiplier flanges outside the active area of the detector. The diameter of the last vessel element is 3.2 m, which is sufficient to house the mirrors and their support panel.

The active area of the detector extends to a radial distance of 1.1 m from the beam axis at the RICH entrance and to 1.4 m at the exit window. The entrance and exit windows have a conical shape and are made of aluminium with a thickness of 2 and 4 mm respectively. The entrance window is the only separator between the decay vacuum volume and the RICH radiator gas volume. A lightweight aluminium tube, connected to the decay-tank vacuum, passes centrally through the vessel.

A mosaic of 20 spherical mirrors is used to reflect the Cherenkov light cone into a ring on the PM array in the mirror focal plane. To avoid absorption of reflected light by the beam pipe

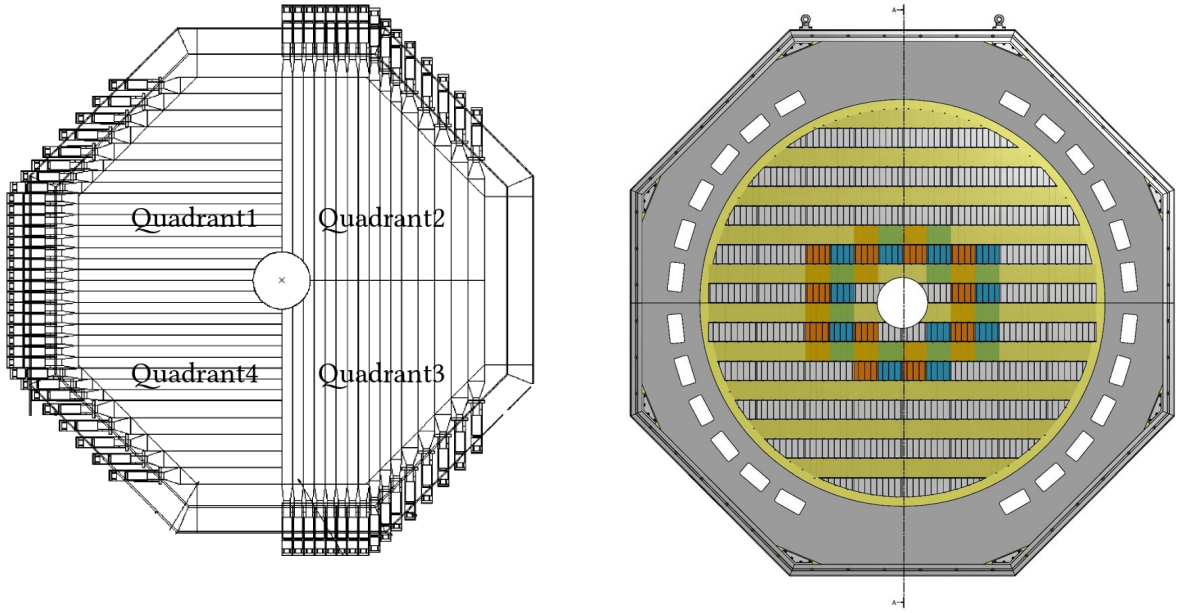

Figure 2.10: *Left: Drawing of the CHOD detector. Half sections of the horizontal and vertical planes are shown, with the beam traversing at the centre of the detector. Right: The NA62CHOD detector mounted on the front face of LAV12 (white blocks forming an annular shape). Pictures taken from*[68].

the mirrors are divided into two spherical surfaces: one with the centre of curvature to the left and one to the right of the beam pipe. The total reflective surface exceeds 6 m^2.

The mirrors have a nominal radius of curvature of 34 m and hence a focal length of 17 m. The mosaic includes 18 mirrors of regular hexagonal shape (350 mm side) and two half mirrors. The two latter ones are used in the centre and have a circular opening to accommodate the beam pipe. The mirrors are made from 25 mm thick glass substrate coated with aluminium.

2.8 Charged particle hodoscopes (CHOD, NA62CHOD)

The NA62 setup includes a scintillator detector system called the charged particle hodoscopes. They cover the lateral acceptance downstream of the RICH and upstream of the LKr calorimeter defined by the LAV12 detector inner radius (1070 mm) and the IRC detector outer radius (145 mm). Their main function is to provide an input for the L0 trigger when at least one charged particle crosses the annulus with the dimensions defined above.

The system consists of the CHOD detector from the former kaon experiment NA48[73] and the newly constructed NA62CHOD detector optimized for the high intensity conditions of NA62 (see Figure 2.10). The CHOD and the NA62CHOD are located, respectively, downstream and upstream of the LAV12 detector, about 700 mm apart in the longitudinal direction. They are operated simultaneously and independently.

The CHOD exploits a high-granularity design based on coincidence of signals in two planes of scintillator strips, suitable to provide track timing with 200 ps precision. The two consecutive

planes are made of 64 vertical and 64 horizontal plastic scintillator strips of 20 mm (0.10 X_0) thickness. Each strip is read out at one end by a photomultiplier through a Plexiglas light guide. The 128 counters are assembled into 4 quadrants of 16 strips in each plane. The strip lengths vary from 1210 mm (inner counters) to 600 mm (outer counters) forming an octagon of 1210 mm apothem. The strip widths are 65 mm in the central region close to the beam, where the particle flux is higher, and 99 mm in the outer region. The radius of the central hole crossed by the beam pipe is 128 mm.

The NA62CHOD active area is an array of 152 plastic scintillator tiles of 30 mm thickness covering an annulus with inner (outer) radii of 140 mm (1070 mm). The scintillation light is collected and transmitted by wavelength shifting fibers to a set of 304 SiPM pairs. The signal from each SiPM is shaped by a constant fraction discriminator (CFD) and are read out by a 512-channel TEL62 board equipped with 4 TDC mezzanies. The time resolution of the NA62CHOD signals is of $\mathcal{O}$(1 ns).

The subdivision of the acceptance surface into tiles leads to an optimized distribution of hit rates, and different groups of tiles can be selected to contribute to specific trigger requirements. The tiles are 108 mm high (except for 12 tiles near the external edge); laterally most tiles are either 134 mm or 268 mm wide. The tile centres are spaced vertically by 107 mm, resulting in a 1 mm overlap. The total thickness of the detector in the active area is 0.13 X_0.

2.9 Hadron calorimeter (MUV1, MUV2)

The hadron calorimeter is a sampling calorimeter made from alternating layers of iron and scintillator corresponding to about 8 nuclear interaction lengths. The calorimeter is divided into two independent detectors: the front detector (MUV1), newly built for the NA62 experiment with a fine transverse segmentation to better disentangle hadronic and electromagnetic shower components, and the back detector (MUV2) inherited from the NA48 experiment[73].

The MUV1 detector consists of 24 layers of 26.8 mm thick steel plates, corresponding to a total thickness of 4.1 interaction lengths (including the scintillating material). The innermost 22 layers have outer dimensions of 2700 $\times$ 2600 mm^2 while the first and the last layer are larger to cover the readout fibres and to serve as support of the whole structure. The distance between consecutive iron layers is 12 mm.

The iron plates are interleaved with 23 layers of scintillator strips of 9 mm thickness and 60 mm width (54 mm width for the four inner strips which end at the beam pipe). Consecutive layers of scintillators are alternately aligned in the horizontal and vertical direction, resulting in 12 layers with horizontal and 11 layers with vertical strip direction. Most of the strips have a length of 2620 mm and span the whole transverse extension of the detector. The four outer strips are shorter by up to 240 mm to accommodate the support structure. The six horizontal and eight vertical strips at or close to the beam pipe are split in two strips of half length to accommodate the pipe and the high particle rate close to the beam, respectively.

The strips are read out by wave-length-shifting (WLS) scintillating fibres connected to PMs. Each scintillating strip has two grooves in its longitudinal direction separated by 30 mm, which contain the WLS fibres and optical glue. The detector in total has 176 channels.

The MUV2 detector is the refurbished front module of the NA48 hadron calorimeter. Similarly to the MUV1 detector, it is built as a sandwich calorimeter and consists of 24 iron plates of 25 mm thickness, each followed by a layer of plastic scintillators.

Each scintillator plane consists of 44 scintillating strips with each strip spanning half the calorimeter. The strips are 1300 mm long, 119 mm wide, and 4.5 mm thick. The two central strips of each half-plane are shaped on one end to enclose the central hole for the beam pipe. The strips are alternately aligned in the horizontal and vertical directions in consecutive planes. As in the MUV1 detector, the strips with identical alignment are coupled to the same PM but in this case using Plexiglas light guides read out by PMs. In total the MUV2 has 88 readout channels.

The fast pulses from the MUV1 and MUV2 PMs are shaped to differential LKr-like pulse shapes by active NIM modules. The signal are then sent to FADC converters of the same type as for the LKr, where the information about the energy and the time of the event is obtained.

2.10 Fast muon veto (MUV3)

The MUV3 detector, located downstream of the hadron calorimeter behind a 80 cm thick iron wall, provides fast L0 trigger signals and is used for muon identification. It detects charged particles traversing the whole calorimeter system (LKr, MUV1,2 and the iron wall) with a total thickness of over 14 interaction lengths. The MUV3 has a transverse size of 2640 $\times$ 2640 mm^2 and is built from 50 mm thick scintillator tiles, including 140 regular tiles of 220 $\times$ 220 mm^2 transverse dimensions and 8 smaller tiles adjacent to the beam pipe, to sustain the high particle rate near the beam.

Each tile is read out by two 2-inch PMs facing towards the tile. The signal from each PM is fed to a constant fraction discriminator (CFD). The CFD signal is further sent to a TEL62 readout board equipped with 3 TDC boards to accommodate the 296 MUV3 readout channels.

2.11 Peripheral muon veto (MUV0)

The MUV0 detector is a scintillator hodoscope designed to detect π^- emitted in $K^+ \to \pi^+\pi^+\pi^-$ decays with momenta below 10 GeV/c, deflected towards positive x by the spectrometer magnet (which adds to the deflection of the K^+ beam induced by the TRIM5 magnet), and leaving the lateral acceptance near the RICH.

The MUV0 is mounted on the downstream flange of the RICH. Its active scintillator area of 1.4 $\times$ 1.4 m^2 covers the periphery of the lateral acceptance (1.545 m $< x <$ 2.945 m, $|y| <$ 0.7 m), and consists of two layers of 48 plastic scintillator tiles with dimensions of 200$\times$200$\times$10 mm^3. The tiles are grouped in 9 super-tiles, each read out with wavelength shifting fibres and a PM using the TEL62/TDC readout.

2.12 Hadronic sampling calorimeter (HASC)

The hadronic sampling calorimeter (HASC) is used for the detection of π^+ emitted in $K^+ \to \pi^+\pi^+\pi^-$ decays with momentum above 50 GeV/c and propagating through the beam holes in

.

Mask	Trigger conditions
L0Control	L0Q1/400
L0PNN	RICH ·NA62CHOD · $\overline{\text{LAV12}}$ · $\overline{\text{QX}}$ · $\overline{\text{MUV3}}$ · $\overline{\text{CALO}}$
L1PNN	KTAG ·$\overline{\text{LAV}}$· STRAW

Table 2.2: *Definition of the conditions comprising the PNN trigger chain and the minimum bias control trigger downscaled by 400. No L1 conditions are applied to the control trigger.*

the centres of the straw chambers. The detector is located downstream of MUV3 and the BEND dipole magnet (Figure 2.4) which sweeps these pions out of the K^+ beam towards negative x. The detector covers the lateral acceptance of -0.48 m $< x < -0.18$ m, $|y| < 0.15$ m.

The HASC is constructed of 9 identical modules. The active element of a module is a sandwich of 60 lead plates (16 mm thick) interleaved with 60 plates of scintillator (4 mm thick) of 100×100 mm^2 transverse dimensions. Each module is organized in 10 longitudinal readout sections. Each scintillator tile is optically coupled to WLS optical fibres, read out by 3×3 mm^2 SiPM sensors.

2.13 Trigger

The total rate of incoming particles in the NA62 detector is 750 MHz. The resulting event rate of 10 MHz requires a highly selective trigger and data acquisition (TDAQ) system. Two levels of trigger logic are used in the 2016 data taking: a hardware trigger (L0) filtering events based on inputs from a small set of fast subdetectors with a maximum output rate of 1 MHz; a software trigger (L1) further reducing the output rate to 100 kHz using information from individual sub-detectors.

The sub-detectors participating in the L0 trigger generate 64 bit words called primitives, which contain time and detector-specific information for each event. The primitives are then sent to the FPGA-based L0 Trigger Processor (L0TP) which checks the time alignment of the primitives asynchronously generated by the detectors. The time alignment is based on information contained in the primitive data, namely a 25 ns precision time-stamp (32 bit) and a 100 ps precision fine time. The trigger processor verifies the relevant matching conditions taking into account the time resolution of each source, as measured at the trigger level. A L0 trigger is issued when a set of primitives matches one of the predetermined configurations (masks). The following primitive definitions are used as input to the L0TP in 2016:

– **L0Q1**: tags charged-particle decays. Positive primitives are generated when a coincidence between the horizontal and the vertical CHOD planes is detected. The L0Q1 condition is used as a control trigger to compute the trigger efficiencies of the PNN trigger chain;

– **L0RICH**: tags charged tracks above the Cherenkov threshold. Positive primitives are generated based on clusters of hits in time;

- **L0NA62CHOD**: a primitive is generated if at least 1 and not more than 4 hits are present in the NA62CHOD;
- **L0QX**: primitives are generated if there are hits in opposite quadrants in the NA62CHOD;
- **L0MUV3**: tags events with muons. The primitives based on tile multiplicities can be used either as a positive or as a veto condition in the trigger logic;
- **L0LAV12**: tags events with photons or muons within the geometrical acceptance. A LAV trigger primitive is generated for events containing signals from one or more LAV blocks. Signals arriving close in time from different blocks are assumed to be originated from the same event, so they generate a single primitive. Only station 12 of the LAV detector is used in the L0 trigger;
- **L0CALO**: a primitive is generated if there is more than 20 GeV energy deposition in the LKr.

The L0PNN mask used all of the above conditions to trigger events with single non-muon track and no extra activity in the event. The time of the L0RICH primitive is used as a time reference for L0PNN mask. Events are kept if: no multiplicity in-time with the reference is found in LAV12 ($\overline{\text{L0LAV12}}$) and the LKr ($\overline{\text{L0CALO}}$); a charged particle consistent with a single-track topology is detected in the NA62CHOD ($\overline{\text{L0NA62CHOD}} \cdot \overline{\text{L0QX}}$) and no MUV3 signal is present ($\overline{\text{L0MUV3}}$). The combination $\text{L0NA62CHOD} \cdot \overline{\text{L0LAV}} \cdot \overline{\text{L0QX}} \cdot \overline{\text{L0MUV3}}$ ($'\cdot'$ means logical AND and the overline logical NOT) will be referred to as L0COMB in the following.

The following L1 software trigger algorithms were used during the 2016 data taking

- **L1KTAG**: minimum of four out of the eight KTAG sectors in coincidence and within ± 10 ns of the L0 trigger time;
- **L1LAV**: no more than two hits in the whole LAV system within ± 10 ns of the L0 trigger time. All twelve LAV stations are used in the L1 trigger;
- **L1STRAW**: the following conditions are applied to reject multi-track events reconstructed either outside the fiducial decay region or outside the track momentum range:
  - ⋆ longitudinal track momentum P_Z smaller than 50 GeV/c;
  - ⋆ track closest distance of approach (CDA) to the beam axis smaller than 200 mm;
  - ⋆ vertex longitudinal position at the CDA smaller than 180 m;
  - ⋆ if a pair of tracks is reconstructed, their CDA must be larger than 30 mm;

The L1KTAG, L1LAV and L1STRAW are applied sequentially on top of each other to define the L1PNN mask. During the 2016 data taking a fraction of L0 triggers, called Auto Pass (AP) and corresponding to 2% of the total bandwidth and 25% of the PNN mask, are directly saved on tape and reserved for offline trigger studies.

The complete set of criteria entering the L0PNN and L1PNN trigger masks (Table 2.2) define the PNN trigger chain.

3 Data and MC samples

3.1 The data sample in 2016

The $K^+ \to \pi^+\nu\overline{\nu}$ analysis is performed on a data sample taken from mid-September to mid-October 2016 after the complete NA62 detector was commissioned. The analysis uses data collected with the PNN and control trigger streams and processed with the NA62 Software Framework[74]. During the 2016 $\pi\nu\overline{\nu}$ data taking period a typical intensity of 10^{12} protons per pulse were utilized. A total of 121 runs containing 82 000 SPS spills were collected, corresponding to 8×10^{16} protons on target, with a good run containing about one thousand spills. After data quality assessment and rejection of bad spills, a total of 51 000 spills are used for the $K^+ \to \pi^+\nu\overline{\nu}$ data analysis.

The criteria used to define a bad spill vary across detectors, typically related to low detector efficiency caused by either hardware or readout problems. The main detectors contributing to the bad spill rejection are LKr (∼15000), KTAG (∼3000), LAV (∼2000), RICH (∼1600) and CHANTI (∼1500). The majority of those spills have critical error in the TEL62 readout boards. The very high number of spill rejected by the LKr data quality assessment is related to strict conditions on the noise level in the LKr needed in the analysis of the 2016 data.

3.2 Monte Carlo samples

A set of kaon decays are generated using MC simulation and are used for signal, normalization and background studies. Each decay is generated in the kaon rest frame according to the corresponding matrix element and form factor parametrization (if applicable). The decay products are then boosted to the laboratory frame. The incident kaon trajectory and momentum are generated taking into account the beam profile as measured in data. The NA62 detector acceptance is simulated using the GEometry AND Tracking (GEANT4) package[75], which includes full detector geometry and material description, stray magnetic fields and a simulation of the

Decay channel	Simulated events [10^6]
$K^+ \to \pi^+\nu\overline{\nu}$	8
$K^+ \to \pi^+\pi^0(\gamma)$	47
$K^+ \to \mu^+\nu_\mu(\gamma)$	15
$K^+ \to \pi^+\pi^- e^+\nu_e$	382
$K^+ \to \pi^0 e^+\nu_l$	39
$K^+ \to \pi^0\mu^+\nu_l$	27
$K^+ \to \pi^+\gamma\gamma$	0.8

Table 3.1: *Definition of the MC samples used for signal and background estimation in the $K^+ \to \pi^+\nu\overline{\nu}$ analysis. All numbers correspond to events simulated in the decay region with longitudinal position between 105 and 165 m.*

kaon beam line.

The $K^+ \to \pi^+\nu\overline{\nu}$ process is generated using the total phase-space integral and normalized differential decay rate defined as

$$\frac{1}{\Gamma}\frac{d\Gamma}{dz} = \frac{\lambda_\pi^3}{\mathcal{I}_\nu^+}\left|\frac{f_+^{K^+\pi^+}(z)}{f_+^{K^+\pi^+}(0)}\right|^2, \quad \mathcal{I}_\nu^+ = \int_0^{(1-r_\pi)^2} dz\lambda_\pi^3\left|\frac{f_+^{K^+\pi^+}(z)}{f_+^{K^+\pi^+}(0)}\right|^2, \tag{3.1}$$

with $r_\pi = m_{\pi^+}/m_{K^+}$, $\lambda_\pi = \sqrt{r_\pi^4 - 2(z+1)r_\pi^2 + (z-1)^2}$, and $z = q^2/m_{K^+}^2$ with q^2 the invariant mass of the two neutrinos related to the π^+ momentum via $|\mathbf{p}_\pi| = m_{K^+}\lambda_\pi/2$, or $z = r_\pi^2 + 1 - 2\sqrt{r_\pi^2 + \mathbf{p}_\pi^2/m_{K^+}^2}$.

The form-factor $f_+^{K^+\pi^+}(z)$ is extracted from $K^+ \to \pi^0 l^+\nu_l$ (K_{l3}) decays using its quadratic parametrization[76]. The form-factor slopes are re-scaled to account for the isospin corrections inducing differences between the K_{l3} decays and the signal. The form-factors at the origin are obtained by using the theoretical ratio[34]

$$r_K = \frac{f_+^{K^+\pi^+}(0)}{f_+^{K^0\pi^+}(0)} = 1.0015 \pm 0.0007. \tag{3.2}$$

The following decays were generated for normalization and background studies:

- $K^+ \to \pi^+\pi^0(\gamma)$: with the internal bremsstrahlung and direct dipole emissions[77,78,79] included. This MC sample was used both for background studies and signal normalization.
- $K^+ \to \mu^+\nu_\mu(\gamma)$: with the form factor parametrized within the CHPT framework[80,81] and improvements of the radiative spectrum description at very low photon energies[82];
- $K^+ \to \pi^0 l^+\nu_l$ ($l = \mu, e$): with the form factor parametrized within the CHPT[83]. Radiative corrections[82] are also implemented;
- $K^+ \to \pi^+\pi^- e^+\nu_e$: with the most precise description of the form factors[84]. Attraction

between opposite-charged pions in the final state and real photon emission are included in the simulation using the PHOTOS package[85].

– $K^+ \to \pi^+\gamma\gamma$: with included one-loop unitarity corrections[86] of $O(p^6)$ in CHPT.

The summary of the statistics generated for the samples described above is shown in Table 3.1. The number of simulated $K^+ \to l^+\pi^0\nu_l$, $K^+ \to \mu^+\nu_\mu$ and $K^+ \to \pi^+\pi^0$ events is far less than what is available in data. However, this is sufficient to show that the $K^+ \to l^+\pi^0\nu_l$ decays constitute negligible fraction of the $K^+ \to \pi^+\nu\overline{\nu}$ background, to measure the $K^+ \to \pi^+\pi^0$ acceptance and kinematic tails for both $K^+ \to \pi^+\pi^0$ and $K^+ \to \mu^+\nu_\mu$.

In all samples accidental activity is added in GTK and KTAG, assuming 300 MHz integrated beam intensity and using a momentum template of pileup beam particles extracted from data. No accidental activity is simulated in the detectors downstream of the final collimator.

4

Event selection

The $K^+ \to \pi^+ \nu\overline{\nu}$ ($K_{\pi\nu\overline{\nu}}$) decay signature is one track in the initial and one track in the final state with two missing neutrinos. The main kinematic variable is the squared missing mass $m^2_{miss} \equiv (P_K - P_{\pi^+})^2$, where P_K and P_{π^+} are the 4-momenta of the K^+ and π^+, respectively. The two neutrinos carry away a large fraction of the momentum and the missing mass distribution is broad as shown in Figure 4.1.

The analysis is performed in two separate regions: Region 1 (R1) between the $K^+ \to \mu^+\nu_\mu$ ($K_{\mu\nu}$) and $K^+ \to \pi^+\pi^0$ ($K_{\pi\pi}$) contributions and Region 2 (R2) between the $K_{\pi\pi}$ and $K^+ \to \pi^+\pi^+\pi^-$ ($K_{\pi\pi\pi}$) contributions. The main backgrounds entering those regions are $K_{\mu\nu}$ and $K_{\pi\pi}$ decays through non-gaussian resolution and radiative tails; $K_{\pi\pi\pi}$ through non-gaussian resolution; $K^+ \to \pi^+\pi^- e^+\nu_e$ (K_{e4}) and $K^+ \to l^+\pi^0\nu_l$ (K_{l3}) decays with neutrinos in the final state; upstream background consisting of K^+ decays upstream of the GTK3 station and inelastic beam-detector interactions. Each of the background processes requires different rejection procedure depending on its kinematics and type of charged particle in the final state. The full event selection procedure is described in the following.

The quality preselection is described in Section 4.1. The reconstruction of π^+ and K^+ candidate tracks is given in Sections 4.2 and 4.3. Single-track K^+ decays are obtained in Section 4.4. Finally, the selection of good $K_{\pi\nu\overline{\nu}}$ decay candidates is detailed in Section 4.5.

4.1 Preselection

General conditions are applied to select only events with good quality of the reconstruction. To pass the preselection an event must have:

- no global readout errors in any of the detectors;
- at least one CHOD hit;
- at least one and no more than 2000 fired LKr cells;

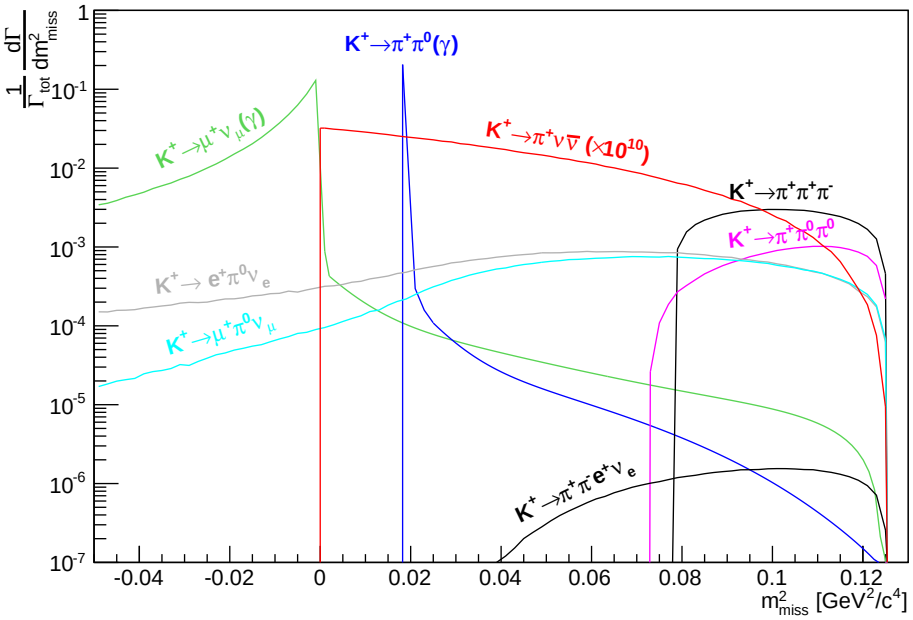

Figure 4.1: *Differential decay width for kaon decays relevant to the $K^+ \to \pi^+\nu\overline{\nu}$ measurement[87]. The Standard model expectation of the signal distribution[36] is shown in red, multiplied by 10^{10} for visibility.*

– either the control or the PNN trigger bit set at level 0;

– at least one and no more than 10 tracks reconstructed by the straw spectrometer (Section 4.2).

Two corrections, α and β, are applied to the reconstructed momentum of each track:

$$P_{\text{corr}} = (1+\beta)(1+\alpha\cdot q\cdot P_{\text{uncorr}})\cdot P_{\text{uncorr}}. \tag{4.1}$$

Here q is the track charge; α, with a typical value of 10^{-7} MeV^{-1}, is related to geometrical misalignment of the STRAW chambers and depends on the track charge and β, with a typical value of 10^{-3}, is a scale factor corresponding to miscalibration of the magnetic field of the straw spectrometer. Both α and β parameters[88] are determined from a study of fully reconstructed $K_{\pi\pi\pi}$ decays and are stored in a database. They are applied to each track on a burst-by-burst basis.

4.2 Pion candidate track reconstruction

Tracks are reconstructed in the STRAW detector using as reference the average CHOD hit time recorded within ±25 ns from the trigger time to measure the drift time in the straw tubes. Then the drift time T_{drift} is converted to the distance R of a particle trajectory to the anode wire of the hit straw using the $R - T_{\text{drift}}$ relation obtained from a GARFIELD simulation[89].

A so-called view-hit is formed if at least two straw hits in consecutive planes of a chamber view module are compatible with the staggering of the planes. The view-hit position is then converted to a position in the NA62 reference frame using the measured drift distances.

View-hits are combined to give the particle position in each chamber. A pattern recognition algorithm then combines the chamber information to provide candidate tracks which are compatible with the momentum kick of the magnet in the xz-plane. Finally, a recursive Kalman filter technique[90] is used to fit the track trajectory, taking into account the 3-dimensional map of the MNP33 magnetic field and the fringe field outside the dipole volume. Each event must have at least one reconstructed STRAW track. A positively charged track is of *good quality* at selection level if:

- hits are present in all four chambers;
- the χ^2 obtained by the fit described above is smaller or equal to 20;
- the difference between the momentum measured before and after the fit is smaller than 20 GeV/c;
- $|\Delta X'_\pi| \leq 0.3$ mrad and $|\Delta Y'_\pi| \leq 1$ mrad, with $\Delta X'_\pi$ and $\Delta Y'_\pi$ being the difference of the dx/dz and dy/dz slopes of the track measured before and after the track fit, respectively;
- more than 15 and less than 42 straw hits should form the candidate track.
- no vertex can be built with any other non-fake track, where:
  - ⋆ a track is fake, if it is reconstructed with 3 chambers and either has a STRAW hit in common with another track or $\chi^2 > 30$;
  - ⋆ the 2-track vertex is built if the closest distance of approach (CDA) of the tracks is smaller than 15 mm, the longitudinal position Z_{vertex} between 60 and 200 m and the track time difference smaller than 50 ns.

The track must be inside the geometrical acceptance of the subdetectors defined in Table 4.1.

Each track must have associated hit candidates in CHOD, NA62CHOD, RICH and LKr. A track is selected if the associated CHOD time is within ±25 ns of the trigger time.

The time of a downstream particle corresponding to a selected STRAW track is defined as:

$$\mathrm{T}_{\text{downstream}} = \frac{\sum_{j=1}^{4} w_j^{-1} \mathrm{T}_j}{\sum_{j=1}^{\text{ndet}} w_j^{-1}}. \tag{4.2}$$

Here $j = 1, 2, 3, 4$ stands for CHOD, LKr, RICH and STRAW, respectively; $\mathrm{T}_{1,2,3}$ are the times of the matched candidates in CHOD, LKr and RICH, indicated as $\mathrm{T}^{\text{CHOD}}_{\text{track}}$, $\mathrm{T}^{\text{LKr}}_{\text{track}}$ and $\mathrm{T}^{\text{RICH}}_{\text{track}}$ in the following sections; T_4 is the time of the straw spectrometer track as measured by the trailing time of the STRAW hits (also indicated as $\mathrm{T}^{\text{STRAW}}_{\text{track}}$); the weighting factors $w_{1,2,3,4}$ are 0.5, 1, 0.2, 10 ns, respectively, and are proportional to the corresponding detector resolutions.

Detector	z_{pos} [mm]	$(x,y)_{\text{center}}$ [mm]	R_{low} [mm]	R_{high} [mm]
STRAW1	183 508	(101.2,0)	75	1000
STRAW2	194 066	(114.4,0)	75	1000
STRAW3	204 459	(92.4,0)	75	1000
STRAW4	218 885	(52.8,0)	75	1000
RICH front	219 445	(34,0)	101	1100
RICH back	237 326	(2,0)	101	1100
NA62CHOD	238 132	(0,0)	140	1070
LAV12 front	238 313	(0,0)		1070
LAV12 back	238 783	(0,0)		1070
CHOD (V plane)	239 009	(0,0)	125	1100
CHOD (H plane)	239 389	(0,0)	125	1100
IRC	239 700	(0,0)	145	
LKr	241 093	(0,0)	150	1070
MUV1	243 418	(0,0)	130	1100
MUV2	244 435	(0,0)	130	1100
MUV3	246 800	(0,0)	130	1200

Table 4.1: *Geometrical acceptance definition for the various subdetectors. The acceptance is in the area between the two circles centered at* $(x,y)_{\text{center}}$ *and radii* R_{low} *and* R_{high}*. Tracks extrapolated to* z_{pos} *of the front face of the corresponding detector with* $R < R_{\text{low}}$ *or* $R > R_{\text{high}}$ *are rejected.*

Association of STRAW tracks with the CHOD

The STRAW track is extrapolated to the CHOD planes. The variable $\mathbf{X}_{\text{track}}^{\text{CHOD}} = (x,y)$ is the extrapolated position of the track at the vertical (V) and horizontal (H) planes, respectively. The H-V pair associated to the track is found by minimizing the discriminating variable

$$\text{D}_{\text{CHOD}} = \left(\frac{|\mathbf{X}_{\text{H-V}} - \mathbf{X}_{\text{track}}^{\text{CHOD}}|}{2\sigma_{\mathbf{X}}}\right)^2 + \left(\frac{\text{T}^{\text{CHOD}} - \text{T}_{\text{track}}^{\text{STRAW}}}{3\sigma_{\text{T}}}\right)^2 + \left(\frac{t_{\text{V}} - t_{\text{H}}}{3\sigma_{\text{t}}}\right)^2. \qquad (4.3)$$

Here $\mathbf{X}_{\text{H-V}}$ are the (x,y) coordinates of the H-V hits pair; $t_{\text{V,H}}$ is the time of the hits in the vertical and horizontal strips, corrected for the light propagation time of the corresponding H-V intersections; $\text{T}^{\text{CHOD}} = 0.5 \cdot (t_{\text{V}} + t_{\text{H}})$, $\sigma_{\mathbf{X}} = 13$ mm, $\sigma_{\text{T}} = 5.6$ ns, $\sigma_{\text{t}} = 3$ ns. The coefficients in front of the corresponding resolutions optimize the impact of the single contributions of the variables on D_{CHOD} (Figure 4.2-bottom).

The distributions of the variables used in D_{CHOD} are shown in Figure 4.2-top. The pattern observed in the $\mathbf{X}_{\text{H-V}} - \mathbf{X}_{\text{track}}^{\text{CHOD}}$ distribution is due to the CHOD geometrical structure. For each horizontal channel many possible vertical intersections can be found. The distance between

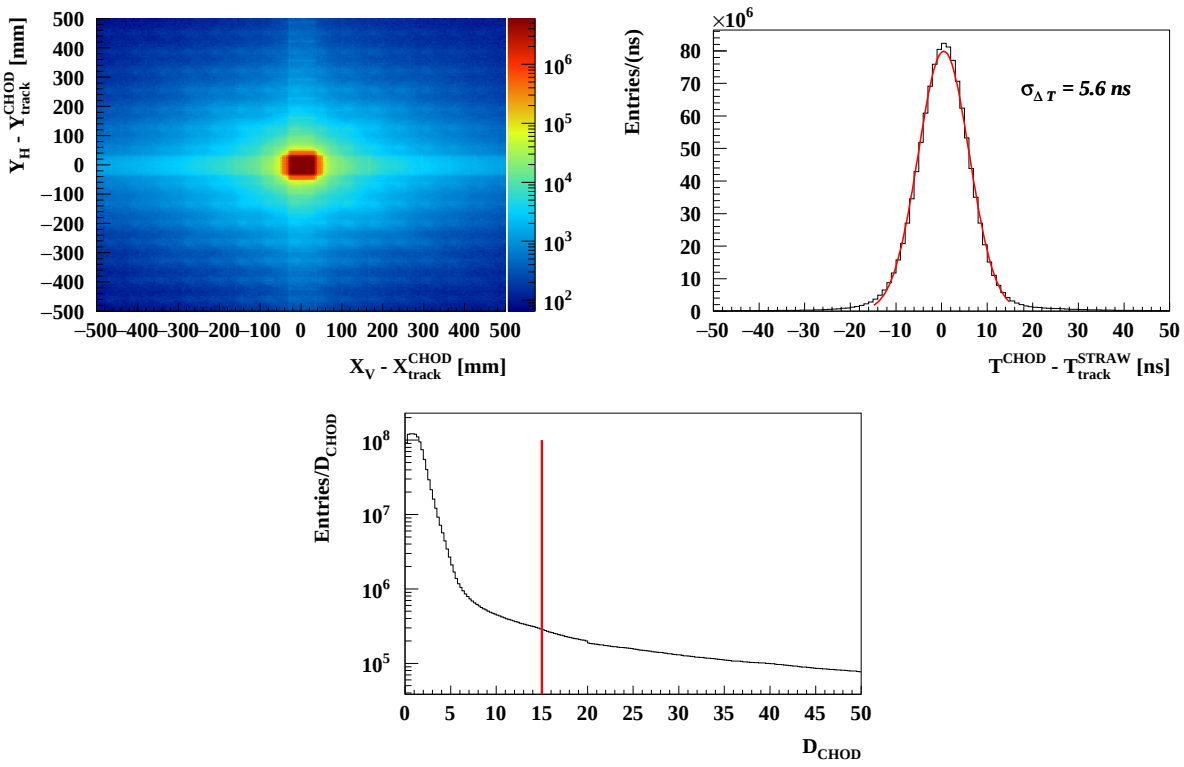

Figure 4.2: *Top left: Distance between the extrapolated position of the STRAW track at the CHOD planes and the corresponding H-V intersections. Top right: Distribution of the time difference between the STRAW track time and the average time of the H-V intersection. The resolution is dominated by the STRAW track time. Bottom: Distributions of the discriminating variable* D_{CHOD}.

two neighbouring strips is varying between 60 and 75 mm in both x and y, causing the grid-like structure of the plot.

The pair of CHOD hits with smallest D_{CHOD} value forms a candidate, which is matched to the track if:

- $D_{CHOD} < 15$;
- T^{CHOD} is within ± 20 ns of T_{track}^{STRAW}.

The CHOD matching efficiency in the $K_{\pi\nu\bar{\nu}}$ MC is 96.9%. The results are consistent with the 96.7% efficiency obtained from one-track events in data.

Association of STRAW tracks with the NA62CHOD

A hit block in the NA62CHOD is associated to each STRAW track using the standard matching tool `SpectrometerNewCHODAssociation`[74]. The tool provides information about the closest block in space to the track extrapolated to the NA62CHOD longitudinal position ($\mathbf{X}_{track}^{NA62CHOD}$).

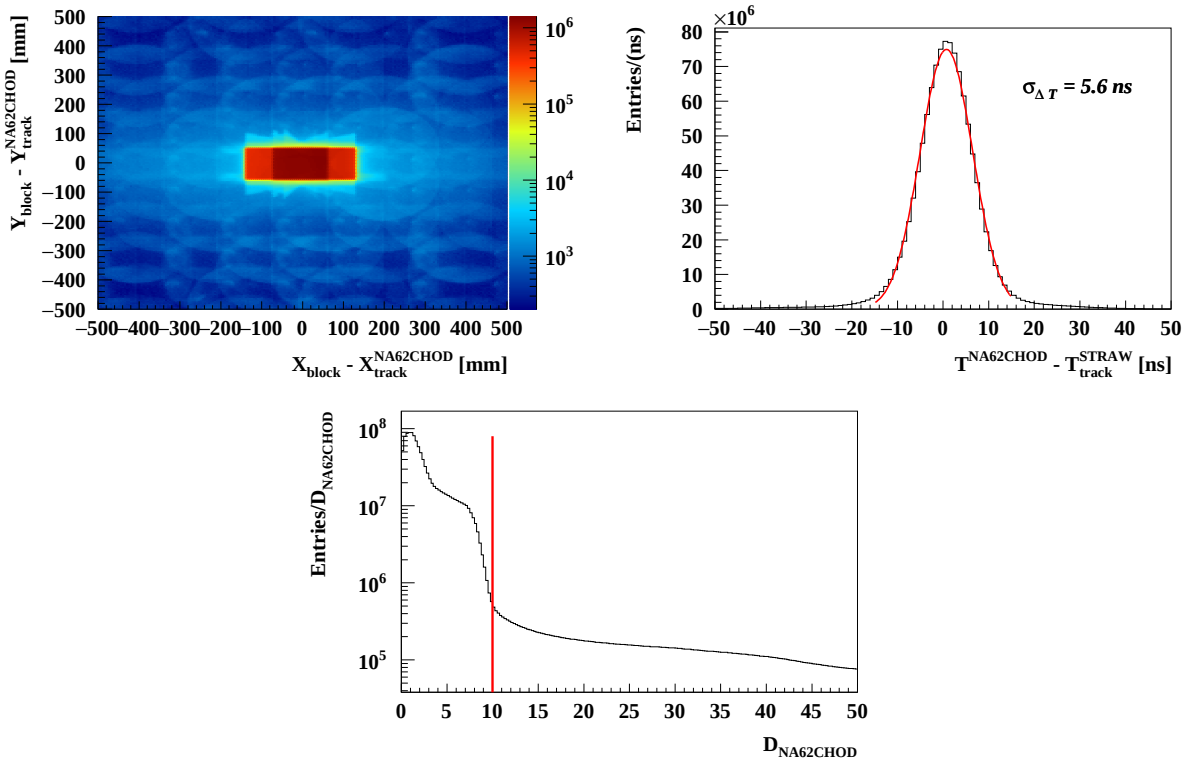

Figure 4.3: *Top left: Distance between the extrapolated position of the STRAW track at the NA62CHOD and the corresponding hit block. Top right: Distribution of the time difference between the STRAW track time and the hit NA62CHOD block. The resolution is dominated by the STRAW track time. Bottom: Distributions of the discriminating variable* $\mathrm{D_{NA62CHOD}}$.

A discriminant is built for the associated block:

$$\mathrm{D_{NA62CHOD}} = \left(\frac{|\mathbf{X}_{\mathrm{block}} - \mathbf{X}_{\mathrm{track}}^{\mathrm{NA62CHOD}}|}{3\sigma_{\mathbf{X}}}\right)^2 + \left(\frac{\mathrm{T}^{\mathrm{NA62CHOD}} - \mathrm{T}_{\mathrm{track}}^{\mathrm{STRAW}}}{2\sigma_{\mathrm{T}}}\right)^2, \qquad (4.4)$$

where $\mathbf{X}_{\mathrm{block}}$ are the (x, y) coordinates of the hit block, $\mathrm{T}^{\mathrm{NA62CHOD}}$ is the time of the associated block, $\sigma_{\mathrm{T}} = 5.8$ ns and $\sigma_{\mathbf{X}} = 16$ mm. The $\mathrm{D_{NA62CHOD}}$ distribution is shown in Figure 4.3-bottom.

The distributions of the variables used in $\mathrm{D_{NA62CHOD}}$ are shown in Figure 4.3-top. The blocks in the NA62CHOD have various sizes in x, while they are all 65 mm along y. This causes the pattern observed in the $\mathbf{X}_{\mathrm{block}} - \mathbf{X}_{\mathrm{track}}^{\mathrm{CHOD}}$ distribution.

The associated block in NA62CHOD is matched to the track if:

- $\mathrm{D_{NA62CHOD}} < 10$;
- $\mathrm{T}^{\mathrm{NA62CHOD}}$ is within ± 5 ns of $\mathrm{T}_{\mathrm{track}}^{\mathrm{CHOD}}$.

The NA62CHOD matching efficiency in the $K_{\pi\nu\bar{\nu}}$ MC is 99%. The same result is obtained from one-track events in data.

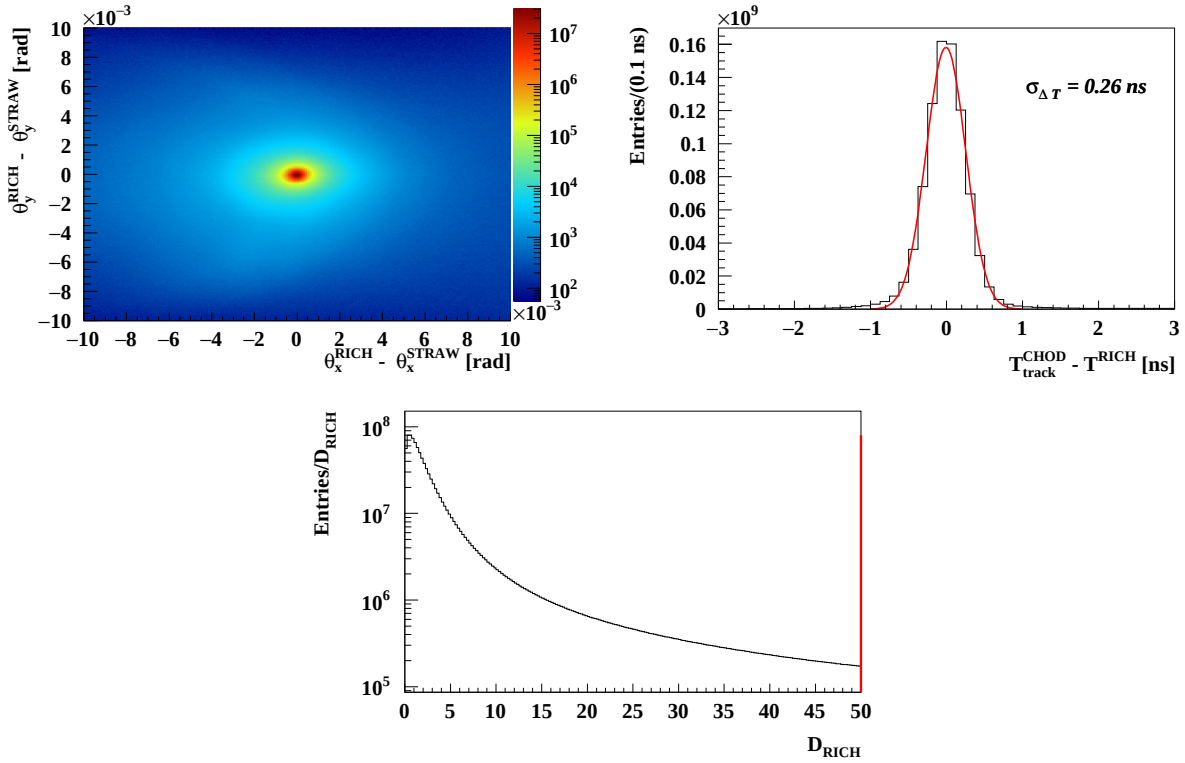

Figure 4.4: *Top left: Difference between the (x,y) track slopes measured by the STRAW and those obtained using the RICH. Top right: Distribution of the time difference between the associated CHOD candidate and the RICH ring candidate. Bottom: Distributions of the discriminating variable* $\mathrm{D_{RICH}}$.

Association of STRAW tracks with the RICH

Two methods are used to search for matching signals in the STRAW and RICH detectors:

1. the standard matching tool `SpectrometerRICHAssociationOutput`[74], where a RICH ring associated to a track is reconstructed using a likelihood algorithm;

2. a standalone reconstruction algorithm where a RICH ring is reconstructed using a single-ring pattern recognition algorithm and then associated to the track.

The likelihood algorithm[91] extrapolates the STRAW tracks to the RICH mirrors, predicting the ring center. The track momentum is the used to calculate the expected ring radius and number of produced hits comprising the ring for each particle hypothesis (π, μ, e). The expectation is compared with the observed RICH hits and the likelihood is provided for each hypothesis.

The implementation of the standalone ring reconstruction algorithm and the ring matching criteria are derived from the procedures reported in[92,93]. The track is extrapolated to the RICH mirror plane ($z = 236\,873$ mm) and virtually reflected onto the focal plane at $z = 202\,873$ mm. $\mathbf{X}_{\mathrm{PM}}$ indicates the (x, y) coordinates at the focal plane. Hits in the RICH are grouped using a ± 5 ns time window to form a ring candidate with a time $\mathrm{T^{RICH}}$. For each ring candidate only the hit PM's between 80 and 200 mm away from $\mathbf{X}_{\mathrm{PM}}$ and within ± 2 ns of the ring time, $\mathrm{T^{RICH}}$,

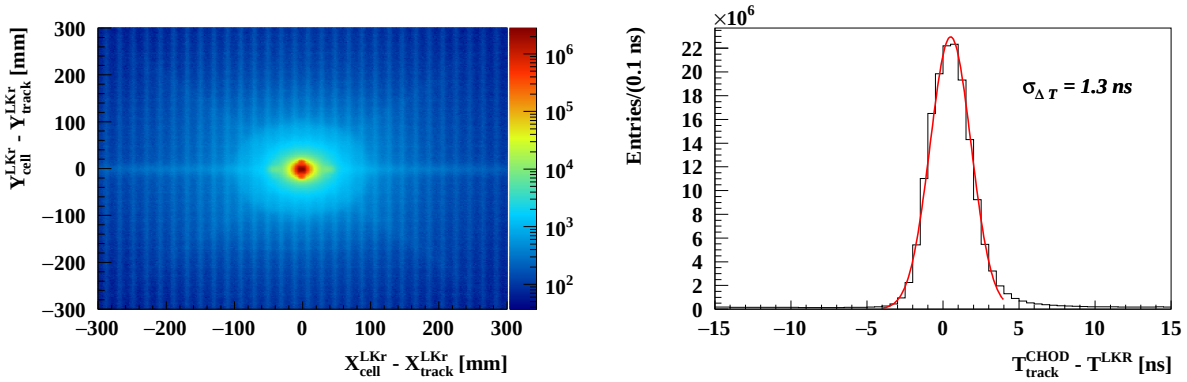

Figure 4.5: *Left: Distance between the extrapolated position of the STRAW track at the LKr and the corresponding LKr cluster. Right: Distribution of the time difference between the CHOD track time and the LKr cluster time.*

are retained. The fit of the ring is then repeated if more than 4 hits remain, otherwise the ring candidate is discarded. The fit is performed using the hit positions corrected for the relative Jura−Saleve rotation, as measured by the mirror alignment procedure[94] (values taken from the RICH database). The χ^2 of the fit is evaluated assuming 4.7 mm resolution ($\approx$ half of the PM active area) on the hit position. If the fit probability is below 0.005, the hit with the largest contribution to the χ^2 is discarded and the fit is repeated. The iteration is performed only once and the candidate kept even in case of further failures of the χ^2 test.

The best standalone ring associated to the track is chosen based on

$$\mathrm{D_{RICH}} = \left(\frac{|\mathbf{X}_{\mathrm{center}} - \mathbf{X}_{\mathrm{PM}}|}{\sigma_{\mathrm{X}}}\right)^2 + \left(\frac{\mathrm{T^{RICH}} - \mathrm{T^{CHOD}_{track}}}{2\sigma_{\mathrm{T}}}\right)^2 . \tag{4.5}$$

Here $\sigma_{\mathrm{T}} = 0.3$ ns, $\mathbf{X}_{\mathrm{center}}$ are the (x, y) coordinates of the ring center and $\sigma_{\mathrm{X}} = 3$ mm. The time difference $\mathrm{T^{RICH}} - \mathrm{T^{CHOD}_{track}}$ and the difference between the θ^{RICH} and θ^{STRAW} angles measured by the RICH and STRAW, respectively, are shown in Figure 4.4. The extrapolated position at the RICH PM plane is used for the association instead of the angles, to ensure that the RICH single ring reconstruction is independent on the angle measurement of the STRAW.

The best standalone ring candidate matches the track if:

- $\mathrm{D_{RICH}} < 50$;
- the fit probability is larger than 0.01;
- $\mathrm{T^{RICH}}$ is within ± 2 ns of $\mathrm{T^{CHOD}_{track}}$.

A STRAW track is considered to have a RICH matching if rings are reconstructed either with the likelihood or the standalone ring reconstruction algorithms. The association efficiency is 98.9%, measured with one-track events in data, which is in agreement with the 99% efficiency in the $K_{\pi\nu\bar{\nu}}$ MC.

Association of STRAW tracks with the LKr

Clusters in the LKr are reconstructed by grouping cells within 110 mm from a seed, where a seed is a cell with at least 250 MeV energy deposition and an energy greater than the average of the 8 surrounding cells. The energy of the cluster is the sum of the energy deposits in each cell. The cluster time is the time of the seed. The cluster position is taken as the barycentre of the cells weighted with the energy deposited in the cells. Corrections are applied to the energy and the position of the clusters to handle the presence of dead cells and to treat clusters close in space or in time. The cluster energy is also corrected for non-linearity induced by the online zero suppression. The zero suppression cut of least 50 MeV signal is applied to each LKr cell. The digital filter[95] is then applied to subtract the noise and to evaluate the real energy deposit in the cell. Corrections are applied to the energy and coordinates of all clusters via the `LKrClusterCorrection` tool[74], related to the overall energy scale, non-linearity and LKr alignment. This algorithm is referred to as "standard LKr reconstruction" in the following.

The standard cluster closest to the track position at the LKr front face is associated to the STRAW track if it is:

- less than 100 mm away from the track;
- within ±20 ns of T^{STRAW}_{track};
- within ±6 ns of T^{CHOD}_{track}.

If no cluster is found, an alternative cell-based approach is used:

- the track is extrapolated to the LKr surface ($z = 241\ 093$ mm);
- all readout cells closer than 100 mm to the extrapolated position and within ±40 ns of T^{STRAW}_{track} are clustered together;
- the most energetic cell must have at least 40 MeV energy deposit (after the digital filter is applied);
- the energy of the resulting cluster is the sum of the cell energies and is corrected for non-linearity;
- the cluster time T^{LKr} is defined as the time of the most energetic cell;
- T^{LKr} must be within ±20 ns of T^{STRAW}_{track} and ±6 ns of T^{CHOD}_{track} (Figure 4.5).

If no matching is found with either of the above methods the track is not considered. The LKr association efficiency is 97.2% obtained from MC simulation consistent with the 96.5% obtained from one-track events in data. A STRAW track matched in the CHOD, NA62CHOD, RICH and LKr is referred to as *pion candidate* track and its time $T_{downstream}$ as T_π in the following.

Calorimetric energy reconstruction

For each selected pion candidate track, signals in MUV1 and MUV2 are combined with the measured LKr energy to obtain the total calorimetric energy. The association and measurement of the energy deposited in MUV1,2 and LKr is performed using the standard multi-variate algorithm (MVA) implemented in the tool `SpectrometerCalorimeterAssociation`[96]. The variables provided by the tool to characterize the combined calorimetric cluster are:

- the total energy defined as the sum of associated energies E_{LKr}, E_{MUV1}, E_{MUV2} in LKr, MUV1 and MUV2, respectively ;
- the time of the energy deposit computed as the average time of the energy clusters in the calorimeters;
- the probabilities provided by the MVA of the particle being a muon / pion / positron;
- the definition of a Minimum Ionizing Particle (MIP) signal variable:

$$\mathrm{D_{MIP}} = \frac{1}{3} \cdot \sqrt{\mathrm{D^2_{MIP\text{-}LKr}} + \mathrm{D^2_{MIP\text{-}MUV1}} + \mathrm{D^2_{MIP\text{-}MUV2}}}, \tag{4.6}$$

  with (energies in MeV)

$$\mathrm{D_{MIP\text{-}LKr}} = (E_{\mathrm{LKr}} - E_{\mathrm{MIP\text{-}LKr}})/(1.5 \cdot 54.9) \tag{4.7}$$
$$\mathrm{D_{MIP\text{-}MUV1}} = (E_{\mathrm{MUV1}} - E_{\mathrm{MIP\text{-}MUV1}})/(1.5 \cdot 165.8) \tag{4.8}$$
$$\mathrm{D_{MIP\text{-}MUV2}} = (E_{\mathrm{MUV2}} - E_{\mathrm{MIP\text{-}MUV2}})/(1.5 \cdot 141.1), \tag{4.9}$$

  where $E_{\mathrm{MIP\text{-}LKr}}$, $E_{\mathrm{MIP\text{-}MUV1}}$, $E_{\mathrm{MIP\text{-}MUV2}}$ with numerical values 561.3, 1183.8 and 1042.5 MeV, respectively, are the average energy released by a MIP in the corresponding detector.
- the extra energy in MUV1 and MUV2 not geometrically associated to a track, but within $\pm$15 ns of the energy matched to the track.

The presence of energy deposits in MUV1 or MUV2 is not required. No calorimetric conditions for particle identification are applied at this stage of the analysis. The presented quantities are used in the particle identification algorithm in Section 4.5.2.

4.3 Kaon candidate track reconstruction

Kaon identification

A pion candidate must have at least one in-time kaon candidate in the KTAG. A KTAG candidate with time $\mathrm{T^{KTAG}}$, computed as the average of the times in each fired sector comprising the candidate, is associated to the track if:

- at least 5 out of the 8 KTAG sectors contribute to the candidate (Figure 4.6-top-left);
- $\mathrm{T^{KTAG}}$ is within $\pm$2 ns of T_π (Figure 4.6-top-right).

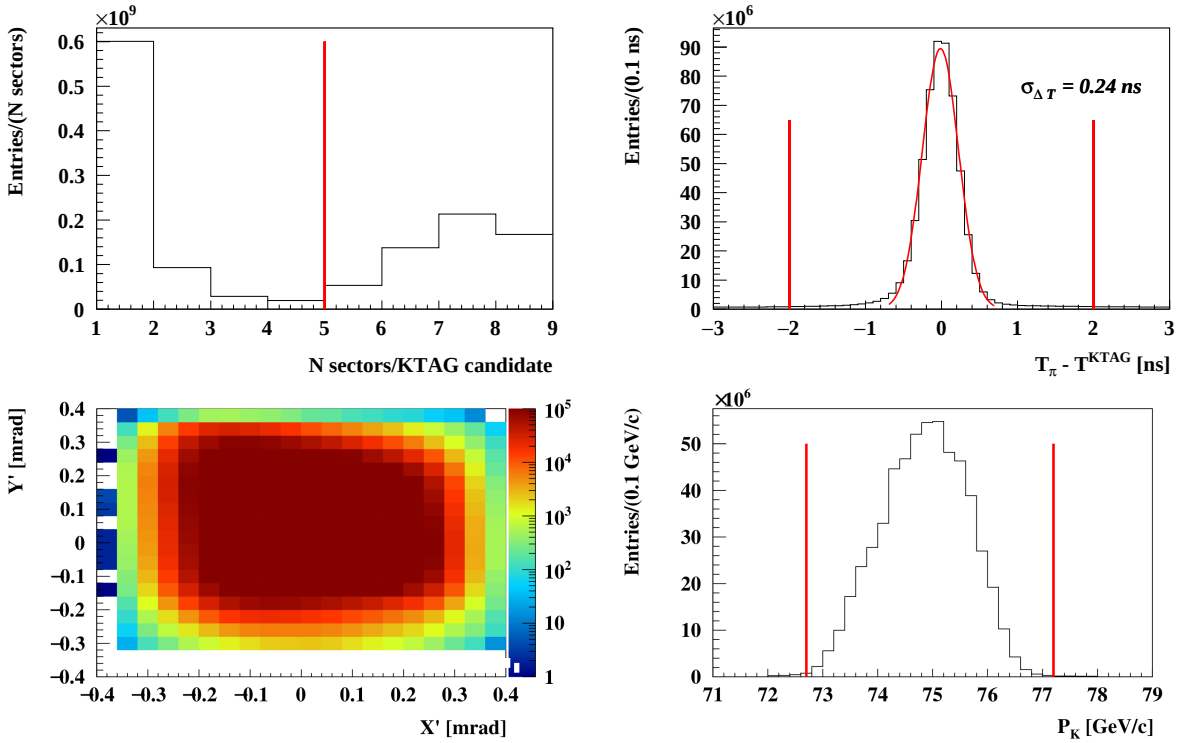

Figure 4.6: *Top left: Distribution of the number of KTAG sectors making a KTAG candidate. The KTAG pressure is optimized to detect the rings from 75 GeV/c kaons. Therefore, a kaon will normally give a signal in at least 5 or 6 KTAG sectors. Tracks with less KTAG sectors fired are due to accidental pions and protons from the beam. Top-right: Distribution of the time difference between the time of the downstream track and the KTAG candidate. Bottom-left: Distributions of the reconstructed slopes of the kaon track X' and Y'. Bottom right: Momentum distribution of the GTK tracks from control-trigger $K_{\pi\pi\pi}$ decays in data.*

If more than one such candidate is found, the candidate with the T^{KTAG} closest to T_π is considered. The KTAG matching efficiency in the $K_{\pi\nu\bar{\nu}}$ MC is 99.8%. The value measured on the $K_{\pi\pi\pi}$ data sample described in Section A.4 is 98%. The difference can be explained due to pileup effects in the KTAG, not simulated in the MC.

Kaon momentum reconstruction

The track reconstruction in the GTK spectrometer is performed at analysis level using T^{KTAG} as the time reference. It is mostly based on the standard reconstruction class `GigaTrackerEvt-Reco`[97].

The schematic layout of the GTK stations and the corresponding achromat is shown in Figure 4.7. The 60 mm y offset generated by the B4 dipoles is recovered after by the B5 and B6 dipoles, so the beam leaves the GTK3 station undeflected in the vertical (y, z) plane (Figure 4.7-left). The TRIM5 dipole gives the final 1.2 mrad horizontal angular deflection before the beam reaches the GTK3 station (Figure 4.7-right).

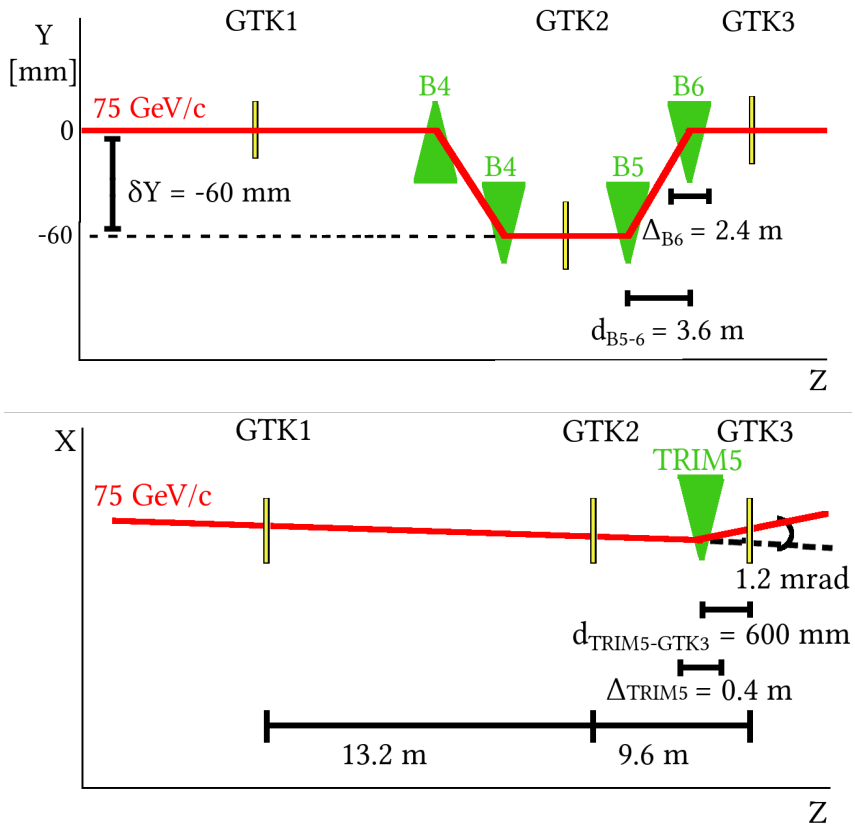

Figure 4.7: *Left: Schematic layout of the Gigatracker stations within the achromat in the vertical view (y, z plane). Right: Same layout in the horizontal view (x, z).*

A GTK track is reconstructed if there are less than 50 hits per station. Only GTK hits within ± 1.2 ns of T^{KTAG} are considered. The x (y) coordinates of the hits in GTK stations 1, 2 and 3 are shifted by -0.341 (-1.842) mm, 2.958 (0.824) mm and 1.775 (0.853) mm to correct for the misalignment of the GTK stations with respect to the reference system. The hits are then combined in triplets with one good hit per GTK station. The track momentum P_K (Figure 4.6-bottom-right) and the dx/dz and dy/dz track slopes X' and Y' (Figure 4.6-bottom-left) are computed for each triplet

$$\begin{aligned} P_K &= \frac{c \cdot B_{B5,6} \cdot \Delta_{B5,6} \cdot d_{B5-6}}{y_1 \cdot (1-\alpha) - y_2 + \delta Y + \alpha \cdot y_3}; \\ X' &= \frac{x_3 - x_1}{z_3 - z_1} + \frac{c \cdot B_{\mathrm{TRIM5}} \cdot \Delta_{\mathrm{TRIM5}}}{P} \left(1 - \frac{d_{\mathrm{TRIM5\text{-}GTK3}}}{z_3 - z_1}\right); \\ Y' &= \frac{y_3 - y_1}{z_3 - z_1}. \end{aligned} \tag{4.10}$$

Here $x_{1,2,3}$ and $y_{1,2,3}$ are the coordinates of the GTK hits in stations 1,2,3, respectively; $z_1 = 79\,600$ mm, $z_2 = 92\,800$ mm and $z_3 = 102\,400$ mm are the longitudinal positions of the GTK stations, $\delta Y = -60$ mm is the offset of GTK2 along y and $\alpha = (z_2 - z_1)/(z_3 - z_1) = 0.579$; $B_{B5,6} = 1.6678$ T/m, $\Delta_{B5,6} = 2500$ mm, $d_{B5-6} = 3600$ mm are the absolute magnetic fields of dipoles B5 and B6, the thicknesses of B5 and B6 and the distances between them, respectively;

$B_{\mathrm{TRIM5}} = 0.7505$ T/m, $\Delta_{\mathrm{TRIM5}} = 400$ mm and $d_{\mathrm{TRIM5\text{-}GTK3}} = 400$ mm are the magnetic field and the thickness of the TRIM5 dipole and its distance from B6, respectively. Track slopes are corrected for residual rotations and misalignments between the GTK and the STRAW.

A set of χ^2 requirements is used to assess the quality of the GTK track: χ^2_{X}, χ^2_{Y}, χ^2_{T}. The χ^2_{X} value is obtained from least squared fit performed to test the consistency of the $x_{1,2,3}$ positions with a straight trajectory, where x_3 is measured after the track has been deflected back by TRIM5. The resolutions on the x hit positions in stations 1,2 and 3 are 86.6, 86.6 and 220 μm. The quantities χ^2_{Y} and χ^2_{T} are defined as

$$\begin{aligned} \chi^2_{\mathrm{Y}} &= \left(\frac{y_2 - y_1}{\sigma_{\Delta y(12)}}\right)^2 + \left(\frac{y_3 - y_2}{\sigma_{\Delta y(23)}}\right)^2; \\ \chi^2_{\mathrm{T}} &= \left(\frac{t_2 - t_1}{\sigma_{\Delta t}}\right)^2 + \left(\frac{t_3 - t_2}{\sigma_{\Delta t}}\right)^2. \end{aligned} \tag{4.11}$$

Here $\sigma_{\Delta y(12)} = 1.42$ mm, and $\sigma_{\Delta y(23)} = 1.20$ mm are the spreads of y_1 and y_3 versus y_2 given the beam momentum bite and $\sigma_{\delta t} = 250$ ps is the resolution of the hit time differences.

A GTK track is defined as *good* if

- the measured GTK momentum P_K is between 72.7 and 77.2 GeV/c;
- the track slope X' is between 0.9 and 1.6 mrad;
- the track slope Y' is between -0.3 and 0.4 mrad;
- the condition $\theta_{\Delta\mathrm{beam}} \leq 0.35$ mrad is used to ensure that the GTK track slopes are consistent with the nominal beam direction

$$\theta_{\Delta\mathrm{beam}} = \sqrt{\left(X'_{\mathrm{K}} - \theta^{\mathrm{TRIM5}}_{\mathrm{X}} - \langle X'_{\mathrm{beam}}\rangle\right)^2 + \left(Y'_{\mathrm{K}} - \langle Y'_{\mathrm{beam}}\rangle\right)^2}. \tag{4.12}$$

  Here $\theta^{\mathrm{TRIM5}}_{\mathrm{X}}$ is deflection angle introduced by the momentum kick along X provided by TRIM5 and $\langle X'_{\mathrm{beam}}\rangle$ and $\langle Y'_{\mathrm{beam}}\rangle$ are the average dx/dz and dy/dz beam slopes before TRIM5;
- $\chi^2_{\mathrm{X}} \leq 20$;
- $\chi^2_{\mathrm{Y}} \leq 20$;
- $\chi^2_{\mathrm{T}} \leq 30$.

Only good GTK tracks are considered for the analysis. The GTK track reconstruction efficiency is 88% (roughly 4% per GTK station) measured on a sample of kinematically selected $K_{\pi\pi\pi}$ decays (Section A.4) in data.

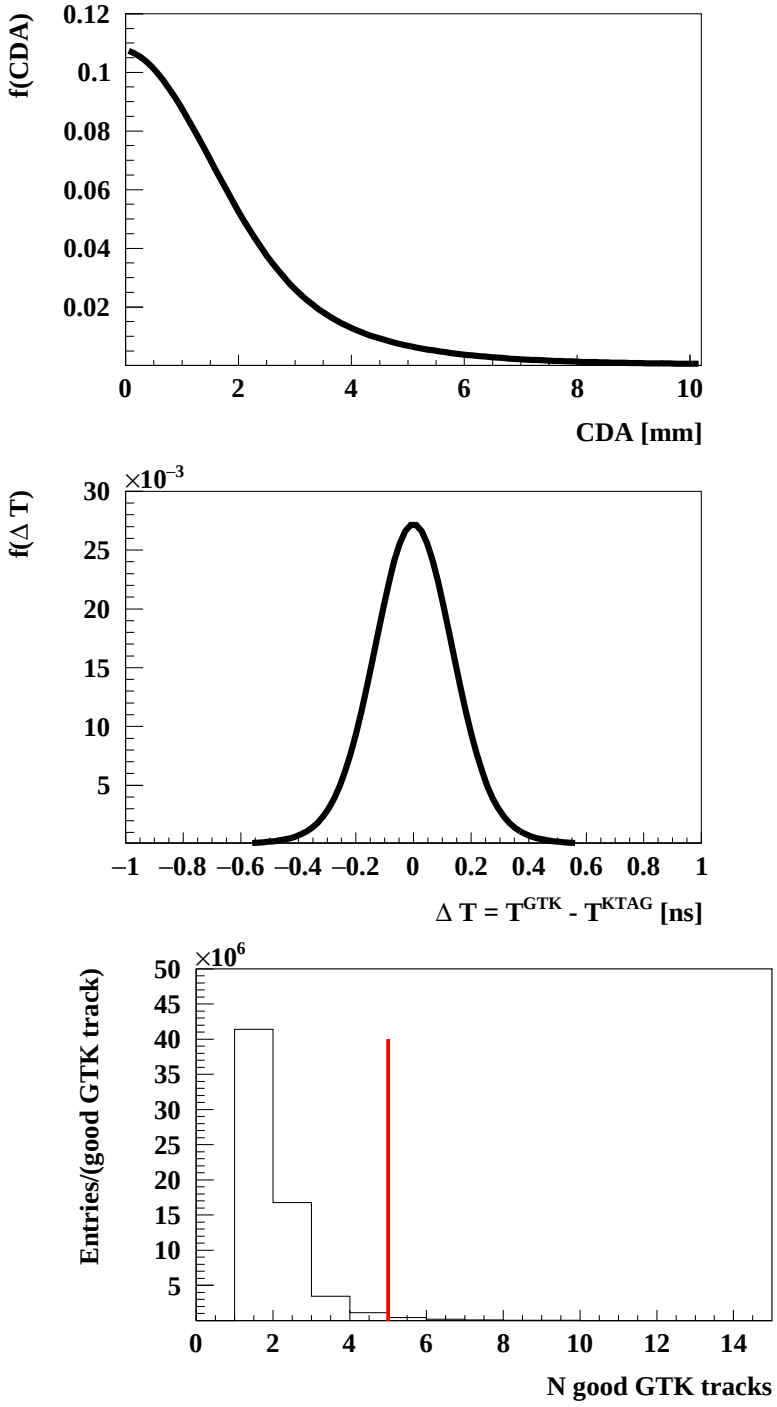

Figure 4.8: *Distributions of p(CDA) (top) and p(*ΔT*) (center), both obtained from control-trigger* $K_{\pi\pi\pi}$ *decays. Distribution of the number of good GTK tracks for one-track events in data (bottom). The red line indicated the cut value.*

4.4 Single-track kaon decay selection

Association of STRAW tracks with the GTK

The decay vertex between the STRAW track and a good GTK track is defined as the position of the median point at the distance of closest approach (CDA) between the two tracks. The CDA and the $\Delta T = T^{GTK} - T^{KTAG}$, where T^{GTK} is the GTK track time are used to form a matching discriminating variable

$$D(CDA, \Delta T) = [1 - p(CDA)] \cdot [1 - p(\Delta T)]. \tag{4.13}$$

Here $p(CDA)$ and $p(\Delta T)$ are the cumulative distribution functions of the CDA and ΔT defined as

$$p(CDA) = \int_0^{CDA} f(CDA')\, dCDA', \tag{4.14}$$

$$p(\Delta T) = \int_0^{|\Delta T|} 2 \cdot f(|\Delta T|')\, d|\Delta T|', \tag{4.15}$$

where $f(CDA)$ and $f(\Delta T)$ are Probability Density Functions (PDFs) for CDA (Figure 4.8-top) and ΔT (Figure 4.8-center), respectively. The PDFs' are template functions derived from the analysis of control-trigger $K^+ \to \pi^+\pi^+\pi^-$ decays[98]. The discriminant represents the probability CDA and ΔT to have larger values than observed.

An additional discriminating variable, $D(CDA, \Delta T_{RICH})$, is computed as above with $\Delta T_{RICH} = T^{GTK} - T^{RICH}$ to reinforce the coincidence between the STRAW and GTK tracks. The same $f(\Delta T)$ PDF (Figure 4.8-center) is used for ΔT_{RICH}.

The good GTK tracks are then sorted by increasing value of $D(CDA, \Delta T)$. The track with the highest $D(CDA, \Delta T)$ value is called the *most probable kaon track* and the others, *associated GTK tracks*. The most probable kaon track matches the STRAW track if:

- the difference between the $D(CDA, \Delta T)$ value obtained for the track and any other associated GTK track is larger than 0.01;
- $D(CDA, \Delta T) > 0.01$ and $CDA < 7$ mm;
- $D(CDA, \Delta T_{RICH}) > 0.005$.

The vertex position and the momenta of the particles corresponding to the STRAW and the associated GTK tracks are corrected for the residual magnetic field in the decay region using the standard correction routine `BlueTubeTracker`[74]. The STRAW - GTK association procedure has 85% efficiency measured on a sample of control-trigger $K^+ \to \pi^+\pi^+\pi^-$ decays (Section A.4) in data. The efficiency agrees with simulation within 5%.

Multi-track topology rejection

Tight cuts are applied to reject events with multiple tracks reconstructed in both the STRAW and GTK detectors:

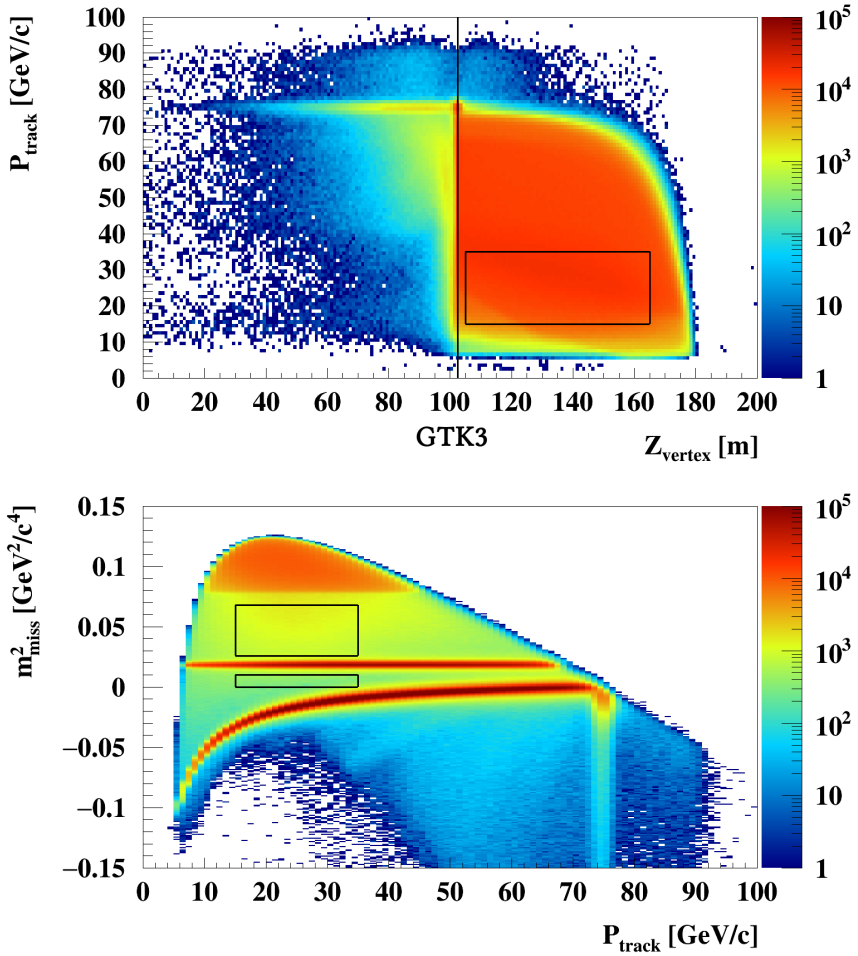

Figure 4.9: *Top: Distribution of the π^+ candidate track momentum versus the z position of the reconstructed kaon decay vertex. The 75 GeV/c component is due to elastic scattering of the beam tracks with the material upstream of GTK3 at 102.4 m (vertical black line). Inelastic beam-GTK3 scattering produces the component at the GTK3 z-position, spanning over the whole momentum range. The signal region is marked with dashed black lines. Bottom: Missing mass squared distribution of all kaon decay events with single-track topology versus the STRAW track momentum. The signal region is marked with dashed black lines. The $K_{\pi\pi}$ decays produce a peak centered at $m^2_{\pi^0} = 0.019$ GeV$^2/c^4$. At missing mass squared above (0.07 GeV$^2/c^4$) the region populated mainly by $K_{\pi\pi\pi}$ decays is distinguished. The band at missing mass squared smaller than 0 is due to $K_{\mu\nu}$ decays. The 75 GeV/c component at negative missing mass squared is produced by the scattered beam pions.*

- a STRAW track must not have more than 4 associated tracks in GTK (Figure 4.8-bottom);
- an event must not have more than 2 tracks reconstructed in the STRAW;
- if 2 STRAW tracks are reconstructed, both must be positive;
- if 2 positive STRAW tracks are selected and both are not fake, their CDA must be greater than 30 mm.

In case of events with two STRAW tracks passing the selection criteria described in the previous sections, the time of the corresponding candidates in CHOD, RICH, LKr, KTAG, GTK and MUV1,2, if any, are compared with the time of the trigger. Events are kept only if the candidate closest in time to the trigger in each of the above detectors matches the same track. This STRAW track is called π^+ *candidate*. The best GTK track associated to the π candidate is called K^+ *candidate*. The missing mass and Z_{vertex} distributions of the single-track kaon decay events are shown in Figure 4.9, both as a function of the π^+ candidate track momentum P_π.

4.5 $K^+ \to \pi^+\nu\overline{\nu}$ selection

Only events passing the single-track kaon decay selection described in the previous section are considered. Additional requirements are applied to the (x, y) coordinates of the reconstructed decay vertex to ensure compatibility with the beam profile

- $X_{\text{vertex}}\,[\text{mm}] \leq -93.9 + 0.0012 \cdot Z_{\text{vertex}}$;
- $X_{\text{vertex}}\,[\text{mm}] \geq -148.53 + 0.00122 \cdot Z_{\text{vertex}}$;
- $Y_{\text{vertex}}\,[\text{mm}] \leq 3.6 + 0.00011 \cdot Z_{\text{vertex}}$;
- $Y_{\text{vertex}}\,[\text{mm}] \geq -5.4 - 0.0001 \cdot Z_{\text{vertex}}$.

The projection in the (x, y) plane at the longitudinal position in the beginning ($Z_{\text{vertex}} = 105$ 000 mm) and the end ($Z_{\text{vertex}} = 165$ 000 mm) of the decay vessel are depicted in Figure 4.10.

4.5.1 Upstream background rejection

Early K^+ decays are responsible for the main component of the upstream background. As the name suggests, those are decays happening before the fiducial decay region and can be wrongly identified as $K_{\pi\nu\overline{\nu}}$ candidates, if an accidental GTK track is associated to the π^+ candidate track.

The following chain of processes illustrates the background mechanism: a $K_{\pi\pi}$ decay happens between the GTK2 and GTK3 stations. The π^0 is absorbed by the C6 collimator (Figure 4.11-top-left), while the π^+ produced within the collimator aperture enters the decay region after deflection by the TRIM5 dipole magnet. A hit is produced in the GTK3 detector by an accidental kaon, forming a fake K^+ track in-time with the π^+ from the decay that can mimic a vertex

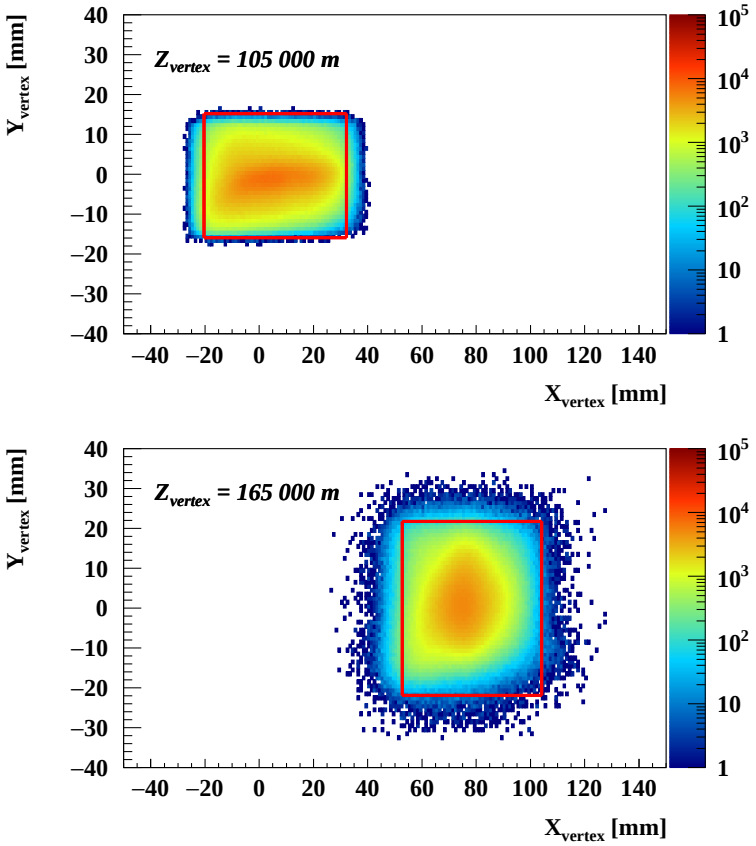

Figure 4.10: *Left: Projection in the (x, y) plane of the decay vertex at $Z_{\text{vertex}} =$ 105 000 mm. The beam profile in the beginning of the decay region is determined by the dimensions of the GTK3 station between -30 and +30* mm *in x and -15 and +15* mm *in y. Right: Same projection, but at the end of the decay region at $Z_{\text{vertex}} =$ 165 000 mm. The z-dependent beam divergence is taken into account in the analysis. The decay vertex must be consistent with the beam profile at a given Z_{vertex} position, marked with thick red box.*

inside the $K_{\pi\nu\overline{\nu}}$ fiducial region. Since the π^0 is absorbed, the downstream detectors see a single π^+ track with significant missing energy and no extra activity in the event.

Similarly, the π^+ track can travel above the collimators and enter the decay region through a hole in the aperture of the dipole magnets (Figure 4.11-top-right). The remaining π^0 is absorbed by the C6 and C7 collimators. The π^+ flies above the GTK3 station and matches a fake K^+ track, forming a vertex inside the fiducial region.

The background depends on the amount of material along the π^+ track and on the residual magnetic field in all beam line elements. A simulation of beam decays and their propagation through the beam line material is extremely difficult. It requires precise knowledge of the material budget along the 23 m long region of the three GTK stations, the mapping of the magnetic fields inside and outside of the beam line elements and a simulation of tens of billions of decays to match the collected data.

However, a toy MC simulation of few million $K_{\pi\pi}$ decays can be used to understand some

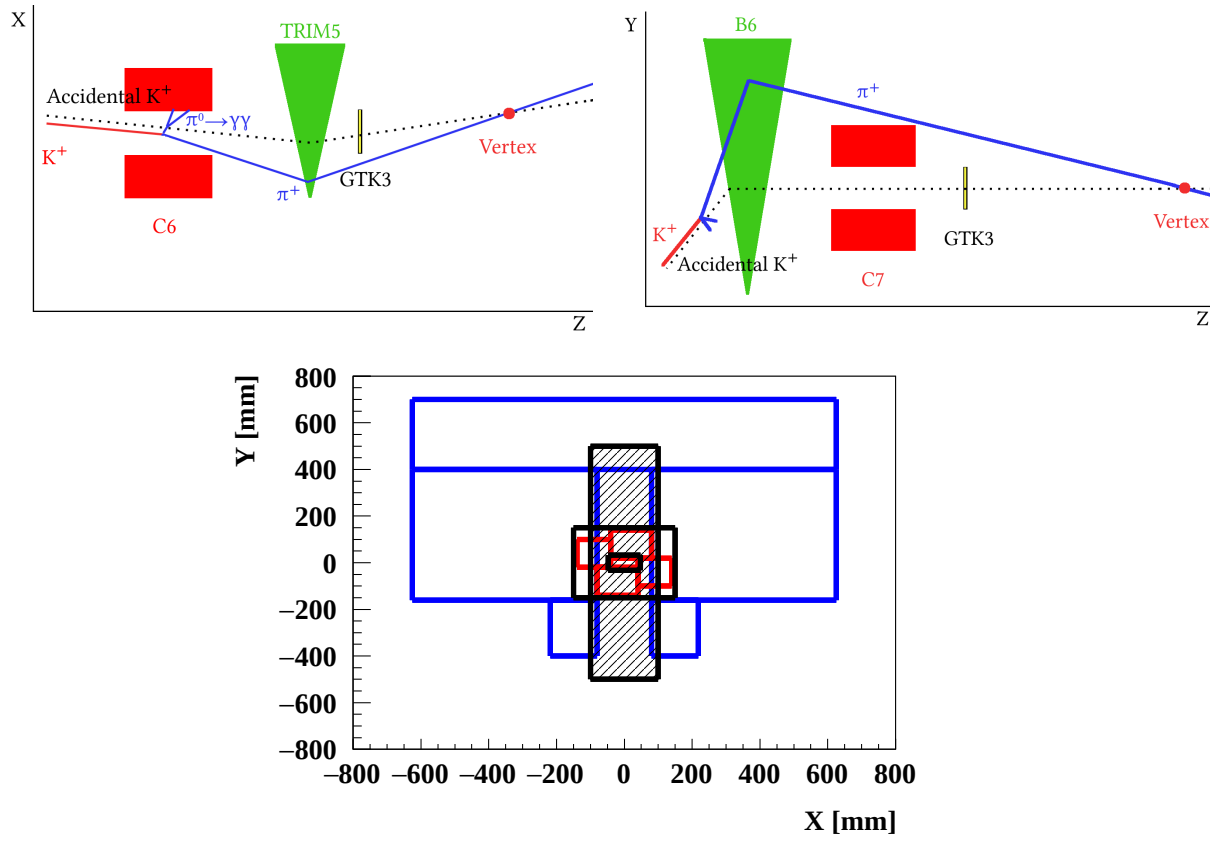

Figure 4.11: *Top: Sketches of $K_{\pi\pi}$ upstream decays in the region before the GTK3 station in the horizontal (left) and the vertical plane (right). For details see text. Bottom: Projection at TRIM5 $z-$position of the upstream beam line elements in the (x, y) plane superimposed with the rectangular cut described in the text. The blue line outlines the envelope of the dipole magnet after GTK2, spanning the region in x from -650 to $+650$* mm *and -160 to $+700$* mm *in y. The black box from -150 to $+150$* mm *in (x, y) corresponds to the projection of CHANTI and the four red boxes represent the four blocks of the final collimator. The applied box cut is shown as a hatched black rectangle in the right plot.*

basic properties of the upstream background decays. The decays are simulated in the region between the GTK2 station and the B5 dipole magnet using two-body phase space simulation of the `TGenPhaseSpace` class in the `ROOT` data analysis framework[99]. The π^+ track produced in the decay is then propagated to the STRAW1 front face, applying the momentum kicks of B5, B6 and TRIM5 dipole magnets. The vertex is defined as the median point of the closest distance of approach between the nominal beam line and the π^+ from the $K_{\pi\pi}$ decay.

The simulation suggests that the background has a geometrical origin and can be suppressed by applying fiducial cuts. The impact position of the π^+ candidate track at the first STRAW chamber can be used, together with the z position of the decay vertex, to improve the upstream background rejection without loosing too much signal acceptance. The comparison between $K_{\pi\nu\bar{\nu}}$ MC and the geometrical simulation is shown in Figure 4.12. Clear differences between the two processes are visible. The shape of the distributions is used to define the fiducial region for the $K_{\pi\nu\bar{\nu}}$ measurement using the distance of the π^+ candidate track from the center of the hole

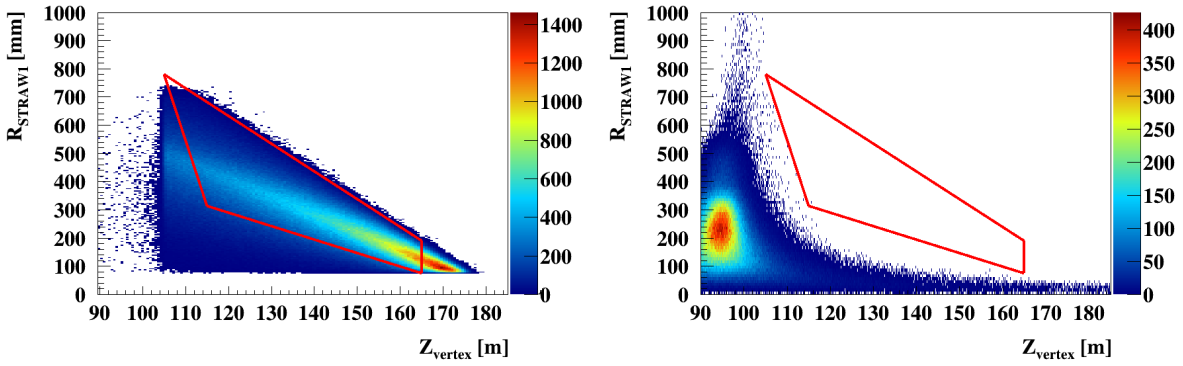

Figure 4.12: *Distribution of the z position of the decay vertex versus the distance between the extrapolated π^+ candidate track at the longitudinal STRAW1 position and the center of the chamber for $K_{\pi\nu\overline{\nu}}$ (left) and simulated $K_{\pi\pi}$ decays between the GTK2 station and the B5 dipole magnet (right). The region marked with thick red line corresponds to the fiducial decay region of the $K_{\pi\nu\overline{\nu}}$ measurement.*

at the STRAW1 front face (the hole has X offset of 101.2 mm)

$$R_{\mathrm{STRAW1}}[\mathrm{mm}] = \sqrt{(X_\pi - 101.2)^2 + Y_\pi^2}, \tag{4.16}$$

where (X_π, Y_π) are the coordinates of the π^+ candidate track at the STRAW1 z-position and the longitudinal position of the decay vertex Z_{vertex}:

- $R_{\mathrm{STRAW1}}\,[\mathrm{mm}] > 735 - 0.004 \cdot Z_{\mathrm{vertex}}$ (bottom border);
- $R_{\mathrm{STRAW1}}\,[\mathrm{mm}] > 7462.5 - 0.0625 \cdot Z_{\mathrm{vertex}}$ (left border);
- $R_{\mathrm{STRAW1}}\,[\mathrm{mm}] < 1812.5 - 0.0098333 \cdot Z_{\mathrm{vertex}}$ (top border);
- $Z_{\mathrm{vertex}}\,[\mathrm{mm}] < 165\,000$ (right border);
- $R_{\mathrm{STRAW1}}\,[\mathrm{mm}] > 0.00436 \cdot Z_{\mathrm{vertex}} + 830$.

Geometrical cuts are applied to exclude possible gaps in the upstream beam line elements. The aperture of the dipoles that bring the beam back on axis after GTK2 allow upstream decays to sneak in the decay region. The corresponding (x, y) projection at the TRIM5 dipole magnet longitudinal position is shown in Figure 4.11-bottom. Events are rejected if the π^+ candidate track extrapolated back to TRIM5 falls within a box defined by $|X_{\mathrm{TRIM5}}| < 100$ mm and $|Y_{\mathrm{TRIM5}}| < 500$ mm, where $(X_{\mathrm{TRIM5}}, Y_{\mathrm{TRIM5}})$ are the (x, y) coordinates of the π^+ candidate track at the TRIM5 z-position.

A beam particle can also interact inelastically with the material of the upstream detectors, in particular in the third station of the GTK. Usually such interactions are followed by extra activity in the CHANTI and can be rejected applying the following criteria

- no CHANTI candidate associated to the π^+ candidate track (a CHANTI candidate is defined as at least one X-Y CHANTI coincidence within ± 3 ns from T_π);

– no associated track in the GTK detector, additional to the K^+ candidate forming a vertex with the π^+ candidate in the range $100 < Z_{\rm vertex} < 105$ m.

The acceptance loss due to the upstream background rejection procedure is estimated using $K_{\pi\nu\overline{\nu}}$ MC. A 30% relative loss comes from the geometrical cut on ($X_{\rm TRIM5}$, $Y_{\rm TRIM5}$) and 10% drop from the fiducial region definition and the cut against CHANTI activity. An additional random veto of 2% is caused by the CHANTI cuts, measured on $K_{\mu\nu}$ decays in data.

4.5.2 Charged pion identification with calorimeters

The algorithm for π^+ identification in the calorimeters has been developed to provide a μ^+ rejection of at least five orders of magnitude, needed to suppress $K_{\mu\nu(\gamma)}$ decays and muons from other sources. Tracks recognized as minimum ionizing particles are rejected using the information from LKr, MUV1, MUV2 and MUV3.

A track is considered to be a μ^+ if it fulfills one of the following requirements:

– a MUV3 hit matches the π^+ candidate track with $-10 < {\rm T}_{\rm hit}^{\rm MUV3} - {\rm T}_{\pi}^{\rm CHOD} < 5$ ns;

– $\rm D_{MIP} < 1$ (Section 4.2);

– the muon probability provided by the MVA algorithm (Section 4.2) is greater 0.01;

– the pion probability provided by the MVA algorithm is lower than 0.96.

Events with the track identified as a μ^+ are rejected.

The residual muons are those undergoing catastrophic bremsstrahlung and is absorbed in the LKr. The LKr shower shapes are used to identify electromagnetic-like showers, which differ from the hadron showers by their size and the energy distribution within the shower.

The two quantities used to reject electromagnetic-like LKr showers are:

$$R_{\rm seed} = \frac{E_{\rm seed}}{E_{\rm cluster}},\ R_{\rm cell} = \frac{N_{\rm cells}}{E_{\rm cluster}}, \tag{4.17}$$

where $E_{\rm seed}$ is energy of the most energetic cell of the cluster, $E_{\rm cluster}$ is the energy of cluster associated to the π^+ candidate track; $N_{\rm cells}$ is the number of cells forming the cluster associated to the π^+ candidate track. The distributions of $R_{\rm seed}$ and $R_{\rm cell}$ for positrons (Figure 4.13-right) and pions (Figure 4.13-left) are compared.

At least one of the following criteria identifies an electromagnetic-like LKr shower:

– $R_{\rm seed} > 0.35$;

– $R_{\rm seed} < 0.05$;

– $R_{\rm seed} > 0.2$ and $R_{\rm cell} \leq 3$ GeV^{-1};

– $R_{\rm seed} \leq 0.2$ and $R_{\rm cell} < 1.8$ GeV^{-1}.

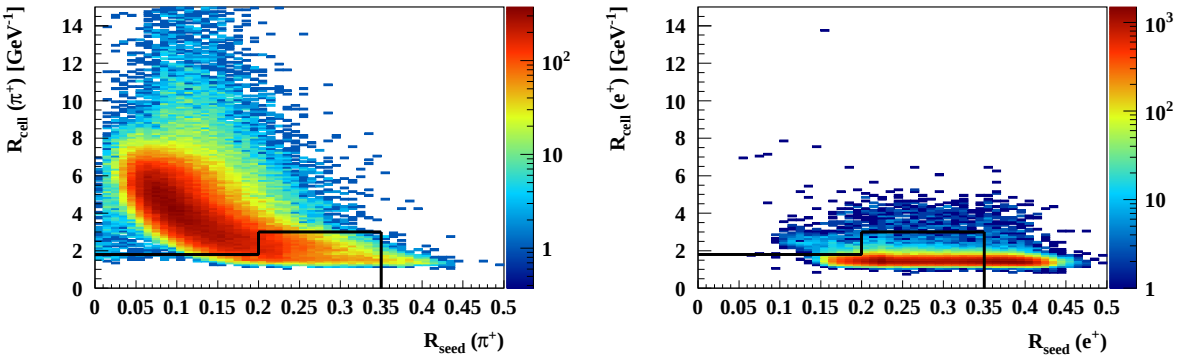

Figure 4.13: *Distributions of the ratios $R_{\rm cell}$ vs $R_{\rm seed}$ for control-trigger pions (left) and positrons (right). The samples are selected by the $K^{calo}_{\pi\pi}$ and K_{e3} selections detailed in Sections A.1 and A.3,respectively. The hadron showers produced by the pions are broad with the energy shared equally among the central cells of the shower, corresponding to a high $R_{\rm cell}$ and small $R_{\rm seed}$. Electromagnetic showers are typically narrow and a big fraction of the energy is released close to the shower starting point.*

Electromagnetic-like clusters are rejected only if no energy is found in the MUV1 or MUV2 detectors. Additionally, the ratio $E_{\rm LKr}/P_\pi$ must be below 0.8, to reject positrons.

No extra calorimeter energy not associated with the cluster of the π^+ candidate track is allowed in the event. Presence of extra energy is detected if at least one of the conditions below is fulfilled:

- more than 5 GeV extra energy in MUV1 and MUV2 together;
- total calorimetric energy lower than $0.15 \cdot P_\pi - 1.5$;
- total calorimetric energy greater than $1.2 \cdot P_\pi$.

The π^+ identification efficiency of the algorithm presented in this section is 80%, measured on $K_{\pi\nu\overline{\nu}}$ MC, which agrees within 2% with the value obtained in data (Section5.1).

4.5.3 Charged pion identification with the RICH

The criteria of particle identification with the RICH counter are applied to a π^+ candidate track with $15 < P_\pi < 35$ GeV/c. A π^+ is identified with the likelihood-based algorithm (Section 4.2) if:

$$\frac{\mathcal{L}(\pi^+)}{\max\left(\mathcal{L}(\mu^+), \mathcal{L}(e^+)\right)} > 1.2, \tag{4.18}$$

where $\mathcal{L}(\textit{particle type})$ is the likelihood for the ring under a particle mass hypothesis provided by the algorithm.

The particle mass is computed from the ring radius given by the standalone RICH algorithm (Section 4.2)

$$M_{\rm RICH} = P_\pi \cdot n_{\rm Ne} \cdot \sqrt{\cos^2\left(\tan^{-1}\left(\frac{R_{\rm ring}}{f_{\rm length}}\right)\right) - 1}. \tag{4.19}$$

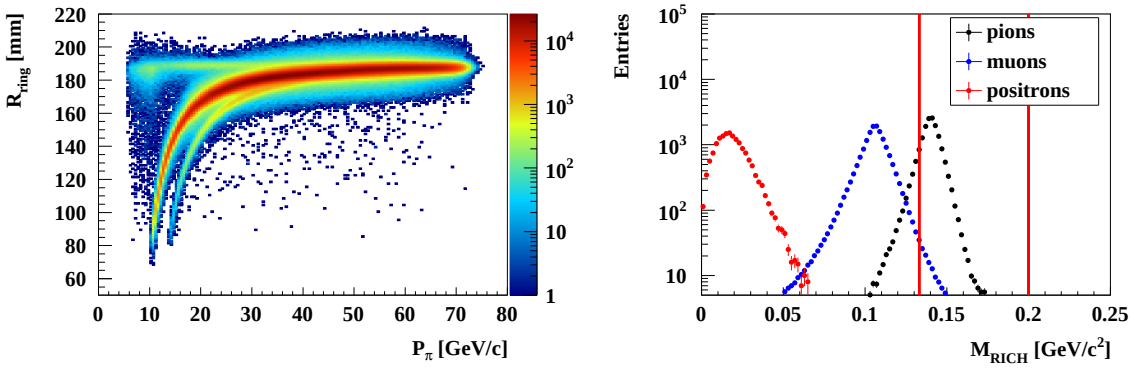

Figure 4.14: *Left: Distribution of the RICH ring radius versus the momentum of the π^+ candidate track. The differences between electrons, pions and muons are clearly visible. Right: Distribution of M_{RICH}, computed with 4.19 for pions (black), muons (blue) and positrons (red) using the $K^{RICH}_{\pi\pi}$, $K^{RICH}_{\mu\nu}$ and K_{e3} samples in data. The samples are described in Sections A.1, A.2 and A.3 of the appendix. The cuts are indicated with red lines.*

Here R_{ring} is the ring radius (Figure 4.14-left), $f_{\mathrm{length}} = 17020$ mm is the focal length of the mirrors and n_{Ne} the refractive index of the neon gas computed from the Cherenkov angle of electrons as

$$n_{\mathrm{Ne}} = \frac{1}{\cos\left(\tan^{-1}\left(\frac{R_{\mathrm{electron}}}{f_{\mathrm{length}}}\right)\right)}, \tag{4.20}$$

with R_{electron} the ring radius for $\beta = 1$ particles as provided by a standard database on a burst-by-burst basis. The particle is considered to be a pion if M_{RICH} is between 133 and 200 MeV/c^2 (Figure 4.14-right). The RICH particle identification algorithm has an efficiency of 87% for π^+, obtained from $K_{\pi\nu\bar{\nu}}$ MC, consistent within 5% with the value obtained from data (Section 5.2).

The RICH counter can also measure the π^+ candidate track momentum, P_π^{RICH}, assuming charged pion mass m_{π^+}:

$$P_\pi^{\mathrm{RICH}} = m_{\pi^+} \cdot \frac{f_{\mathrm{length}}}{\sqrt{R^2_{\mathrm{electron}} - R^2_{\mathrm{ring}}}}. \tag{4.21}$$

The momentum P_π^{RICH} will be is used for signal region definition (Section 4.5.6).

4.5.4 Photon rejection

A positively identified π^+ track must not have any additional in-time activity in the downstream detectors. Therefore a cluster-based rejection of extra activity is applied in the LKr, LAV, SAC and IRC detectors.

Extra clusters of energy deposition are reconstructed using the standard LKr cluster algorithm (Section 4.2). The clusters are considered if they are at least 100 mm away from the extrapolated pion track position at the LKr front face and are defined in the two dimen-

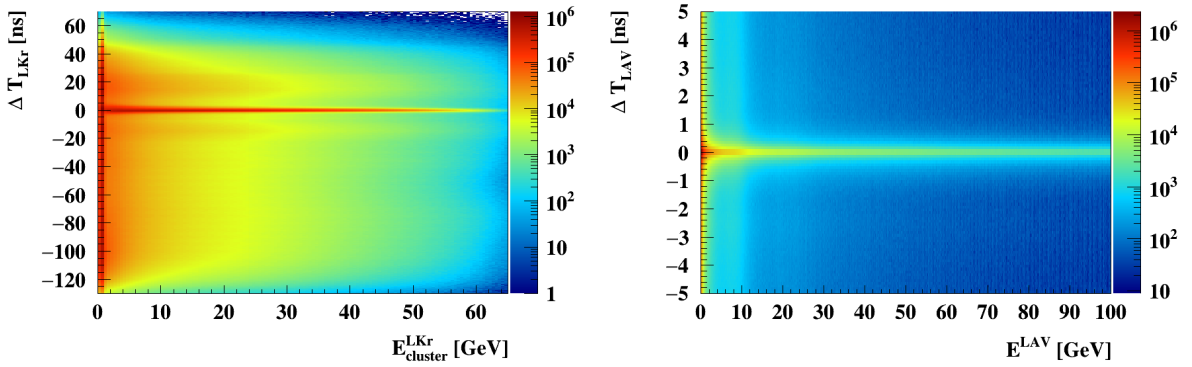

Figure 4.15: *Left: Distribution of the LKr clusters not belonging to the π candidate. On the x axis the cluster energy is shown. The y axis corresponds to the time difference between the cluster and the CHOD time of the π candidate. Right: Distribution of the total energy deposit in the LAV station closest in time to T_π versus the corresponding time difference.*

sional (E_{cluster}, ΔT_{LKr}) plane shown in Figure 4.15-left, where $E^{\text{LKr}}_{\text{cluster}}$ is the cluster energy and $\Delta T_{\text{LKr}} = T_{\text{CHOD}} - T^{\text{LKr}}_{\text{cluster}}$ is the time difference between the cluster and the CHOD time of the π^+ track.

The gaussian part of the in-time activity centered at $\Delta T_{\text{LKr}} = 0$ is removed using the typical time resolution of an electromagnetic LKr cluster $\sigma_{T_{\text{LKr}}}(\text{ns}) = 0.56 + 1.53/E_{\text{cluster}}[\text{GeV}] - 0.233/\sqrt{E_{\text{cluster}}[\text{GeV}]}$. However, wide time windows of up $\pm 70\,\sigma_{T_{\text{LKr}}}$ are necessary to reject non-gaussian tails induced by cluster time mis-reconstruction. Significant time offsets can be generated if the clusters are reconstructed using hits originating from the same shower, but with time wrongly assigned to a neighbouring readout time slot. Such hits will typically have offsets of at least 25 ns due to the 400 MHz sampling rate of the readout modules.

If no cluster are reconstructed with the standard reconstruction, an "auxiliary reconstruction algorithm" is used to ensure the highest possible LKr rejection. Energy depositions of at least 40 MeV are clustered geometrically in nearby cells. Two cells are considered nearby if separated by less than 100 mm. The same energy and time corrections as in the standard reconstructions are applied to the auxiliary clusters.

The cuts against in-time activity apply to the clusters reconstructed with either the standard or the auxiliary reconstruction. The cut for energies below 1 GeV is applied only if the clusters are reconstructed with the standard algorithm. The complete set of photon rejection conditions are presented in Table 4.2.

The standard LAV veto tool `LAVMatching`[74] is used to reject activity in any of the LAV stations. Any hit block in any of the LAV stations selected by the tool is considered to be a photon in time with the π^+ track if within ± 3 ns of T_π (Figure 4.15-right).

Hits selected by the standard IRC and SAC veto algorithm `SAVMatching`[74] are in time with the pion if they are within ± 7 ns of T_π. The tool uses the TDC readout of IRC and SAC. In case no signal is found, hits are considered in time if any of the conditions in Table 4.3 are met.

Finally, the FADC readout of IRC and SAC is exploited to reject residual photons not

Cluster energy range	Time cut
$E < 1$ GeV	$\lvert\Delta T_{LKr}\rvert < 5$ ns
$1 \le E < 2$ GeV	$\lvert\Delta T_{LKr}\rvert < 5 \cdot \sigma_{T\ LKr}$
$2 \le E < 15$ GeV	$\lvert\Delta T_{LKr}\rvert < 15 \cdot \sigma_{T\ LKr}$
$E \ge 15$ GeV	$\lvert\Delta T_{LKr}\rvert < 70 \cdot \sigma_{T\ LKr}$
$E > 10$ GeV	$\lvert\Delta T_{LKr} \pm 25\text{ ns}\rvert < 3 \cdot \sigma_{T\ LKr}$
$E > 2$ GeV $0 < X_{\text{cluster}} < 600$ mm $\lvert Y_{\text{cluster}}\rvert < 300$ mm	$\lvert\Delta T_{LKr} + 36\text{ ns}\rvert < 3$

Table 4.2: *Photon veto conditions in the LKr. The cut 25 ns away is to protect against clusters reconstructed in the neighbouring readout time slot. The final cut 36 ns away is related to a problematic readout module that was producing signals with a 36 ns offset during parts of the 2016 data taking. The* $T(X_{\text{cluster}}, Y_{\text{cluster}})$ *cuts indicate the specific regions of the LKr covered by that readout board.*

ToT range	Time cut [ns]
$ToT < 2$	$\lvert T_{IRC} - T_\pi\rvert < 7$ $\lvert(T_{IRC} - 7) - T_\pi\rvert < 7$ $-7 < T_{SAC} - T_\pi < 10$
$2 \le ToT < 25$	$\lvert T_{IRC\,(SAC)} - T_\pi\rvert < 7$ $\lvert T_{SAC} - T_\pi\rvert < -8.3524 + 0.2105 \cdot ToT$
$ToT \ge 25$	$\lvert T_{IRC\,(SAC)} - T_\pi\rvert < 7$

Table 4.3: *Photon veto conditions in IRC and SAC. The time* T_{IRC} *and* T_{SAC} *is the IRC and SAC hit time and* ToT *is the time over threshold measured by the TDC readout.*

detected by the TDC readout. Signals are considered in time if the energy in IRC and SAC is greater than 1 GeV and their time is within ± 7 ns of T_π.

The photon rejection procedure has an efficiency of 96% for π^+ tracks. The inefficiency is caused by hadronic interactions of the track with the RICH mirrors and delta rays emission followed by an e^+e^- pair conversion and is measured on $K_{\pi\nu\bar{\nu}}$ MC. The additional random veto induced by accidental activity in the detectors is 16.4% (Section 6.5) measured on $K_{\mu\nu}$ decays in data.

4.5.5 Charged multiplicity rejection

A set of background rejection cuts are needed to suppress kaon decays with extra charged particles in the final state, which are not reconstructed in the straw spectrometer or with photons interacting in the material before reaching the LKr.

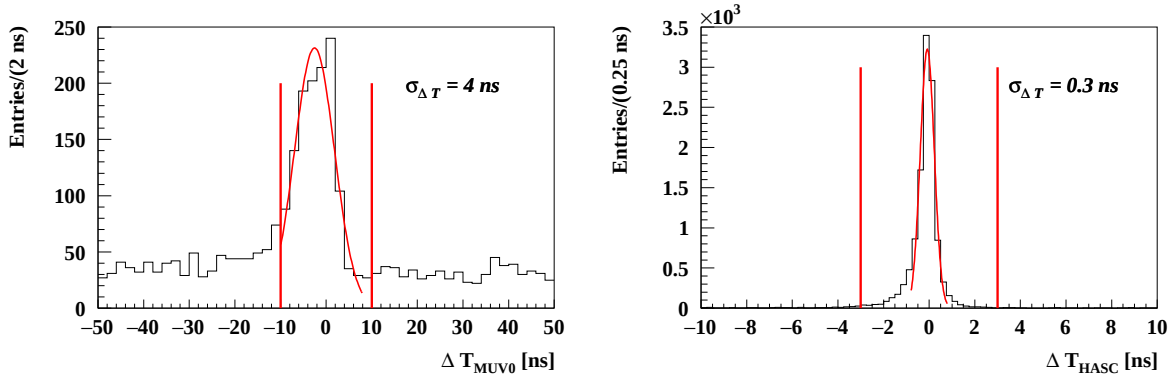

Figure 4.16: *Left: Distribution of the time difference between the MUV0 hit time and* T_π*. No slewing corrections are applied to the MUV0 hit time. Right: Distribution of the time difference between the HASC hit time and* T_π*. No slewing corrections are applied to the HASC hit time.*

No hits are allowed in the HASC within ±3 ns from T_π. A background hit in the HASC is produced by $K_{\pi\pi\pi}$ decays with one of the π^+s flying inside the beam pipe. The pion is deflected by the dipole magnet after MUV3 and produces a hadronic shower in the HASC. Similarly, if a π^0 photon of very high energy converts in the beam pipe close to MUV3, creating a electron-positron pair, the positron will be deflected into the HASC.

No hit are allowed in MUV0 within ±10 ns from T_π. A background in MUV0 is produced by $K_{\pi\pi\pi}$ decays with the π^- further decaying to a muon and an anti-neutrino before the RICH entrance window. The time distributions of the MUV0 and HASC detectors are shown in Figure 4.16.

The final steps for rejecting background with multiple charged particles are:

– hit multiplicity rejection combining in-time activity in LKr, CHOD and NA62CHOD;

– STRAW multiplicity rejection based on reconstruction of STRAW segments not belonging to the track.

These two procedures are described in the following.

The complete charged multiplicity rejection procedure leads to a 12% acceptance loss due to hadronic showers and delta rays in the material upstream of the CHOD counter, measured using $K_{\pi\nu\bar{\nu}}$ MC. An additional 6% loss is due to random veto measured on data and described in details in Section 6.5.

Hit multiplicity rejection

All extra hits in time with T_π are collected in the LKr and the two hodoscopes. Events with more than 5 hit CHOD strips within ±7 ns from T_π are rejected. Cells at coordinates $(X_{\text{cell}}, Y_{\text{cell}})$, with energy E_{cell} deposited at time T_{cell} produce extra activity in the LKr if:

– $E_{\text{cell}} > 0.05$ GeV;

- $|T_\pi - T_{cell}| < 4$ ns for $E_{cell} < 0.3$ GeV;
- $-7 < T_\pi - T_{cell} < 10$ ns for $0.3 \leq E_{cell} < 2$ GeV;
- $|T_\pi - T_{cell}| < 10$ ns for $E_{cell} \geq 2$ GeV;
- the distance between the cell position and the pion position at the LKr front face must be > 100 mm.

NA62CHOD hit blocks at coordinates (X_{NA62CHOD}, Y_{NA62CHOD}) detected at time T_{NA62CHOD} are considered in time if they are within ± 5 ns of T_π. The block hit by the pion track is excluded from the counting.

Pairs of horizontal and vertical CHOD strips are associated to extra activity in LKr and NA62CHOD using a procedure similar to the one described in Section 4.2, but using the position of the extra in-time hits as a reference instead of the spectrometer track position at CHOD. A CHOD strip pair is matched to extra LKr activity if

- within ± 15 ns of T_{cell};
- not more than 130 mm away from the extra hit position.

A CHOD strip pair is matched to NA62CHOD in-time hit if

- within ± 15 ns of T_{NA62CHOD};
- within a rectangle defined by ± 250 mm in x and ± 140 mm in y, which covers approximately two time the standard size of a NA62CHOD block.

If both strips are also hit by the track, the pair is discarded.
The NA62CHOD in-time hit blocks are associated to LKr extra activity if

- within a rectangle defined by ± 250 mm in x and ± 140 mm in y.

If an association is found between the extra activity in any pair of detectors the event is rejected.

Extra segments

Straw segments not belonging to the reconstructed tracks are built according to the following procedure: chamber-hits not belonging to the pion track are reconstructed; then segments are reconstructed using vertex and chamber-hits in chambers 1 and 2 or vertex and chamber-hits in chambers 3 and 4.

The hits are sorted per plane and only those with a drift time between 0 and 170 ns are kept. Then clusters of 2 and 3 hits belonging to different view-planes are formed in each view. The same pattern recognition algorithm is applied as in the standard spectrometer reconstruction. A measurement of the coordinate of a track passing through a straw in the local reference system of

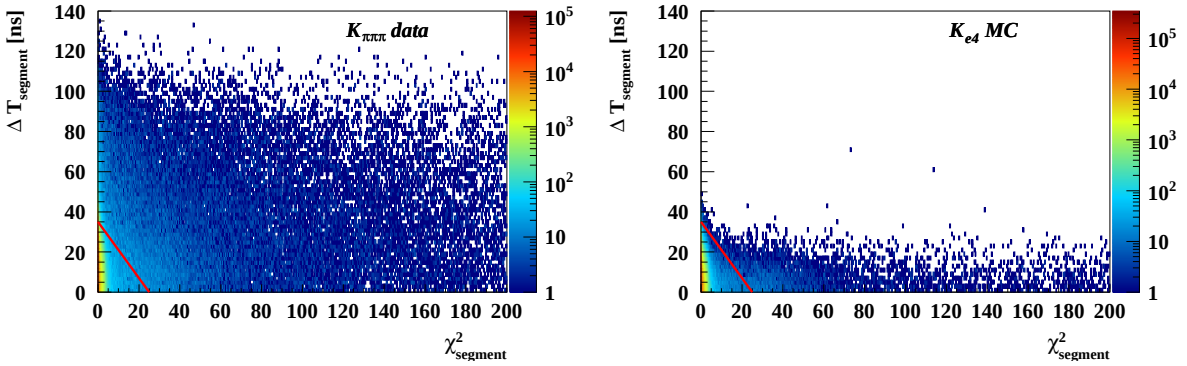

Figure 4.17: *Distributions of the time difference $\Delta T_{segment}$ versus the χ^2_{events}(segment12) for data $K_{\pi\pi\pi}$ decays with two tagged π^+s (left) and MC simulated K_{e4} decays (right). Events below the thick red line have a reconstructed segment.*

the view is provided, exploiting the staggering of the planes of the clustered straws to solve the left-right ambiguity. The unpaired hits are also saved as 1-hit view-clusters, with the position of the straw used as coordinate of the track passing through. Finally, the view-clusters are combined together to form 2-3-4-view chamber-hits adapting the standard pattern recognition to the additional presence of 1-hit view-clusters by broadening the condition on the cluster trailing time to ±200 ns instead of ±100 ns. Furthermore, the quality of the straw intersections is softened to increase reconstruction efficiency.

After the sorting of the non-associated hits, least squared fits in the xz and yz planes are performed on each triplet formed by two chamber-hits in chamber 1 and 2 and the vertex. A triplet is accepted if:

- the fitted slopes are lower than 20 mrad in both projections;
- the fitted segments are at least 30 mm away from the pion position at chamber 1 and 2;

The triplet with the minimum χ^2 defines a segment in chamber 1-2 (*segment12*). The same procedure is applied to chamber-hits in chambers 3 and 4 and the vertex (*segment34*), with two differences:

- the fit and the condition on the slope are not applied in the xz plane;
- the direction of the segment must be compatible with a negative particle with momentum not greater than 90 GeV/c or with a positive particle with momentum lower than 10 GeV/c.

An event has an extra segment in the spectrometer if:

- *segment12*: $|\Delta T_{\text{segment}}| < 35 - 1.4 \cdot \chi^2_{\text{segment}}$;
- *segment34*: $|\Delta T_{\text{segment}}| < 40 - 5.7 \cdot \chi^2_{\text{segment}}$.

Region	m^2_{miss}	$m^2_{\text{miss, beam}}$	$m^2_{\text{miss, RICH}}$
R1 $P < 25$ GeV	$(0, 0.01)$	$(-0.005, 0.0135)$	$(0, 0.02)$
R1 $P \geq 25$ GeV	$(0, 0.01)$	$(0, 0.0135)$	$(-0.005, 0.02)$
R2	$(0.026, 0.068)$	$(0.024, 0.068)$	$(0.02, 0.07)$
CR1($\pi\pi$)	$(0.01, 0.015)$		
CR2($\pi\pi$)	$(0.021, 0.026)$		
CR($\mu\nu$)	$(m^2_{\mu-kin.} + 3\sigma, 0)$		
CR(3π)	$(0.068, 0.071)$		
$\pi\pi$	$(0.015, 0.021)$		$(0, 0.07)$
$\mu\nu$	$(-0.05, m^2_{\mu-kin.} + 3\sigma)$		
$\pi\pi\pi$	$(0.071, maximum)$		

Table 4.4: *Definition of signal regions (R1, R2), control regions (CR) for $K_{\pi\pi}$, $K_{\mu\nu}$ and $K_{\pi\pi\pi}$, background regions for $K_{\pi\pi}$ ($\pi\pi$ region), $K_{\mu\nu}$ ($\mu\nu$ region) and $K_{\pi\pi\pi}$ ($\pi\pi\pi$ region). All m^2_{miss} values are quoted in* GeV^2/c^4.

Here $\Delta\text{T}_{\text{segment}}$ is the difference between T_{GTK} and the average of the trailing time of the two chamber-hits and χ^2_{segment} the value of the χ^2 of the corresponding triplet. Events with reconstructed segments are rejected.

The performance of the algorithm is validated on data using $K_{\pi\pi\pi}$ decays from control triggers reconstructed with two tagged π^+s. The same selection is applied to K_{e4} MC and the comparison is presented in Figure 4.17.

4.5.6 Kinematic selection

The events surviving the $K_{\pi\nu\overline{\nu}}$ selection described in this chapter are show in Figure 4.18. The final selection step is the choice of the kinematic region. Only events with pions in the (15, 35) GeV/c momentum range are considered. Let p_π be the 4-momentum of the pion measured by the spectrometer; $p_{\pi,\,\text{RICH}}$ the 4-momentum of the pion with the pion momentum measured by the RICH instead of the spectrometer; p_K the 4-momentum of the kaon measured by the GTK spectrometer; p_{beam} the nominal beam 4-momentum. The following squared invariant masses are then defined:

$$\begin{aligned} m^2_{\text{miss}} &= (p_K - p_\pi)^2 \\ m^2_{\text{miss, beam}} &= (p_{\text{beam}} - p_\pi)^2 \\ m^2_{\text{miss, RICH}} &= \left(p_K - p_{\pi,\,\text{RICH}}\right)^2 . \end{aligned}$$

Using those three m^2_{miss} definitions the signal, control and background regions are defined in

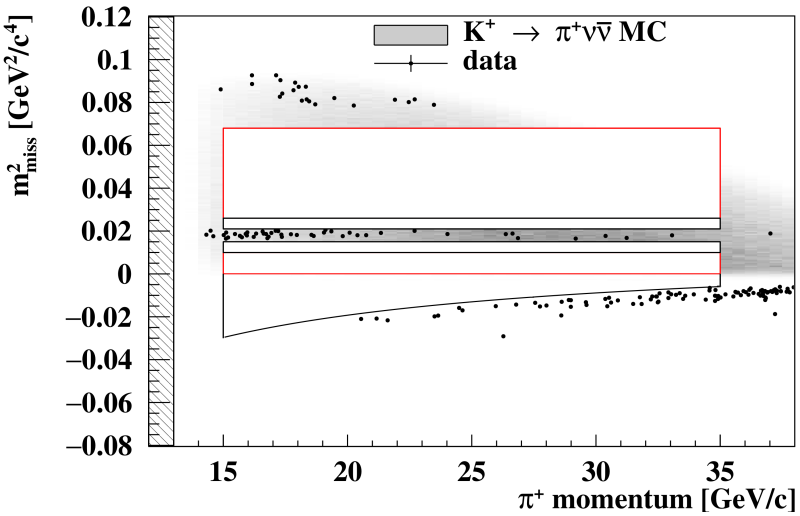

Figure 4.18: *Left: m^2_{miss} as a function of P_π for PNN-trigger data events (dots) passing the $K_{\pi\nu\overline{\nu}}$ selection, but the cuts on m^2_{miss} and P_π. The gray area corresponds to the distribution of $K_{\pi\nu\overline{\nu}}$ MC events, with darker (lighter) grey indicating more (less) populated regions. Red (black) lines define the signal (control) regions and are masked.*

Table 4.4. The $K_{\mu\nu}$ kinematic boundary is

$$m^2_{\mu-\mathrm{kin}} = \left(m^2_{\pi^+} - m^2_{\mu^+}\right)\left(1 - \frac{75}{P_\pi}\right)$$

and its resolution $\sigma = 1.2 \cdot 10^{-3}$ GeV$^2/c^4$ is the gaussian rms obtained using $K_{\mu\nu}$ MC, which is constant over the $15 - 35$ GeV/c momentum range.

The control regions are chosen away from the peaking regions of the background to contain only the non-gaussian components of the kinematic resolution. Events in control regions are used to validate the number of expected background events. The control regions are kept masked in the analysis until the background assessments are finalized.

Events in the signal regions R1 and R2 are the $K_{\pi\nu\overline{\nu}}$ candidates. The signal regions are kept masked until the analysis procedure is completed.

5 Background estimation

After completing the selection the background contamination in R1 and R2 is evaluated using the events in the background regions multiplied by extrapolating factors measured on data. The number of surviving events in the background regions (Figure 4.18) are dependent on the performances of the particle identification algorithms (Sections 4.5.2 and 4.5.3) and neutral pion rejection (Sections 4.5.4 and 4.5.5). Even though those performances are not directly used in the background computation their assessment is very important to control the background contamination in the data sample.

The π^+/μ^+ separation provided by the particle identification procedure is shown in Sections 5.1 and 5.2. Neutral pion rejection is detailed in Section 5.3. Background estimation for all processes contributing to the $K_{\pi\nu\bar{\nu}}$ background is explained in Sections 5.4-5.11. The background is summarized in Section 5.12.

5.1 Particle identification with calorimeters

Two samples of π^+ and μ^+ tracks are considered to evaluate the performance of the particle identification algorithm: $K^{\rm calo}_{\pi\pi}$ and $K^{\rm calo}_{\mu\nu}$, described in Sections A.1 and A.2. Both closely follow the normalization selection with the only difference that calorimetric particle identification is not applied and kinematic cuts are added to suppress background.

The π^+/μ^+ separation is shown in Figure 5.1-left. The average π^+ efficiency in the (15, 35) GeV/c momentum range is $\epsilon^{\pi}_{\rm calo} = (77.5 \pm 0.1_{stat})\%$, corresponding to a μ^+ rejection of $\epsilon^{\mu}_{\rm calo} = (6.4 \pm 0.5) \times 10^{-6}$.

The achieved π^+/μ^+ separation is better than the required value of 10^{-5} for the $K_{\pi\nu\bar{\nu}}$ analysis[87]. The stronger suppression is needed to compensate the slightly larger tails due to kinematic $K_{\mu\nu}$ misreconstruction. The efficiency curves are obtained using the full 2016 dataset.

The MC simulation reproduces these results within 3%. The difference is due to trigger-induced MUV3 random veto, because the 20 ns trigger veto window in 2016 was wider than the

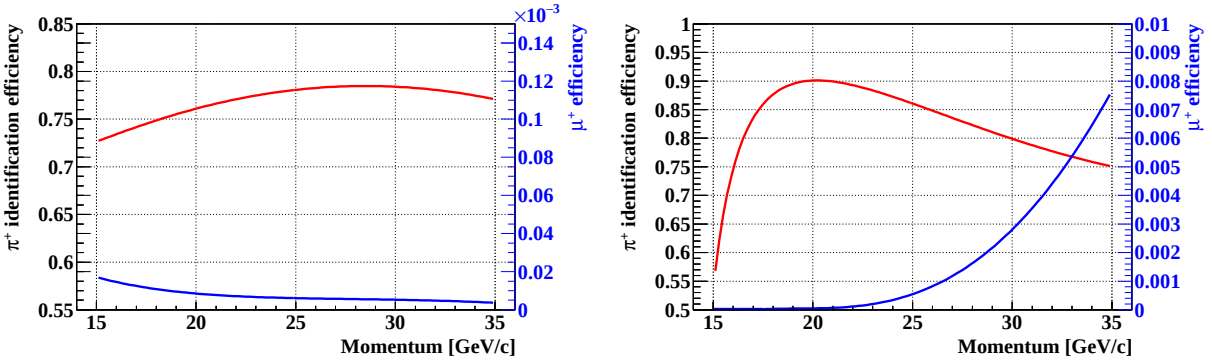

Figure 5.1: *Particle identification performance: Calorimetric (left), RICH (right). Note the different scales for the π^+ and the μ^+ efficiencies.*

offline window of 15 ns. This is not simulated in the MC, but the difference should not affect the $K_{\pi\nu\bar{\nu}}$ measurement, because it is present for both signal and normalization. However, this difference is conservatively added as a systematic uncertainty on the single event sensitivity.

5.2 Particle identification with RICH

The samples $K^{\mathrm{RICH}}_{\pi\pi}$ ($K^{\mathrm{RICH}}_{\mu\nu}$) with control-trigger $K_{\pi\pi}$ ($K_{\mu 2}$) decays are used to measure the π^+/μ^+ separation with the RICH. Calorimetric particle identification is applied to both samples to select the $\pi^+(\mu^+)$, respectively. The selection details are listed in Sections A.1 and A.2.

The results are shown in Figure 5.1-right. The average π^+ efficiency in the (15, 35) GeV/c momentum range is $\epsilon^{\pi}_{\mathrm{RICH}} = (82.35 \pm 0.04)\%$, with a μ^+ rejection of $\epsilon^{\mu}_{\mathrm{RICH}} = (0.219 \pm 0.001)\%$. The quoted uncertainties are statistical.

The sources of inefficiency in the RICH identification are: the standalone ring reconstruction performance, dominating at low momenta as the π^+ momentum approaches the threshold for production of Cherenkov radiation; the multi-ring likelihood algorithm performance, the strong cut on the RICH mass M(RICH), dominating at high momentum. The results are reproduced by the MC simulation within 6%, which is assigned as a systematic uncertainty on the single event sensitivity.

5.3 Neutral pion rejection

The photon rejection procedure suppresses extra clusters of energy deposition in-time with the track. The algorithm exploits the two body kinematics of the $K^+ \to \pi^+\pi^0$ decay, as well as the correlation between the photons from the subsequent $\pi^0 \to \gamma\gamma$ decay.

As an example one can consider the case of a 20 GeV/c π^+ track. The average momentum of a beam K^+ is 75 GeV/c, leaving an average energy of 55 GeV to the π^0. In asymmetric configurations where one photon has $E_\gamma > 50$ GeV and the other has $E_\gamma < 5$ GeV, the lower energy photon is more likely to reach one of the LAV stations or escape between two neighboring LAVs. The detection efficiency decreases with energy and the probability for a low energetic photon to escape increases. Applying a strict rejection of high-energy photons circumvents this

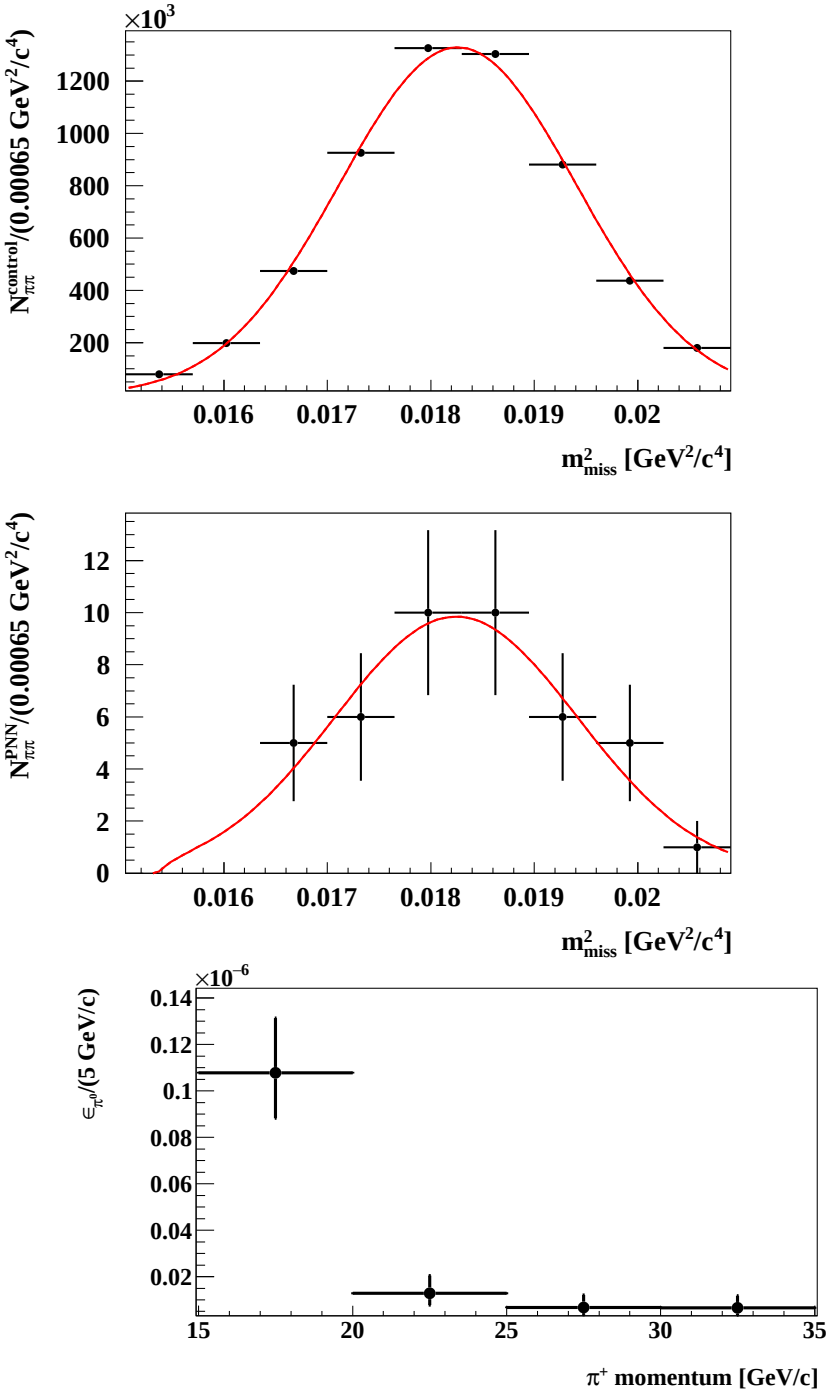

Figure 5.2: *Top left: number of control-trigger normalization events $N_{\pi\pi}^{control}$ in the $\pi\pi$ region before the π^0 rejection is applied. Top right: number of events $N_{\pi\pi}^{PNN}$ after the π^0 rejection triggered by the PNN trigger chain. The data is displayed as black dots and the fitted distributions with red line. Bottom: fraction of $K_{\pi\pi}$ events after the π^0 rejection is applied.*

effect.

In contrast, configurations where both photons in the LKr have medium-range energies are easier to reject and the veto condition can be kept looser. The size of the veto time windows in each calorimeter is chosen to be energy-dependent to achieve optimal rejection without loosing too much signal.

Hit multiplicity is further applied to suppress photons converting in the RICH mirrors. The electrons produced in the conversions will give rise to signals in the charged hodoscopes and deposit energy in the LKr, but in some cases not enough to have an associated reconstructed cluster. Exploiting correlations between energy deposits in LKr cells in-time with the pion track and signals in the hodoscopes, gives the last contribution to the $K_{\pi\pi}$ background rejection.

The fraction of $K_{\pi\pi}$ events surviving the π^0 veto conditions is computed as

$$\epsilon_{\pi^0} = \frac{N_{\pi\pi}^{\mathrm{PNN}}}{D \cdot N_{\pi\pi}^{\mathrm{control}} \cdot \epsilon_{\mathrm{RV}} \cdot \epsilon_{\mathrm{trigger}}}. \tag{5.1}$$

Here $N_{\pi\pi}^{\mathrm{PNN}}$ is the number of $K_{\pi\pi}$ after the full $\pi\nu\bar{\nu}$ selection is applied on PNN-trigger data; $N_{\pi\pi}^{\mathrm{control}}$ is the number of $K_{\pi\pi}$ after the $K_{\pi\nu\bar{\nu}}$ selection is applied on control-trigger data before the π^0 veto; D is the downscaling factor of the control trigger, which was 400 in the 2016 data taking. The missing mass distributions before and after the π^0 rejection are presented in Figure 5.2.

A total of 43 events are observed in the $\pi\pi$ region after the rejection, corresponding to

$$\epsilon_{\pi^0} = (2.7 \pm 0.4_{\mathrm{stat}} \pm 0.1_{\mathrm{syst}}) \times 10^{-8}. \tag{5.2}$$

The systematic uncertainty is entirely due to the random veto estimation procedure (see Section 6.5). Background from other kaon decays in the $\pi\pi$ region is negligible. A worse rejection is observed at low momentum, caused by $K_{\pi\pi}$ decays with one photon lost in the beam pipe and the other, having low energy, escaping between two LAV stations. The ϵ_{π^0} efficiency is used to assess the background suppression capabilities of the NA62 detector for events with photons in the final state.

5.4 $K^+ \to \pi^+\pi^0$

The background contribution from $K_{\pi\pi}$ decays in a given signal or control region (as defined in Section 4.5.6) is computed as:

$$N_{\pi\pi}^{exp}(region) = \sum_j N_j(\pi\pi) \cdot f_j^{kin}(region), \tag{5.3}$$

where $N(\pi\pi)$ is the number of PNN-trigger events in the $\pi\pi$ region for the jth momentum bin after the $K_{\pi\nu\bar{\nu}}$ selection (Figure 4.18) and $f_j^{kin}(region)$ is the corresponding fraction of events entering *region* due to the kinematic resolution. The background is estimated summing over the four 5 GeV/c-wide π^+ momentum bins in the (15, 35) GeV/c range. The non-radiative $K_{\pi\pi}$ background is estimated using data. Simulations are used to cross-check the sources of kinematic misreconstruction, but are not used in the background estimation. The π^0 rejection

P_π[GeV/c]	15-20	20-25	25-30	30-35	Total
	Data $K_{\pi\pi}$ ($\pi^0 \to \gamma\gamma$ control)				
CR1	112(2)	109(2)	116(1)	123(2)	115(1)
CR2	204(3)	211(2)	203(2)	195(2)	203(1)
R1	4.4(4)	5.3(4)	5.8(3)	4.7(3)	5.1(2)
R2	9.1(6)	7.4(4)	7.0(4)	7.1(3)	7.4(2)
	MC $K_{\pi\pi}$ ($\pi^0 \to \gamma\gamma$ control)				
CR1	93(1)	83(1)	82(1)	80(1)	83(1)
CR2	141(2)	139(2)	137(1)	135(1)	138(1)
R1	5.1(4)	5.2(3)	5.4(3)	5.4(3)	5.3(2)
R2	6.0(4)	6.1(3)	5.4(2)	5.4(3)	5.6(2)
	MC $K_{\pi\pi}$ ($\pi\nu\overline{\nu}$-like)				
CR1	92(1)	85(1)	84(1)	84(1)	85(1)
CR2	160(2)	154(2)	154(1)	154(1)	154(1)
R1	5.0(2)	6.1(2)	5.9(2)	5.8(2)	5.8(1)
R2	37.7(7)	36.1(5)	32.8(5)	30.5(5)	33.5(2)

Table 5.1: *Fractions f^{kin} of the kinematic tails m^2_{miss} distribution, measured on $K_{\pi\pi}$ samples selected on control data reconstructing the π^0 (Data $K_{\pi\pi}$ $\pi^0 \to \gamma\gamma$ control); on MC reconstructing the π^0 as in data (MC $K_{\pi\pi}$ $\pi^0 \to \gamma\gamma$ control); on MC without the π^0 reconstruction (MC $K_{\pi\pi}$ $\pi\nu\overline{\nu}$-like). The fractions f^{kin} is in units of* 10^{-4}.

is assumed to be independent of the kinematic resolution.

The kinematic tails $f^{kin}_j(region)$ are measured using a sample of $K_{\pi\pi}$ decays selected by reconstructing the π^0 from two photons in the LKr, described in the $K_{\pi\pi}$ control sample selection in Section A.1. The tails are also measured using the same selection on a dedicated MC simulation of $K_{\pi\pi}$ decays with 300 MHz pileup tracks overlaid in the GTK detector. The tails due to radiative $K_{\pi\pi\gamma}$ decays are not included in this estimation, as they are not present in this control sample because of the π^0 reconstruction requirements. LKr activity which is not produced by the two photons from the π^0 decay is rejected, including the radiative photon. Another $K_{\pi\pi}$ selection similar to the normalization ($\pi\nu\overline{\nu}$-like selection) allows the study of possible biases of the tail measurement induced by the $\pi^0 \to \gamma\gamma$ control selection. The m^2_{miss} distribution of the $K_{\pi\pi}$ events in data and the two MC selection are shown superimposed in Figure 5.3-top. The $K_{\pi\pi}$ tails in the two signal regions (R1, R2) and the two control regions (CR1, CR2) are summarized in Table 5.1 for the $\pi^0 \to \gamma\gamma$ control and $\pi\nu\overline{\nu}$-like selections in data and MC simulation as a function of P_π. The simulation reproduces the resolution tails over 4-5 orders of magnitude within 20-30% accuracy. The comparison with the $\pi\nu\overline{\nu}$-like selection shows that the $\pi^0 \to \gamma\gamma$ reconstruction does not bias the resolution tails, but suppresses completely the radiative component. The latter effect is induced by the requirement of two-body kinematics in the $\pi^0 \to \gamma\gamma$ control selection. Simulations without pileup show that the pileup in the GTK accounts for 20%

P_π[GeV/c]	15-20	20-25	25-30	30-35	Total
$N(\pi\pi)$	29	5	6	3	43
$N^{exp}_{\pi\pi}(CR1)$	0.324(62)(6)	0.055(28)(1)	0.069(32)(1)	0.037(26)(1)	0.49(8)(1)
$N^{exp}_{\pi\pi}(CR2)$	0.593(113)(12)	0.105(53)(2)	0.122(55)(2)	0.058(41)(1)	0.88(14)(2)
$N^{exp}_{\pi\pi}(R1)$	0.0127(27)(6)	0.0026(13)(1)	0.0035(16)(2)	0.0014(10)(1)	0.020(4)(1)
$N^{exp}_{\pi\pi}(R2)$	0.0263(53)(13)	0.0037(19)(2)	0.0042(19)(2)	0.0021(15)(1)	0.036(6)(2)

Table 5.2: *Observed number of events in the $\pi\pi$ background region and expected number of $K_{\pi\pi}$ background events in signal and control regions due to kinematic tails after the full $K_{\pi\nu\bar{\nu}}$ selection. The main contribution to the $K_{\pi\pi}$ background comes from the 15-20 GeV/c bin. The contribution of the Poisson fluctuations of $N(\pi\pi)$ in the uncertainties is symmetrized.*

of the resolution tails.

The $K_{\pi\pi}$ non-radiative background expectation, using the tails after the $\pi^0 \to \gamma\gamma$ control selection, is summarized in Table 5.2 and is shown in Figure 5.3-bottom as a function of P_π. The statistical uncertainties on the expected background include the statistical uncertainty on the kinematic tail estimation and the poissonian fluctuation of the observed number of events in the background region $N(\pi\pi)$. A systematic uncertainty of 5% is assigned to the tails in R1 and R2 to account for biases introduced by the π^0 reconstruction. The effect is estimated as the half-difference between the tails measured in data and MC simulation, with applied $\pi^0 \to \gamma\gamma$ reconstruction.

5.5 $K^+ \to \pi^+\pi^0\gamma$

The kinematic tails of the $m^2_{\rm miss}$ distribution in R2 induced by the radiative component of the $K_{\pi\pi}$ decay are about six times larger than the resolution tails, as can be seen from the comparison between the $\pi^0 \to \gamma\gamma$ and the $\pi\nu\bar{\nu}$-like MC selections (Table 5.1). Only the inner bremsstrahlung (IB) component of the radiation is considered. The contributions of the direct emission (DE) and the interference (INT) terms of the amplitude are considered negligible. Using the values from Table 5.2 the fraction of $K_{\pi\pi(\gamma)}$ background events in R2 is

$$N(\pi\pi(\gamma))_{R2}[\text{before } \pi^0 \text{ rejection}] = N(\pi\pi) \cdot [27.9 + 7.4\cdot] \times 10^{-4}. \tag{5.4}$$

The first term accounts for the radiative part of the kinematic tails and the second one the resolution tails measured on the $K_{\pi\pi}$ control sample in data. However, the suppression of radiative events in R2 is 30 times stronger than that of $K_{\pi\pi}$ events under the π^0 mass peak, due to the suppression of the additional photon, as shown by a study of the single-photon efficiency of LKr, LAV, IRC and SAC in data[100]. Using those results we obtain

$$N(\pi\pi(\gamma))_{R2}[\text{after } \pi^0 \text{ rejection}] = N(\pi\pi) \cdot \eta_{\pi^0} \cdot [1/30 \cdot 27.9 + 7.4] \times 10^{-4}, \tag{5.5}$$

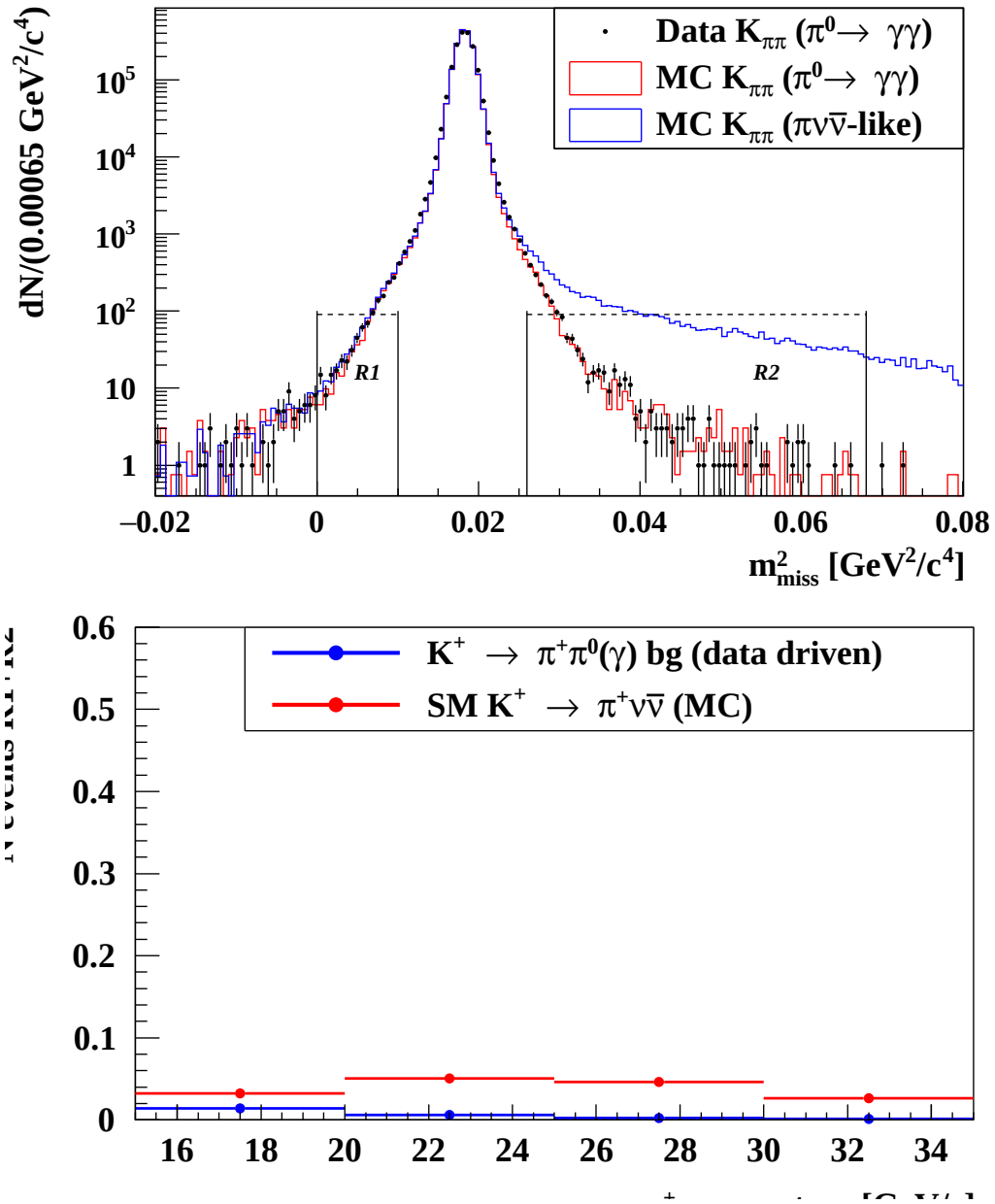

Figure 5.3: *Top: m^2_{miss} distribution of the $K_{\pi\pi(\gamma)}$ control events selected on data reconstructing the π^0 (dots). Two $K_{\pi\pi(\gamma)}$ MC samples are superimposed: one selected as in data (red line) and the other selected without the π^0 reconstruction (blue line). The two vertical red lines lower (higher) than the $m^2_{\pi^0}$ peak indicate R1(2). Bottom: Expected number of $K_{\pi\pi(\gamma)}$ background events in bins of P_π, compared to the expected number of SM $K_{\pi\nu\bar{\nu}}$ events..*

P_π[GeV/c]	15-20	20-25	25-30	30-35	Total
	Data $K_{\mu\nu}$ control				
CR	53.3(5)	67.5(5)	81.0(1)	89.2(4)	77.0(2)
R1	0.37(4)	0.97(6)	1.78(7)	4.42(9)	2.31(4)
R2	0.29(4)	0.25(3)	0.23(4)	0.20(2)	0.23(1)
	MC $K_{\mu\nu}$ control				
CR	52(1)	79(2)	71(1)	100(2)	79(2)
R1	0.5(2)	0.8(2)	1.5(2)	3.5(3)	1.9(1)
R2	0.16(9)	0.18(8)	0.16(7)	0.16(7)	0.17(4)
	MC $K_{\mu\nu}$ $\pi\nu\overline{\nu}$-like				
CR	185(1)	152(1)	137(1)	127(2)	143(1)
R1	0.42(6)	0.83(3)	1.43(7)	2.96(9)	1.73(4)
R2	0.45(6)	0.30(3)	0.38(3)	0.41(3)	0.38(2)

Table 5.3: *Fractions f^{kin} of the kinematic tails of the m^2_{miss} distribution measured on $K_{\mu\nu(\gamma)}$ control data (Data $K_{\mu\nu}$ control); on MC simulation selected as in data (MC $K_{\mu\nu}$ control); on MC simulation using a similar to the $K_{\pi\nu\overline{\nu}}$ selection, but without applying the particle identification (MC $K_{\mu\nu}$ $\pi\nu\overline{\nu}$-like). The tail fractions f^{kin} are in units of* 10^{-4}.

where η_{π^0} is the fraction of $K_{\pi\pi}$ events passing the π^0 rejection (see Section 5.3). Since $N(\pi\pi)\cdot\eta_{\pi^0}$ is the number of PNN-trigger events remaining in the $\pi\pi$ region after the $K_{\pi\nu\overline{\nu}}$ selection, the number of expected $K_{\pi\pi(\gamma)}$ events in R2 after the π^0 rejection is

$$N(\pi\pi(\gamma))_{R2}[\text{after } \pi^0 \text{ rejection}] = 43 \cdot [0.93 + 7.4] \times 10^{-4}, \tag{5.6}$$

showing that the radiative contribution is about 13% of the non-radiative $K_{\pi\pi}$ background in R2. Applying this fraction to the expectation in Table 5.2 one gets for the $K_{\pi\pi\gamma}$ background

$$N^{exp}_{\pi\pi\gamma}(R2) = 0.004 \pm 0.004. \tag{5.7}$$

Conservatively, an error of 100 % is assigned as a systematic uncertainty.

5.6 $K^+ \to \mu^+\nu_\mu(\gamma)$

The background contribution from $K_{\mu\nu(\gamma)}$ decays is computed as:

$$N^{exp}_{\mu\nu}(region) = \sum_j N_j(\mu\nu) \cdot f^{kin}_j(region), \tag{5.8}$$

where $N(\mu\nu)$ is the number of PNN-trigger events in the $\mu\nu$ region for the jth momentum bin after the $K_{\pi\nu\overline{\nu}}$ selection (Figure 4.18) and $f^{kin}_j(region)$ is the tail fraction in the corresponding signal or control region. The background is estimated summing over the π^+ momentum bins in

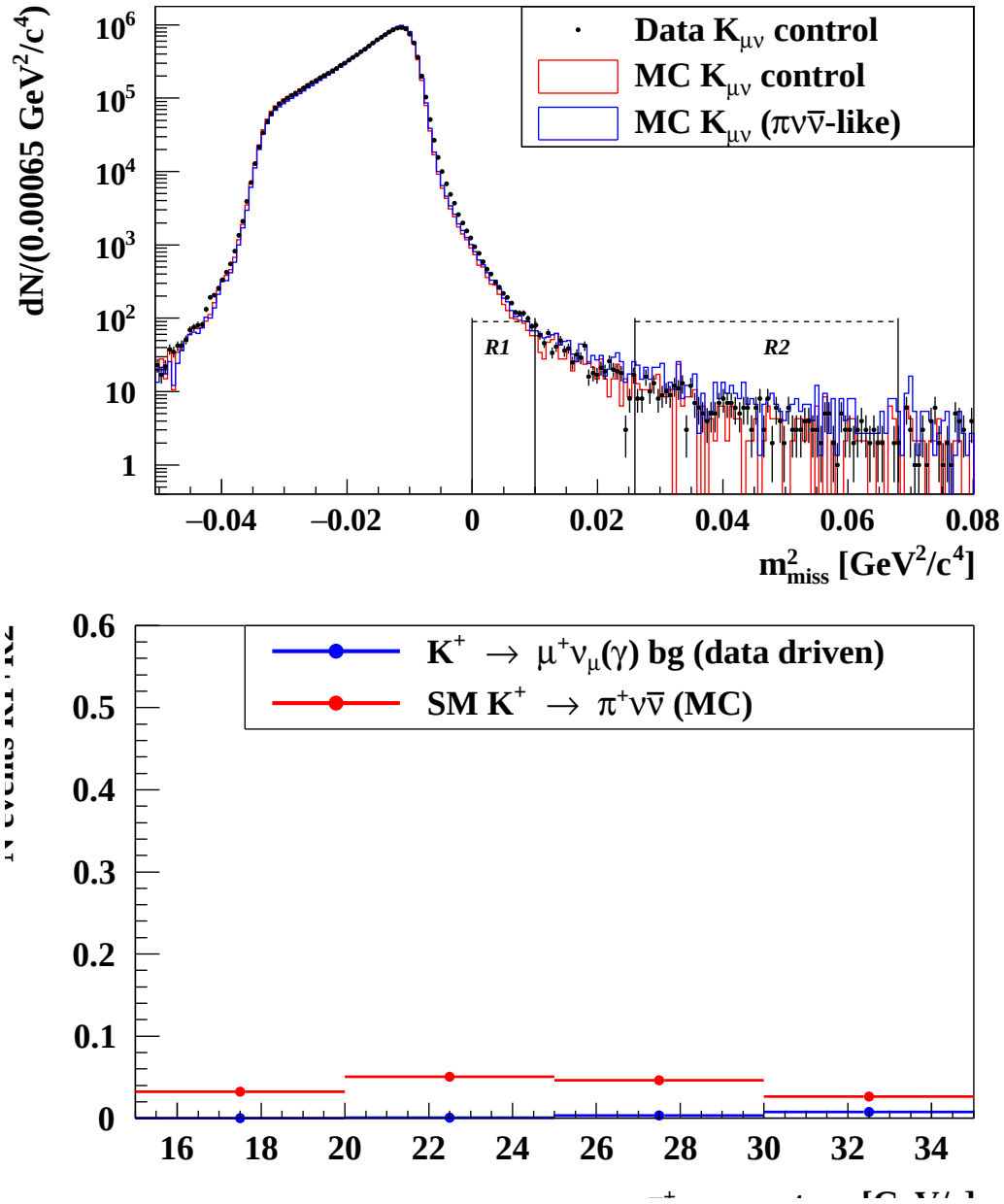

Figure 5.4: *Left: m^2_{miss} distribution of the $K_{\mu\nu(\gamma)}$ control events selected on data (dots). Two $K_{\mu\nu(\gamma)}$ MC samples are superimposed: one selected as in data (red line) and the other selected without particle identification(blue line). The two vertical red lines at lower(higher) m^2_{miss} correspond to R1(2). Right: Expected number of $K_{\mu\nu(\gamma)}$ background events in bins of P_π momentum, compared to the expected number of SM $K_{\pi\nu\bar{\nu}}$ events.*

P_π[GeV/c]	15-20	20-25	25-30	30-35	Total
$N(\mu\nu)$	0	6	9	31	46
$N^{exp}_{\mu\nu}(CR)$	< 0.007	0.040(18)(4)	0.081(28)(8)	0.276(53)(28)	0.404(60)(40)
$N^{exp}_{\mu\nu}(R1)$	$< 5{\cdot}10^{-5}$	0.0006(3)(1)	0.0016(6)(2)	0.0137(27)(14)	0.0159(27)(16)
$N^{exp}_{\mu\nu}(R2)$	$< 4{\cdot}10^{-5}$	0.0002(1)(1)	0.0002(1)(1)	0.0006(1)(3)	0.0010(2)(5)

Table 5.4: *Observed number of events in the $\mu\nu$ background region and expected number of $K_{\mu\nu(\gamma)}$ background events in signal and control regions due to kinematic tails after the full $K_{\pi\nu\bar{\nu}}$ selection.*

the (15, 35) GeV/c range. $N(\mu\nu)$ and $f^{kin}(region)$ are assumed to be independent.

The $\mu\nu$ region is defined as $m^2_{miss} < m^2_{kin} + 3 \cdot \sigma_{res}$ and the CR is between 0 and $m^2_{miss} \geq m^2_{kin} + 3 \cdot \sigma_{res}$. Here $m^2_{kin} = (m^2_{\pi^+} - m^2_{\mu^+}) \cdot (1 - 75[\text{GeV}/c]/P_\pi)$ is the reconstructed $K_{\mu\nu}$ squared missing mass under the π^+ mass hypothesis for the track and $\sigma_{res} = 0.0012$ GeV$^2/c^4$ is the $K_{\mu\nu}$ squared missing mass resolution measured using MC. The tails are computed for each of the four 5 GeV/c momentum bins. The m^2_{kin} for each bin is computed using for P_π the maximum momentum in that bin.

The fraction $f^{kin}_j(region)$ is measured using a sample of $K_{\mu\nu}$ decays in data selected by requiring a MIP-like signal in the calorimeters for positive muon identification and a hit in the MUV3 detector. Details of the $K_{\mu\nu}$ control selection are given in Section A.1. The $f^{kin}_j(region)$ is in addition measured on MC as a cross-check. The simulation includes a 300 MHz pileup component in the GTK detector. The pileup contribution to the $K_{\mu\nu}$ tails is about 10%.

A comparison with simulated $K_{\mu\nu(\gamma)}$ decays shows good agreement across 6 orders of magnitude, as shown in Figure 5.4. Radiative $K_{\mu\nu(\gamma)}$ decays (IB component) are included and are responsible for the tails in R2. The $K_{\mu\nu(\gamma)}$ background is estimated using the kinematic tails (Table 5.3) measured on control data. The uncertainties on f^{kin} are statistical. The number of remaining events and the number of expected $K_{\mu\nu}(\gamma)$ background are presented in Table 5.4. The statistical uncertainty of the background estimation includes the statistical uncertainty on the kinematic tails and the poissonian fluctuation of the observed number of events in the $\mu\nu$ background region. Conservative systematic uncertainties on $N^{exp}_{\mu\nu}$ of 10% in R1 and 50% in R2 are assigned to account for possible biases in the sample used to measure the $K_{\mu\nu}$ kinematic distribution.

5.7 $K^+ \to \pi^+\pi^+\pi^-$

The background contribution from $K_{\pi\pi\pi}$ decays is computed as

$$N^{exp}_{\pi\pi\pi} = \sum_j N_j(\pi\pi\pi) \cdot f^{kin}_j, \tag{5.9}$$

where $N_j(\pi\pi\pi)$ is the number of events in the $\pi\pi\pi$ region for the jth momentum bin and f^{kin}_j are the $K_{\pi\pi\pi}$ kinematic tails. The $K_{\pi\pi\pi}$ kinematic boundary of $4m^2_{\pi^+} = 0.077$ GeV$^2/c^4$ is far

P_π[GeV/c]	15-20	20-25	25-30	30-35	Total
$N(\pi\pi\pi)$	15	5	0	0	20
$N^{exp}_{\pi\pi\pi}(R2)$	0.0015(4)(5)	0.0005(2)(5)	$< 10^{-4}$	$< 10^{-4}$	0.0020(5)(20)

Table 5.5: *Observed number of events in the $\pi\pi\pi$ background region and expected number of $K_{\pi\pi\pi}$ background events in signal and control regions due to kinematic tails after the full $K_{\pi\nu\bar{\nu}}$ selection. Kinematic tails for $K_{\pi\pi\pi}$ are assumed to be 10^{-4}.*

Sample(Q_{track})	Acceptance	N^{exp}(MC)	N^{obs}(DATA)
BIF(−)	$4.3(1) \times 10^{-6}$	15.4 ± 1.7	8
BIF(−) + RICH	$1.1(1) \times 10^{-6}$	4.0 ± 0.4	2
FULL(−)	$8.9(5) \times 10^{-7}$	3.2 ± 0.2	3
FULL(−) + RICH	$2.0(2) \times 10^{-7}$	0.7 ± 0.1	1
BIF(+)	$3.4(3) \times 10^{-7}$	1.2 ± 0.1	5

Table 5.6: *Comparison between K_{e4} MC expectation and observed data events for 5 different selections, all orthogonal to the $K_{\pi\nu\bar{\nu}}$ selection.*

above R2, so the background contribution is low and only in R2.

The expected background from $K_{\pi\pi\pi}$ decays is presented in Table 5.5. An upper limit of 10^{-4} is conservatively assigned to the tails, based on a study of $K_{\pi\pi\pi}$ decays[101]. The poissonian fluctuation of the observed number of events in the $\pi\pi\pi$ background region is taken as a statistical uncertainty. A systematic uncertainty of 100 % is assigned to account for possible differences between the kinematic distributions of the control sample used to measure the tails and the remaining events.

5.8 $K^+ \to \pi^+\pi^-e^+\nu_e$

The K_{e4} background decay can only appear in R2, because of its kinematic boundary at $(m_e + m_\pi)^2$. It is estimated using MC simulation. A sample of 387×10^6 K_{e4} decays has been simulated in the 105−165 m fiducial region. The simulation is validated using five different control selections, orthogonal to the $K_{\pi\nu\bar{\nu}}$ selection:

- **BIF(+)**: Bifurcated region, selected using the complete $K_{\pi\nu\bar{\nu}}$ selection with the spectrometer-related part of the multiplicity applied as a positive requirement instead of a veto condition;
- **BIF(−)**: Same as BIF(+), but the single tracks must be negative;
- **BIF(−)+RICH**: BIF(−), but RICH particle identification is applied in addition;
- **FULL(−)**: Full $K_{\pi\nu\bar{\nu}}$ selection applied to negative single tracks;
- **FULL(−)+RICH**: Same as FULL(−), but with RICH identification applied in addition.

P_π[GeV/c]	15-20	20-25	25-30	30-35	Total
R1	0	0	0	0	0
R2	0.005(12)(5)	0.005(12)(5)	0.005(12)(5)	0.005(12)(5)	0.018(24)(9)

Table 5.7: *Expected K_{e4} background events in R1 and R2 signal regions. The results for each momentum bin is just the total K_{e4} expectation in R2 divided by 4, due to lack of statistics to evaluate it for each bin.*

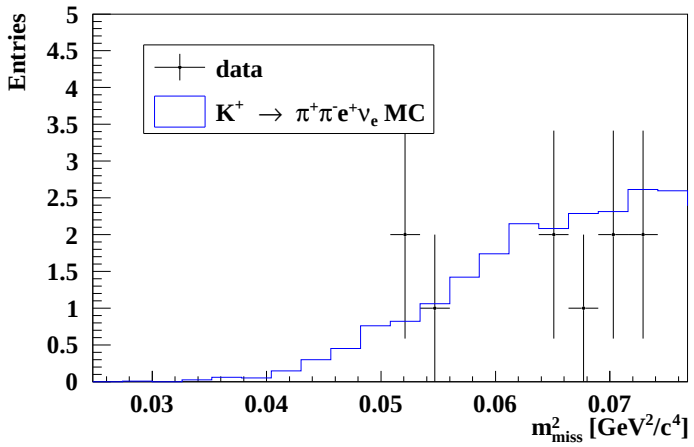

Figure 5.5: *Distribution of the m^2_{miss} for the BIF(−) sample. The K_{e4} MC simulation is denoted by blue lines and data with black dots.*

The $m^2_{\rm miss}$ region used for the validation is $0.026 < m^2_{\rm miss} < 0.072$ GeV$^2/c^4$, because it is free from other background processes. The comparison between data and MC simulation is shown in Table 5.6. There is an agreement across the five validation samples with no statistically significant discrepancies. The shape of the missing mass spectrum is matching the expectation within the limited statistical accuracy, as shown for the BIF(−) sample in Figure 5.5. Half of the difference between the MC expectations and observed data events for the BIF(−) sample is quoted as a systematic uncertainty. This is the sample where the discrepancy is the largest.

Two events survive the full $K_{\pi\nu\overline{\nu}}$ selection in the MC simulation, corresponding to $Acc_{\pi\pi e\nu} = 5(7)_{stat} \times 10^{-9}$. The uncertainty is symmetrized poissonian and quoted at 68% CL, symmetrized using the larger value. The background expectation is shown in Table 5.7. The background is considered constant over the momentum range and the uncertainties are propagated accordingly. Statistical uncertainties are symmetrized taking the larger of the two as an uncertainty on the background expectation.

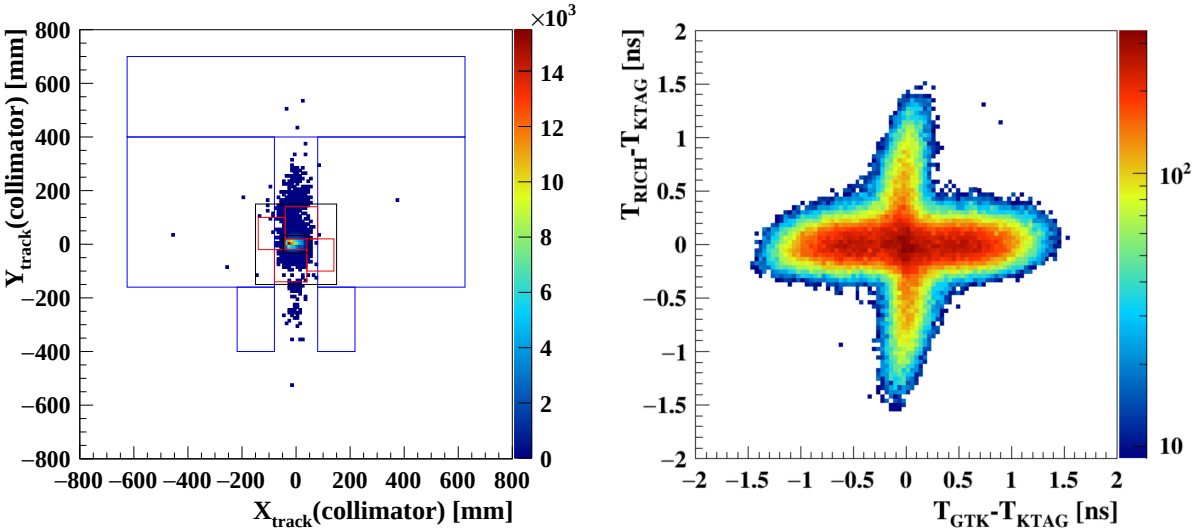

Figure 5.6: *Left: Projection in the (x, y) plane at the final collimator z-position of the π^+ tracks passing the $K_{\pi\nu\bar{\nu}}$ selection, but with K^+-π^+ associated inverted. The CHANTI veto and the geometrical cut described in Section 4.5.1 are not applied. Right: Time difference between RICH and KTAG versus GTK and KTAG for the π^+s shown on the left plot. The three components of the upstream background described in the text can be identified: the accidental band centered at $T_{RICH} - T_{KTAG} = 0$ (type 1) ; the accidental band centered at $T_{GTK} - T_{KTAG} = 0$; component centered at $(T_{RICH} - T_{KTAG} = 0, T_{GTK} - T_{KTAG} = 0)$ (type 3).*

5.9 Upstream background

Upstream events are classified in three different categories:

1. a π^+ from a K^+ decay in the beam line region between the GTK2 and GTK3 detectors is associated to an accidental track in the GTK detector;

2. a π^+ from interactions of a beam track with the GTK2 or GTK3 detectors is associated to an accidental K^+ GTK track;

3. a π^+ from interactions of a K^+ with GTK3 is produced as a prompt particle from the interaction process or a decay product of longer living particles like K_S or K_L.

The interpretation of the upstream events in terms of the above topologies is supported by the analysis of the PNN-trigger events passing the $K_{\pi\nu\bar{\nu}}$ selection, inverting the K^+-π^+ association and not applying the cuts on Z_{vertex}, CHANTI and the geometrical cut described in Section 4.5.1. The distribution of the XY position of the π^+ extrapolated to the final collimator z-position (Figure 5.6-left) suggests that the π^+s at positive Y and around the beam axis in X originate from a region upstream of the final collimator and enter the decay volume depending on the amount of material and the magnetic fields encountered along their path. The π^+s travelling closer to the beam axis are compatible with products of beam-GTK3 interactions. Interactions

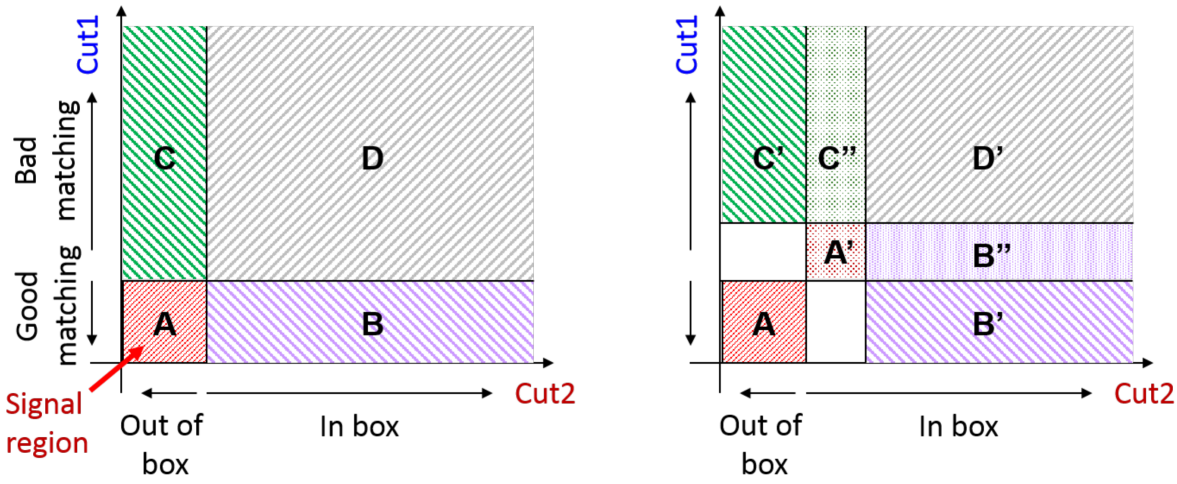

Figure 5.7: *Left: Illustration of the bifurcation method. Selection criteria Cut1 and Cut2 are defined in the text. The reference conditions for $Cut1_0$ and $Cut2_0$ define: sample A, corresponding to the signal and the bifurcated samples B, C, D used to evaluate the expected number of background events in A. Right: Validation procedure of the bifurcation method: samples B', C', D' are selected by varying conditions on Cut1 and Cut2 to give the same expected background as B, C and D within the statistical uncertainty under the hypothesis of independence between Cut1 and Cut2. The expected number of background events in control region A' is evaluated using samples B'', C'' and D'' to be compared with the observation. Samples B'' and C'' are defined by varying Cut1 and Cut2. Background expectations in A and A' are computed according to* (5.10) *and* (5.12).

with the GTK2 station can also explain the π^+s observed at negative Y positions. The time structure of these events is shown in Figure 5.6-right: the horizontal band is compatible with π^+s of type 1, as the KTAG-RICH time coincidence is compatible with the expected $O(100)$ ps time resolution. Similarly the vertical band can be explained by π^+s of type 2 as GTK and KTAG are in time within the expected resolution. The third type of upstream events should manifest themselves as a 2-dimensional coincidence between GTK-KTAG and KTAG-RICH. Studies of the x and y projections of the timing 2D plot of Figure 5.6-right indicate that the central peak could be simply explained by the superposition of the distribution of events of types 1 and 2, suggesting that type 3 events are at least an order of magnitude lower than the others. Type 3 events include charge exchange processes producing K_S and K_L ($K^+n \to pK_S(K_L)$). Decays of the neutral kaons to $\pi^+\pi^-$ or $\pi^+l^-\nu_l$ can mimic the signal if the π^- or the $l^-\nu_l$ is lost. This background is included in the upstream background estimation.

Residual upstream events after the $K_{\pi\nu\bar{\nu}}$ selection form the upstream background. It is estimated from data using a bifurcation analysis. The K^+-π^+ association (later referred to as *Cut1*) and the geometrical box cut at the final collimator z-position (later referred to as *Cut2*) are used as independent criteria to select bifurcated samples, after applying all the other criteria of the $K_{\pi\nu\bar{\nu}}$ analysis. The reference conditions on *Cut1* and *Cut2*, indicated as $Cut1_0$ and $Cut2_0$, are:

$Cut1_0$: K^+-π^+ discriminant (4.13) greater than 0.01 (0.005) if $T_{\rm KTAG}$ ($T_{\rm RICH}$) time is used as

j	$Cut1_j$	$Cut2_j$ [mm]
1	$D > 0.001$	$!(\|x\| < 50\ \&\ \|y\| < 350)$
2	$0.0003 < D < 0.001$	$!(\|x\| < 15\ \&\ \|y\| < 350)$
3	$0.0003 < D < 0.001$	$!(\|x\| < 50\ \&\ -500 < y\ \&\ y < 50)$
4	$0.0003 < D < 0.001$	$!(\|x\| < 50\ \&\ -50 < y\ \&\ y < 500)$
5	$0.0003 < D < 0.001$	$!(\|x\| < 50\ \&\ \|y\| < 50)$

Table 5.8: *Set of conditions on Cut1 and Cut2 used to validate the upstream background estimations.*

reference, denoted by $D > 0.01$ ($D_{\mathrm{RICH}} > 0.005$) in the following; time difference between T_{KTAG} and T_{GTK} less than ± 0.6 ns; $CDA < 7$ mm.

$Cut2_0$: downstream track projected at the final collimator longitudinal position outside a box $|X| < 100$ mm and $|Y| < 500$ mm wide.

The bifurcation technique is illustrated in Figure 5.7.

Reference conditions $Cut1_0$ and $Cut2_0$ define the reference set made of four samples: A, B, C and D. A is the signal sample kept masked; B, C and D are the bifurcated samples used to estimate the expected background in A. If criteria *Cut1* and *Cut2* are independent and the events in the bifurcated samples are all of the same nature (upstream events in this case), the expected number of background events A_{exp}, in the signal region is:

$$A_{\mathrm{exp}} = \frac{B \cdot C}{D}. \tag{5.10}$$

Here B, C and D stand for the observed number of events in the corresponding bifurcated samples. The validation of this method is done by varying the conditions on *Cut1* and *Cut2* to define the bifurcated samples A', B', C', B'', C'' and D': if the hypothesis of independence between *Cut1* and *Cut2* is true, the following relations hold:

$$A_{\mathrm{exp}} = \frac{B' \cdot C'}{D'} \tag{5.11}$$

$$A'_{\mathrm{exp}} = \frac{B'' \cdot C''}{D'} = A'_{\mathrm{obs}}. \tag{5.12}$$

Here A'_{exp} and A'_{obs} stands for the expected and observed number of background events in region A', respectively; the other labels indicate the observed number of events in the corresponding samples. Five sets of conditions on *Cut1* and *Cut2* denoted by $Cut1_j$ and $Cut2_j$ ($j = 1..5$) are used to validate the estimation of A with the reference set. The definition of the conditions used to define the validation sets is given in Table 5.8.

Samples A, B, C and D and samples A', B', C', B'', C'' and D' corresponding to each validation sets are defined as shown in Figure 5.7.

D'	B'	C'	B''	C''	$A_{\rm exp}$	$A'_{\rm exp}$	$A'_{\rm obs}$
249	15	1	33	17	0.06 ± 0.02	2.4 ± 0.7	3
135	7	1	7	99	0.05 ± 0.02	$5.1^{+2.5}_{-2.0}$	8
42	2	1	2	192	$0.05^{+0.05}_{-0.03}$	9^{+10}_{-6}	13
201	14	1	14	33	0.07 ± 0.02	2.3 ± 0.8	1
9	1	1	1	225	$0.11^{+0.20}_{-0.07}$	25^{44}_{-16}	14

Table 5.9: *Results of the validation procedure for upstream background. Statistical errors on A_{exp} are uncorrelated to that of table 5.10, i.e. the fluctuation on C is factorized out because the only event of samples C' is always the same for each validation set and the same as that of sample C.*

D	B	C	$A_{\rm exp}$
302	15	1	$0.05^{+0.09}_{-0.03}$

Table 5.10: *Expected background from upstream tracks predicted using samples A, B, C, D. The Poisson fluctuation of D, B, C are considered and errors are at 68% CL.*

The results for the expected upstream background events and the validation methods are summarized in Tables 5.9 and 5.10. The results from the validation sets are in agreement with the expectations and observations within the statistical uncertainties and validate the expectation of the upstream background in the signal region derived from the reference set. The final estimation is statistically limited. As a further cross-check the pattern of the timing distribution of events of the bifurcated sample D qualitatively resembles the one in Figure 5.6-right, suggesting that the bifurcated samples consist of upstream events.

5.10 $K^+ \to \pi^0 l^+ \nu_l$

Background from $K^+ \to \pi^0 l^+ \nu_l$ (K_{l3}), with $l = \mu$, e, is expected low as these processes involve the simultaneous presence of a lepton and a π^0. The background contamination is evaluated using MC simulation together with the measured particle identification (PID) performances and photon rejection efficiency on data. The π^+ PID criteria in the calorimeters and the RICH are assumed independent and uncorrelated to the photon rejection. The acceptance $A_{K_{l3}}$ is the fraction of K_{l3} events passing the $K_{\pi\nu\bar{\nu}}$ selection before applying PID, photon and multiplicity rejection. Both the MC simulation and the μ^+ and e^+ data samples are used to measure the π^+ PID efficiency with calorimeters and RICH. Conservatively, the worse estimation is taken. The fraction of events surviving the photon rejection, ϵ_{π^0}, is taken from K_{l3} simulation after applying the $K_{\pi\nu\bar{\nu}}$ selection without PID. The efficiencies, acceptance and the total background contamination of K_{l3} decays are summarized in Table 5.11. The total number of kaons N_K (Section 6.3) is used as normalization. The random veto and trigger efficiencies are included in

	$K_{\mu 3}$	K_{e3}
$A_{K_{l3}}$	0.082	0.062
$\epsilon_{\text{PID-calo}}$	10^{-5}	10^{-3}
$\epsilon_{\text{PID-RICH}}$	3×10^{-3}	0.25×10^{-3}
ϵ_{π^0}	3×10^{-5}	2×10^{-5}
Branching ratio	0.0335	0.0507
Expected background	0.0002	0.0012

Table 5.11: *Expected background from $K_{\mu 3}$ and K_{e3} decays.*

the background estimation. The PID efficiency $\epsilon_{\text{PID-calo}}$ for $K_{\mu 3}$ is obtained from simulation and agrees with the value of 0.65×10^{-5} measured on data. On the contrary $\epsilon_{\text{PID-RICH}}$ for $K_{\mu 3}$ is taken from data, while simulations report a lower value 0.4×10^{-3}. Both $\epsilon_{\text{PID-calo}}$ and $\epsilon_{\text{PID-RICH}}$ for K_{e3} are taken from simulation. Simulation is used for ϵ_{π^0}, with the inefficiency mostly due to specific geometrical configurations of the two photons. The final estimations of the $K_{\mu 3}$ and K_{e3} backgrounds do not include multiplicity rejection and therefore can be considered conservative upper limits.

5.11 $K^+ \to \pi^+\gamma\gamma$

The $K_{\pi\gamma\gamma}$ background decay is suppressed by its branching ratio (order of 10^{-6}), kinematics and the presence of two photons. In particular, the form factors bring the m^2_{miss} towards the $\pi\pi\pi$ m^2_{miss} region, with about 10% of the events remaining in R2 and corresponding to configurations with two photons in the acceptance of the calorimeters. The simulation shows that the overall acceptance of $K^+ \to \pi^+\gamma\gamma$ after the $K_{\pi\nu\overline{\nu}}$ selection is 1.8%, before applying photon rejection. The fraction of events passing photon rejection without the SAC and multiplicity veto conditions is $< 6.4\times10^{-6}$, when all the events in the full m^2_{miss} spectrum are used. This value is, with confidence, a conservative upper limit because kinematics makes photon rejection less effective at high m^2_{miss}. Moreover, the study of the $K_{\pi\pi}$ background suggests that the multiplicity rejection improves the π^0 rejection by a factor of 5. Assuming that the same factor applies to the $\gamma\gamma$ pair and using N_K for normalization, the above numbers translate in an expected background from $K^+ \to \pi^+\gamma\gamma$ decays of about 0.002. This number can be considered as an upper limit because SAC has not been applied.

5.12 Background summary

The summary of all background processes considered in the $K^+ \to \pi^+\nu\overline{\nu}$ analysis is presented in Table 5.12.

The dominant kaon decay background is the $K_{\pi\pi(\gamma)}$ decay. Most of the $K_{\pi\pi(\gamma)}$ background contribution is present at low π^+ momentum. In such cases the π^0 rejection is less efficient and

Process	Expected events in R1 + R2
$K^+ \to \pi^+\pi^0(\gamma)$ IB	$0.060 \pm 0.007_{stat} \pm 0.003_{syst}$
$K^+ \to \mu^+\nu_\mu(\gamma)$ IB	$0.017 \pm 0.003_{stat} \pm 0.002_{syst}$
$K^+ \to \pi^+\pi^- e^+\nu_e$	$0.018^{+0.024}_{-0.017}\vert_{stat} \pm 0.009_{syst}$
$K^+ \to \pi^+\pi^-\pi^+$	$0.002 \pm 0.001_{stat} \pm 0.002_{syst}$
$K^+ \to \pi^+\gamma\gamma$	< 0.002
$K^+ \to l^+\pi^0\nu_l$	< 0.001
Upstream background	$0.050^{+0.090}_{-0.030}\vert_{stat}$
Total background	$0.15 \pm 0.09_{stat} \pm 0.01_{syst}$

Table 5.12: *Summary of all background processes to the $K^+ \to \pi^+\nu\overline{\nu}$ measurement.*

more than half of the events left in the $\pi\pi$ region have a π^+ momentum below 20 GeV/c. The background is significantly reduced at higher momenta.

The $K_{\mu\nu}$ background decay dominates at high momentum and results from the combination of two effects: as the π^+ momentum increases the kinematic boundary is approaching R1 and the tail fractions are larger; the π^+/μ^+ separation using the RICH becomes worse as both particles approach $\beta = 1$.

The K_{e4} and upstream backgrounds are assumed to be constant over the whole momentum range. The statistics of the data samples used to estimate these backgrounds is not sufficient to study the momentum dependence.

All background expectations are dominated by their statistical uncertainties. This will be improved in the future by adding the 2017-2018 dataset and simulating several billion more K_{e4} decays.

6

$\pi\nu\overline{\nu}$ analysis

6.1 Analysis strategy

The full $K^+ \to \pi^+\nu\overline{\nu}$ analysis presented in this chapter is based on the events passing the selection described in Chapter 4, without the m^2_{miss} and P_π cuts. A simple counting method is used to assess the sensitivity of the analysis. The selection criteria are very similar to those of the signal selection. The number of expected SM $K_{\pi\nu\overline{\nu}}$ events $N^{\rm exp}_{\pi\nu\overline{\nu}}$ is computed as:

$$N^{\rm exp}_{\pi\nu\overline{\nu}} = D \cdot N^{\rm control}_{\pi\pi} \cdot \frac{BR_{\pi\nu\overline{\nu}}}{BR_{\pi\pi}} \cdot \frac{\epsilon_{\pi\nu\overline{\nu}}}{A_{\pi\pi}} \cdot \epsilon_{\rm trig}, \tag{6.1}$$

where $BR_{\pi\nu\overline{\nu}}$ and $BR_{\pi\pi}$ are the SM branching ratios of the $K^+ \to \pi^+\nu\overline{\nu}$ and $K^+ \to \pi^+\pi^0$ decays, respectively[11]; $\epsilon_{\pi\nu\overline{\nu}}$ is the signal detection efficiency; $A_{\pi\pi}$ the normalization acceptance; $\epsilon_{\rm trig}$ is the PNN trigger efficiency which cannot be considered in the selection and D is the downscaling factor applied to the control triggers. The trigger conditions are highly correlated with the selection criteria, because most of them are also applied at analysis level. The control trigger efficiency is 100%.

The signal efficiency $\epsilon_{\pi\nu\overline{\nu}}$ is written as:

$$\epsilon_{\pi\nu\overline{\nu}} = A_{\pi\nu\overline{\nu}} \cdot \epsilon_{\rm RV} \tag{6.2}$$

Here $A_{\pi\nu\overline{\nu}}$ is the full signal acceptance and the $\epsilon_{\rm RV}$ is the signal inefficiency induced by photon and charged multiplicity random veto, which is beam intensity dependent.

The expected background from $K_{\mu\nu}$, $K_{\pi\pi}$ and $K_{\pi\pi\pi}$ decays is evaluated by counting the number of events after the $K_{\pi\nu\overline{\nu}}$ selection in the $\mu\nu$, $\pi\pi$ and $\pi\pi\pi$ background regions, respectively, and extrapolating to the signal regions. The K_{e4} and K_{l3} backgrounds are estimated using MC simulations. Background from upstream K^+ decays and beam-GTK3 inelastic interactions is estimated on data using a bifurcation method.

A blind procedure is adopted for the $BR(K^+ \to \pi^+\nu\overline{\nu})$ measurement to avoid biasing the

Selection stage	$A_{\pi\nu\bar{\nu}}$ [%]	$A_{\pi\pi}$ [%]
Pion + Kaon candidate reconstruction	66.12(2)	61.12(1)
Signal region	13.44(1)	16.11(1)
Charged pion ID calorimeters	10.07(1)	11.57(1)
Charged pion ID RICH	8.81(1)	9.687(4)
Neutral pion rejection	7.18(1)	-
Total acceptance	3.97(1)	9.687(4)

Table 6.1: *Acceptance for signal ($A_{\pi\nu\bar{\nu}}$) and normalization ($A_{\pi\pi}$) after the selection criteria described in Chapter 4. 'Pion + Kaon candidate reconstruction' refers to the selection described in Sections 4.2 and 4.3. 'Signal region' corresponds to the selection in Section 4.4 in the $15 < P_\pi < 35$ GeV/c momentum range and with m^2_{miss} in R1+R2 for $K_{\pi\nu\bar{\nu}}$ and in the $\pi\pi$ region for $K_{\pi\pi}$ (Table 4.4). 'Charged pion identification' selection criteria are described in Sections 4.5.2 and 4.5.3. 'Neutral pion rejection' is detailed in Sections 4.5.4 and 4.5.5. 'Total acceptance' includes the complete kinematic selection using $m^2_{mmiss,\ beam}$ and $m^2_{miss,\ RICH}$ (Section 4.5.6) and the box cut applied in the (X_{TRIM5}, Y_{TRIM5}) plane given in Section 4.5.1.*

analysis. Signal and control regions are kept blind during the whole procedure. Data are unblinded only after both signal and background expectations are finalized.

After outlining the $K_{\pi\nu\bar{\nu}}$ analysis strategy in this section, the signal acceptance determination is presented in Section 6.2. The analysis of the normalization channel is described in Section 6.3. Trigger efficiency is detailed in Section 6.4. The accidental signal loss caused by the photon and charged multiplicity rejection is documented in Section 6.5. Finally, the Single Event Sensitivity (SES) is obtained in Section 6.6.

6.2 Signal acceptance

The signal acceptance $A_{\pi\nu\bar{\nu}}$ is the ratio between the number of MC simulated $K_{\pi\nu\bar{\nu}}$ events passing the signal selection and the number of generated K^+ decays in the fiducial region $105 - 165$ m from the target. The acceptance at the different stages of the $K_{\pi\nu\bar{\nu}}$ selection is shown in Table 6.1. The main source of signal loss is induced by the geometrical acceptance and by the signal region definition in the $(P_\pi, m^2_{\rm miss})$ plane (Figure 6.1-center), followed by the subsequent particle identification efficiency with the RICH and calorimeters and the cuts against upstream background. The total signal acceptance (R1 + R2) after the complete $K_{\pi\nu\bar{\nu}}$ selection is $A_{\pi\nu\bar{\nu}} = (3.965 \pm 0.004_{\rm stat})\%$, shown in Figure 6.1-top for R1 and R2 in bins of P_π. Low values result at low momenta in both regions from the lower RICH reconstruction efficiency and in R2 at high momenta from the extra cut in the $(Z_{\rm vertex}, R_{\rm STRAW1})$ plane.

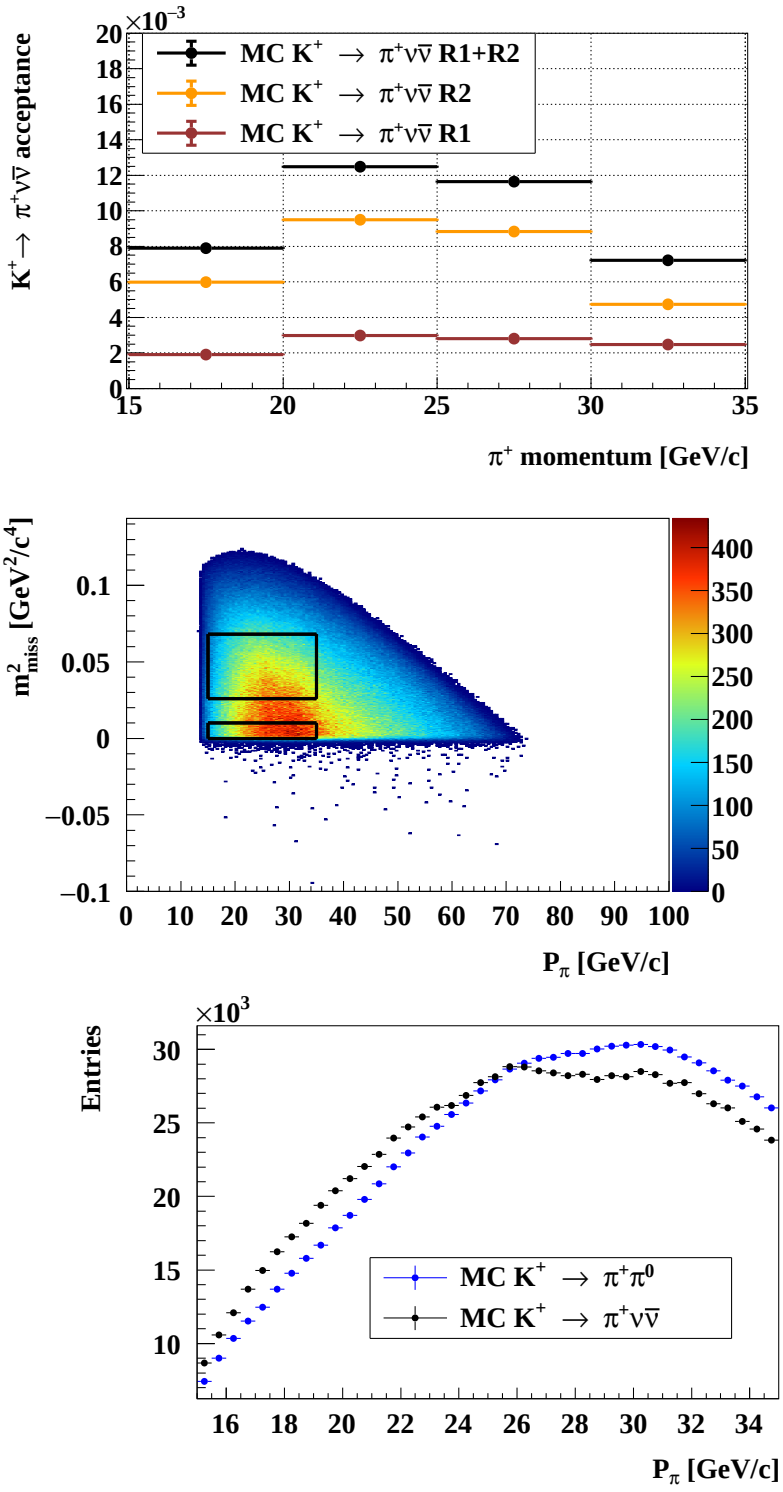

Figure 6.1: *Top: Acceptance for the $K_{\pi\nu\bar{\nu}}$ decay, obtained by $K_{\pi\nu\bar{\nu}}$ MC simulation. The results are presented in bins of momentum for* R1 *(brown dots),* R2 *(orange dots) and combined* R1 + R2 *(black dots). Center: Distribution of the squared missing mass versus the pion track momentum for MC simulated $K_{\pi\nu\bar{\nu}}$ decays after the full selection. Bottom: Comparison between the momentum spectrum of the pion track for $K_{\pi\nu\bar{\nu}}$ (blue) and $K_{\pi\pi}$ (black). The difference in the distributions is assigned as a systematic uncertainty on the kaon flux.*

6.3 Normalization channel

The $K_{\pi\pi}$ decay mode is chosen as normalization for the $K_{\pi\nu\bar{\nu}}$ measurement. This choice ensures first order cancellation of track-related systematic effects, due to the presence of a single pion track in the final state of both decays. Small differences are observed in the P_π spectrum, because the π^+ momentum of the $K_{\pi\pi}$ decay, due to its two-body nature, is slightly higher than that for the $K_{\pi\nu\bar{\nu}}$ three-body decay.

The $K_{\pi\pi}$ normalization decays are selected from control-trigger events, passing the complete $K_{\pi\nu\bar{\nu}}$ selection, except photon and charged multiplicity rejection. The total acceptance is $A_{\pi\pi} = 9.686(4)\%$. The differences between the $K_{\pi\nu\bar{\nu}}$ and $K_{\pi\pi}$ acceptances are mainly due to the full acceptance in $m^2_{\rm miss}$ for the normalization.

In the data sample $N^{\rm control}_{\pi\pi} = 6.145(3) \times 10^6$ normalization events are selected in the $\pi\pi$ background region. Further correction is applied to account for the control trigger downscaling $D = 400$. The total number of kaon decays in the fiducial region is computed as

$$N_K = \frac{N^{\rm control}_{\pi\pi} \cdot D}{A_{\pi\pi} \cdot BR_{\pi\pi}} = 1.21(2)_{\rm syst} \cdot 10^{11}. \tag{6.3}$$

The PDG value of $BR(\pi^+\pi^0) = 0.2067$[11] is used for the $K_{\pi\pi}$ branching ratio. The systematic uncertainty reflects the differences between the $K_{\pi\nu\bar{\nu}}$ and $K_{\pi\pi}$ momentum spectra shown in Figure 6.1-bottom. The statistical uncertainty is 40 times smaller than the systematic one. The 0.4% uncertainty on $BR_{\pi\pi}$ has a negligible contribution.

6.4 Trigger efficiency

The trigger efficiency of the components entering the PNN trigger chain is evaluated using two control samples of $K_{\pi\pi}$ decays: $K^{2\gamma{\rm calo}}_{\pi\pi}$ with the both π^0 photons detected by the LKr and $K^{2\gamma{\rm LAV}}_{\pi\pi}$ where the photons are detected by the LAV detector. The first is used as a reference to study the L0COMB and L0RICH trigger efficiencies. The latter is used as a reference to evaluate the L0CALO trigger efficiency. The samples are described in Section A.1 of the appendix.

Specific conditions are applied offline to reproduce the trigger behavior in the analysis framework. The efficiency is evaluated looking at the L0TP data, which include both the primitive ID and the time of all the primitives sent for each trigger. An event is declared efficient if there is a primitive recorded by the L0TP within ± 10 ns from the time of the reference detector. The reference time for the PNN mask is given by L0RICH. For estimation of the L0RICH efficiency the time of L0NA62CHOD is taken as reference.

The evaluation of the L0CALO efficiency requires a special treatment. At the trigger level, a veto decision is taken depending on the amount of energy deposited in the LKr. The efficiency is then corrected for the probability for a pion to release a certain fraction of its energy in the LKr. The pion $E_{\rm LKr}/P_\pi$ distribution of a π^- track is obtained from a sample of fully reconstructed $K_{\pi\pi\pi}$ decays. For a given π^+ momentum bin, the corresponding $E_{\rm LKr}$ distribution is computed using the π^- $E_{\rm LKr}/P_\pi$ distribution from Figure 6.2-center. The resulting spectrum is then re-weighted with the energy dependent trigger efficiency estimation.

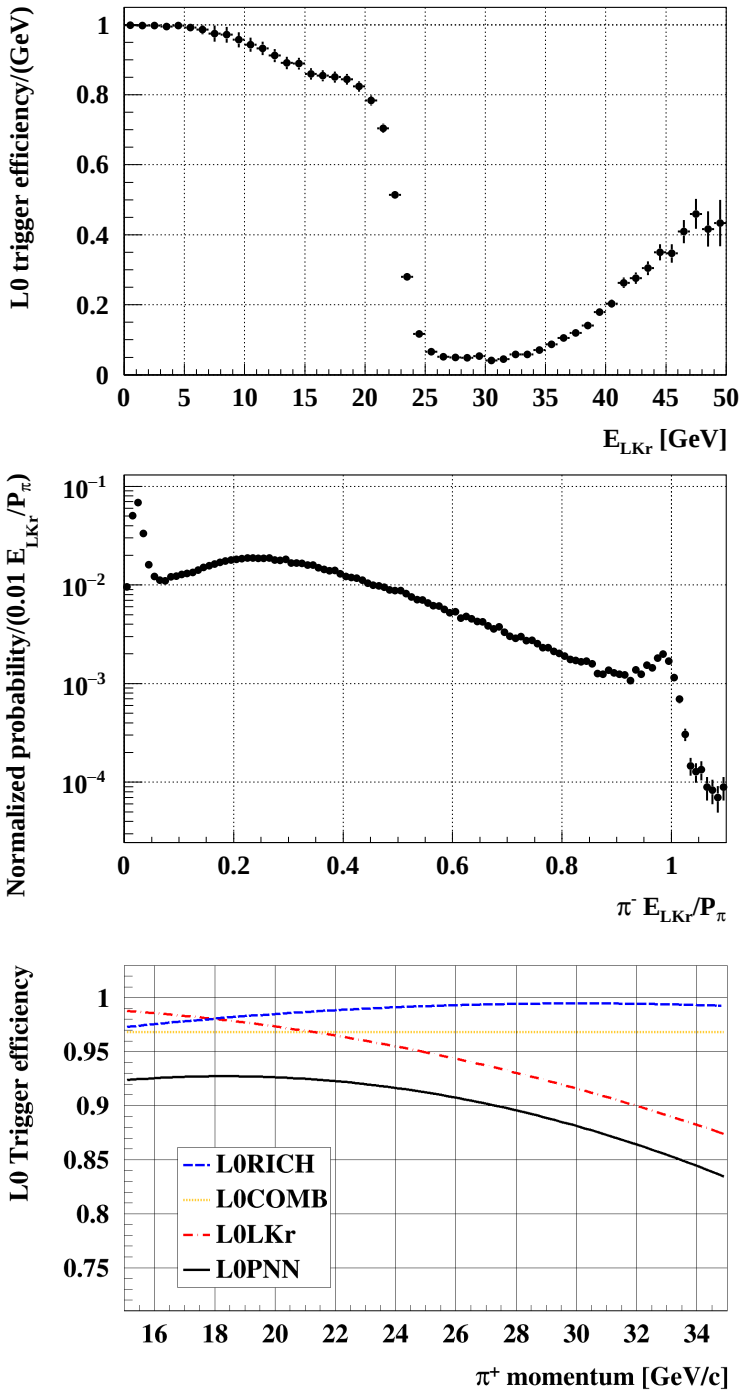

Figure 6.2: *Top: energy dependent L0CALO trigger efficiency. The increased efficiency at high E_{LKr} was due to a known problem in the L0CALO trigger, which was producing primitive signals outside of the online trigger time windows. This effect caused inefficiency in vetoing events with high energy deposits in the LKr. Center: π^- E_{LKr}/P_π spectrum obtained from a $K_{\pi\pi\pi}$ selection. Bottom: Trigger efficiency for each component of the L0PNN trigger chain studied on normalization events. See text for details.*

The L0 trigger efficiency for the full 2016 dataset is presented in Figure 6.2-bottom. The inefficiency of L0COMB caused by a fake veto induced by accidental beam muons is constant. The decrease in L0RICH efficiency at low momentum is due to the decreasing yield of Cherenkov photons emitted by the pion. The L0CALO veto threshold was set to $E_{\text{calo}} > 20$ GeV/c in 2016, which causes the sudden drop of efficiency for energy releases above 20 GeV as shown in Figure 6.2-top. This is not the optimal energy cut for the $K_{\pi\nu\bar{\nu}}$ measurement, because the positron rejection cut $E_{\text{LKr}}/P_{\pi} < 0.8$ allows pion energy releases of up to 28 GeV at 35 GeV/c π^+ momentum. The trigger cut was changed to 30 GeV before the 2017 data taking. The total trigger efficiency is $\epsilon_{\text{trig}} = (88.3 \pm 0.9_{\text{stat}} \pm 2.0_{\text{syst}})\%$ and is corrected for the 97% L1 trigger efficiency, considering that 25% of the events in the PNN mask are "autopass" [102]. A systematic uncertainty equal to the L1 correction is assumed and assigned to the trigger efficiency.

6.5 Multiplicity induced signal loss

The normalization channel contains a π^0, so the π^0 rejection procedure is applied only in the signal selection. Two types of signal loss can occur: one due to multiple hits produced by the pion track; the other due to random veto induced by accidental in-time activity. The former occurs when the track emits a delta ray, further converting to an e^+e^- pair upstream of the charged hodoscopes, or undergoes hadronic interaction in the RICH mirrors, again inducing high multiplicity of particles in the hodoscopes and the LKr. The contribution of this component is simulated in the MC and is already included in the acceptance $A_{\pi\nu\bar{\nu}}$. The latter is dependent on the beam intensity and can only be studied on data.

The signal efficiency ϵ_{RV} is defined as

$$\epsilon_{\text{RV}} = (1 - \eta_{\gamma-\text{loss}}) \cdot (1 - \eta_{\text{mult}}), \tag{6.4}$$

where $\eta_{\gamma-\text{loss}}$ and η_{mult} are the losses due to the photon and multiplicity rejection.

The photon rejection random veto inefficiency $\eta_{\gamma-\text{loss}}$ is measured using the $K^{\text{rveto}}_{\mu\nu}$ sample of muons positively identified by the calorimeters and the RICH (see Section A.2 for details). The cluster-based photon rejection is applied in LAV, SAC and IRC. The random veto is measured to be $\eta_{\gamma-\text{loss}} = (16.4 \pm 2.0_{\text{syst}})\%$. The systematic effects are dominating the uncertainty, because delta rays are included in both the $K^{\text{rveto}}_{\mu\nu}$ sample and the $K_{\pi\nu\bar{\nu}}$ MC simulation and are counted twice. The acceptance loss in the signal MC is 4%, due to both hadronic interactions and delta rays. Half of it is assumed to be due to delta rays and is subtracted from the measured $\eta_{\gamma-\text{loss}}$ value, assuming a systematic uncertainty equal to the correction. The statistical uncertainty is below the per mill level.

The inefficiency η_{mult} is highly correlated with $\eta_{\gamma-\text{loss}}$, because both procedures use the LKr as a veto detector. Therefore, it is measured only after the cluster-based photon rejection is already applied. Events surviving the photon rejection are used as normalization for the η_{mult} measurement. The charged multiplicity rejection relies on the presence of segments in the STRAW and correlated hits in space and time in the CHOD, NA62CHOD and LKr. The combined information is used to identify any charged particle produced upstream of the CHOD. In addition, a veto on the HASC and MUV0 detectors is applied to reject specific topologies

P_π [GeV/c]	15-20	20-25	25-30	30-35
$A_{\pi\pi}$ [%]	1.334(2)	2.391(2)	3.023(3)	2.933(2)
$N_{\pi\pi}^{\text{control}}$ data	863963	1468290	1798430	1782650
D	400			
$BR_{\pi\pi}$	0.2067(8) [11]			
N_K	$(1.21 \pm 0.02_{\text{syst}}) \cdot 10^{11}$			

Table 6.2: *Input values used for the N_K computation in 6.3 in bins of momentum. For explanation of the N_K systematic uncertainty see text.*

of $K_{\pi\pi\pi}$ and $K_{\pi\pi}$ backgrounds. The dominant contribution to the signal inefficiency is the acceptance loss induced by the pion track. Any charged particle produced in the RICH mirrors are detected by this procedure and the event is rejected. The acceptance loss is described in the simulation and is included in the signal acceptance evaluation. The accidental contribution $\eta_{\text{mult}} = (9.7 \pm 2.0_{\text{syst}})\%$ is lower than $\eta_{\phi-\text{loss}}$, as it is unlikely for an accidental hit to appear at the same time and position in all three detectors. A systematic uncertainty of $\pm 2\%$ is assigned to account for a possible bias of the data sample.

The resulting signal efficiency $\epsilon_{\text{RV}} = (75.5 \pm 2.5_{\text{syst}})\%$ is constant over the (15, 35) GeV/c momentum range, because it has a purely accidental origin. Multiplying ϵ_{RV} by the acceptance from Section 6.2 following (6.2) the corresponding $K_{\pi\nu\bar{\nu}}$ efficiency is then $\epsilon_{\pi\nu\bar{\nu}} = (3.0 \pm 0.1_{\text{syst}})\%$. The statistical uncertainty is two orders of magnitude smaller than the systematic one.

6.6 Single event sensitivity (SES)

The branching ratio, which can be obtained from one observed signal event for the case of zero background is called single event sensitivity (SES) and is computed as

$$SES = \frac{1}{N_K \sum\limits_{p \text{ bins } j} \left(\epsilon^j_{\pi\nu\bar{\nu}} \cdot \epsilon^j_{\text{trig}}\right)}, \tag{6.5}$$

using the effective number of kaon decays N_K from (6.3), the $K_{\pi\nu\bar{\nu}}$ efficiency $\epsilon_{\pi\nu\bar{\nu}}$ from (6.2) (including acceptance and multiplicity induced signal loss), and the trigger efficiency of the PNN trigger chain ϵ_{trig}. The last two quantities are computed in each momentum bin j and summed over the four bins to obtain the final result for the SES.

The values of the input variables to the SES and N_K computations are shown in Tables 6.2 and 6.3. The SM value of $BR_{\pi\nu\bar{\nu}} = (8.4 \pm 1.0) \cdot 10^{-11}$ [36] is used.

The value of the SES is dominated by systematic uncertainty. All sources of systematic uncertainties are reported in Table 6.4 and explained in the following:

– Muon-driven losses can affect differently the $K_{\pi\nu\bar{\nu}}$ signal and the $K_{\mu 2}$ data sample used

P_π [GeV/c]	15-20	20-25	25-30	30-35
$A_{\pi\nu\bar{\nu}}$ [%]	0.790(3)	1.245(4)	1.164(4)	0.722(3)
$A_{\pi\nu\bar{\nu}}$ (R1) [%]	0.192(2)	0.299(2)	0.281(2)	0.248(2)
$A_{\pi\nu\bar{\nu}}$ (R2) [%]	0.599(3)	0.950(3)	0.883(3)	0.473(2)
ϵ_{RV} [%]	78.6(1)(13)	78.3(1)(13)	78.5(1)(13)	79.1(1)(13)
ϵ_{trig} [%]	89.8(3)(20)	90.1(3)(20)	87.9(3)(20)	85.1(3)(20)
SES	$(3.15 \pm 0.01_{\mathrm{stat}} \pm 0.24_{\mathrm{syst}}) \cdot 10^{-10}$			
$N^{\mathrm{exp}}_{\pi\nu\bar{\nu}}$[R1, R2]	$0.270 \pm 0.001_{\mathrm{stat}} \pm 0.020_{\mathrm{syst}} \pm 0.032_{\mathrm{ext}}[0.070,\ 0.200]$			

Table 6.3: *Input values used for the SES computation.* R1 and R2 *indicate region* 1 and 2*, respectively. The uncertainties are displayed within brackets, the first being statistical and the second systematic. The external uncertainty on* $N^{exp}_{\pi\nu\bar{\nu}}$ *is due to* $BR_{\pi\nu\bar{\nu}}$ [36].

Source	δSES [10^{-10}]
ϵ_{RV}	± 0.17
m^2_{miss} resolution description	± 0.10
Simulation of π^+ interactions	± 0.09
N_K	± 0.05
Trigger efficiency	± 0.04
Extra activity	± 0.02
Pileup simulation	± 0.02
Momentum spectrum	± 0.01
Total	± 0.24

Table 6.4: *Breakdown of the systematic uncertainties to the Single event sensitivity (SES).*

to measure $\epsilon_{\rm RV}$. The $\epsilon_{\rm RV}$ value is extrapolated down to 0 using the dependence on the instantaneous beam intensity and compared to the $\epsilon_{\rm RV}$ value obtained from $K_{\mu\nu}$ MC. The difference is conservatively assigned as a systematic uncertainty;

– A systematic uncertainty related to the imperfect description of the $m^2_{\rm miss}$ resolution in the MC is considered, which affects the number of normalization events in the $\pi\pi$ region. The uncertainty is estimated by varying the cuts defining the $\pi\pi$ region and comparing the corresponding SES. The maximum variation of 3.2% from the standard definition is taken as a systematic uncertainty;

– An uncertainty is assigned, related to the simulation of the π^+ losses due to the π^0 rejection conditions, driven by pion interactions in the RICH material. The uncertainty is obtained using the $K^{2\gamma{\rm LAV}}_{\pi\pi}$ selection with an additional LAV12 veto, to avoid multiplicity induced by photon conversion in the RICH. The π^+ losses are evaluated for both data and MC. The π^0 rejection losses due to random activity are subtracted using $K_{\mu2}$ decays in data, so only the component induced by the pion interactions in the RICH material is quoted. The losses observed are 9.9% in MC and 13.1% in data. The $K_{\pi\nu\bar{\nu}}$ simulation suggests that signal losses due to π^0 rejection are about 10% in total. Therefore, a systematic uncertainty of 3% is assigned to the signal acceptance and propagated to the SES;

– The N_K value is computed with two different methods: either using the full (15, 35) GeV/c track momentum range or dividing it in four 5 GeV/c wide momentum bins using the bin-dependent acceptance. Th half-difference between the two values is considered as a systematic uncertainty on the description of the π^+ spectrum in the MC. This uncertainty is more than 40 times larger than the statistical error on N_K;

– A systematic uncertainty of 2% is assigned to account for the L1 trigger efficiency correction, as described in Section 6.4;

– The SES is computed using two different values of the $A_{\pi\nu\bar{\nu}}$ and $A_{\pi\pi}$ acceptances, either integrated over the momentum spectrum or as the sum of the acceptances computed in each momentum bin. The half-difference is taken as a systematic uncertainty due to differences in the momentum spectrum between signal and normalization;

– An additional systematic uncertainty is evaluated using MC simulation without pileup for both signal and normalization and adding/removing some cuts on extra-activity in the selection of the normalization that are balanced by a corresponding variation of random veto and normalization acceptance.

The calorimetric (RICH) π^+ identification are reproduced by the MC within 3% (6%). As the particle identification efficiencies are the same within 2% between signal and normalization, any systematic effect is assumed to cancel to first order in the ratio. No systematic uncertainty is assigned due to possible geometry-dependent or intensity-dependent detector efficiencies. The effect is considered as negligible, because the signal and normalization channels illuminate the NA62 detector in a similar way and both PNN and control trigger streams are collected concurrently.

7
Results

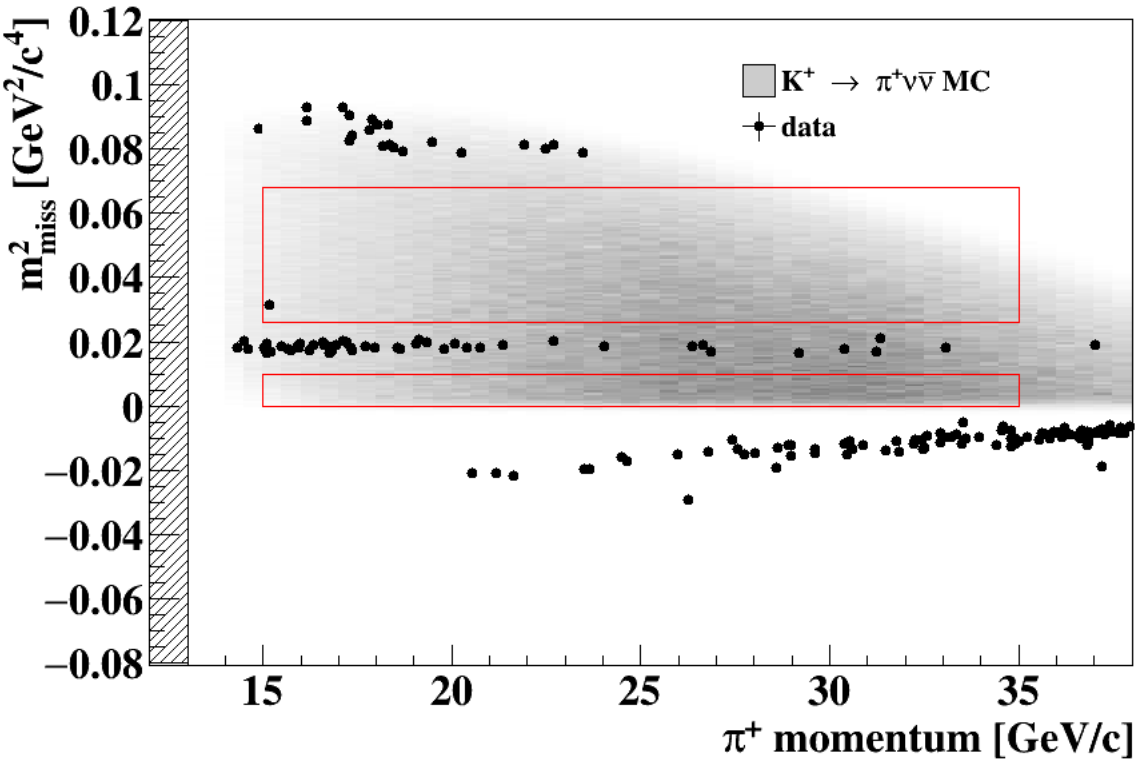

Figure 7.1: m^2_{miss} as a function of P_π for PNN-trigger data events (dots) passing the $K_{\pi\nu\bar{\nu}}$ selection. The gray area corresponds to the distribution of $K_{\pi\nu\bar{\nu}}$ MC events. The red rectangles correspond to the two signal regions. One event is observed in R2.

SES	$(3.15 \pm 0.01_{stat} \pm 0.24_{syst}) \cdot 10^{-10}$
Expected SM $K^+ \to \pi^+\nu\bar{\nu}$	$0.270 \pm 0.001_{stat} \pm 0.020_{syst} \pm 0.032_{ext}$
Expected Background	$0.15 \pm 0.09_{stat} \pm 0.01_{syst}$
Events Observed	1

Table 7.1: *Summary of the results from the $K^+ \to \pi^+\nu\bar{\nu}$ analysis on 2016 data.*

After gathering all ingredients together we are ready to unblind the signal and control regions. One event is observed in the $K_{\mu\nu(\gamma)}$ control region (CR), consistent with the expectation of $0.40 \pm 0.06_{stat} \pm 0.04_{syst}$. One event is observed in the $K_{\pi\pi(\gamma)}$ control region (CR1 + CR2), consistent with the expectation of $1.37 \pm 0.16_{stat} \pm 0.02_{syst}$.

One event is found in R2 after unblinding the signal regions, as shown in Figure 7.1. The particle associated to the $K_{\pi\nu\bar{\nu}}$ candidate has 15.3 GeV/c track momentum and is the one that triggered the event. The signals detected in the LKr, MUV1, MUV2 and RICH detectors clearly indicate that the track is a positively charged pion. The event looks visually close to the edge of the signal region, but the one-dimensional $m^2_{\rm miss}$ comparison between the signal and background profiles (Figure 7.2) clearly shows that signal-to-background ratio is larger than two. The complete information about the observed event can be found in Section A.5 of the appendix. No events are found with m^2_{miss} in the signal regions and momentum below 15 GeV/c or above 35 GeV/c. The Cherenkov threshold for π^+ in the RICH limits the acceptance below 15 GeV/c.

The expected number of SM signal and background events are presented in Table 7.1. The $p-$value of the observed event is 0.067, where the hybrid frequentistic-bayesian prescription described in [103] is applied to account for the uncertainty on the expected background, considering a symmetric uncertainty of ± 0.09 on the expected background. Using the CL$_s$ method [104], the observed upper limit on the $K^+ \to \pi^+\nu\bar{\nu}$ branching ratio is

$$BR(K^+ \to \pi^+\nu\bar{\nu}) < 14 \times 10^{-10} \ @ \ 95 \ \% \ \text{CL}, \tag{7.1}$$

where the corresponding expected limits is $BR(K^+ \to \pi^+\nu\bar{\nu}) < 10 \times 10^{-10}$. The result is compatible with the Standard Model prediction [36]: $BR(K^+ \to \pi^+\nu\bar{\nu}) < (8.4 \pm 1.0) \times 10^{-11}$. To compare with previous measurements, the decay rate is also computed at 68% CL to

$$BR(K^+ \to \pi^+\nu\bar{\nu}) = 28^{+44}_{-23} \times 10^{-11} \ @ \ 68 \ \% \ \text{CL}. \tag{7.2}$$

The obtained branching ratio is in agreement with the previous result $BR(K^+ \to \pi^+\nu\bar{\nu}) < 17.3^{+11.5}_{-10.5} \times 10^{-11}$ quoted by the E949 collaboration [45].

The result presented in this chapter is an important milestone for the NA62 collaboration. It is a proof that the decay-in-flight technique to study the extremely rare kaon decay $K^+ \to \pi^+\nu\bar{\nu}$ works. The acceptance is 20 times larger than the one achieved with the stopped kaon technique [45] and this result is already competitive with just 1% of the total expected NA62 statistics. In the future various improvements are foreseen at analysis level to further reduce backgrounds and enhance signal efficiency. Ongoing studies aim at improving π^+ identification

efficiency, reduce random veto and employ likelihood methods to separate better signal and background. A new final collimator made of iron was installed in June 2018 to remove completely pions from upstream decays entering the decay region. The idea was inspired by the analysis of the upstream background described in this thesis, which showed the geometrical origin of this background. This will increase the signal acceptance by 30% in 2018.

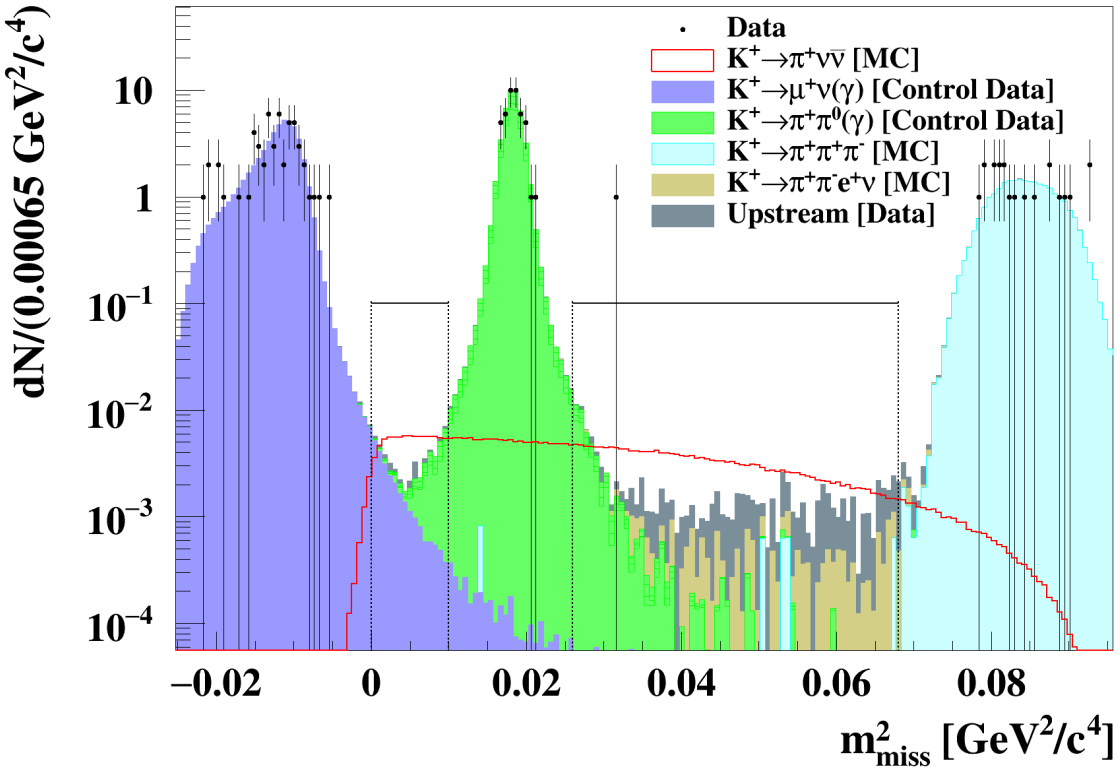

Figure 7.2: *m^2_{miss} distribution for data and expected backgrounds after $K^+ \to \pi^+\nu\bar{\nu}$ selection for events with $15 < P_\pi < 35$ GeV/c. The distributions of $K^+ \to \mu^+\nu_\mu(\gamma)$ and $K^+ \to \pi^+\pi^0(\gamma)$ decays are produced with control data used to measure the m^2_{miss} kinematic tails. Samples from MC simulation are used to model the m^2_{miss} distribution of $K^+ \to \pi^+\pi^+\pi^-$ and $K^+ \to \pi^+\pi^-e^+\nu_e$, selected similar to the signal except the π^0 and the straw segment rejection procedures are not applied. The shape of the m^2_{miss} distribution of upstream events is taken from the bifurcated sample with both Cut1 and Cut2 reversed. The relative normalization of the different components is described in the text.*

A

A.1 $K^+ \to \pi^+\pi^0$ control samples

Control-trigger π^+ tracks are selected from $K_{\pi\pi}$ decays to measure the kinematic tails, particle identification and trigger efficiency. The selection follows closely the $K_{\pi\nu\bar{\nu}}$ signal selection. The events considered are single-track kaon decays selected according to Section 4.4 and rejected for upstream background Section 4.5.1. A positive identification of the π^0 is used to improve the background rejection.

Only π^0 reconstructed in the LKr are considered. A veto is applied in LAV, SAC and IRC according to Section 4.5.4. A π^0 is selected if:

- there are exactly two extra standard LKr clusters reconstructed with $E_\gamma \geq 3$ GeV/c and $d_{\mathrm{DeadCell}} \geq 2$ cm to reject minimum-ionizing particles and avoid clusters passing close to a dead LKr cell;
- both extra clusters are electromagnetic (Section 4.5.2)
- the average time of the two LKr photons T_{π^0} is within ± 5 ns of $\mathrm{T}^{\mathrm{CHOD}}_{\mathrm{track}}$;
- the $m^2_{\mathrm{miss}} = (p_K - p_{\pi^0})^2$ of the π^+ track is in the range (0.008,0.031) GeV$^2/c^4$;
- the longitudinal position of the two-photon vertex $Z^{\pi^0}_{\mathrm{vertex}}$ is between 110 and 165 m;
- the expected π^+ (x, y) position at the subdetector z positions is inside their geometrical acceptances. When extrapolated to the LKr front face the π^+ should be at least 15 cm away from any of the two photons;

The above criteria are referred to as π^0 identification in the following. The samples are divided in several categories depending on the study they are needed for.

$K_{\pi\pi}$ ($\pi^0 \to \gamma\gamma$) control sample : Used to study kinematic tails. The cuts applied are

- π^0 identification;
- positive calorimetric and RICH π^+ identification.

The radiative $K_{\pi\pi(\gamma)}$ decays are not included in this sample.

$\boldsymbol{K^{\mathbf{RICH\ (calo)}}_{\pi\pi}}$ **samples**: Used to estimate the RICH (calorimetric) π^+ identification efficiency. Events are selected if

- the missing mass squared is in within (0.013,0.023) GeV$^2/c^4$;
- the track is positively identified as a π^+ using the calorimeters (RICH) algorithms described in Section 4.5.2(4.5.3).

$\boldsymbol{K^{2\gamma\ \mathbf{calo}}_{\pi\pi}}$ **sample**: Used to estimate the L0COMB and L0RICH trigger efficiency. Two isolated LKr photons are required with no activity in LAV and SAV.

$\boldsymbol{K^{2\gamma\ \mathbf{LAV}}_{\pi\pi}}$ **sample**: Used to estimate the L0CALO trigger efficiency. Events are selected if

- exactly two photons are present in the LAV
- no activity is present in the LKr or SAV.

This is the only sample that does not use the LKr π^0 identification.

A.2 $K^+ \to \mu^+\nu_\mu$ control samples

A control sample of muons is selected from $K_{\mu\nu}$ decays to study kinematic tails, μ^+ rejection capabilities and random veto induced by the π^0 rejection. The events considered are single-track kaon decays selected according to Section 4.4 and rejected for upstream background Section 4.5.1. Several samples are selected in the (15, 35) GeV/c track momentum range.

$\boldsymbol{K^{\mathbf{rveto}}_{\mu\nu}}$ **sample**: Used to estimate the accidental component of the multiplicity induced signal loss. The following criteria are applied

- positive μ^+ identification with RICH and Calorimeters;
- missing mass squared computed using m_{μ^+} must be within $(-0.01,\ 0.01)$ GeV$^2/c^4$.

The background contamination in this sample is negligible.

$\boldsymbol{K_{\mu\nu}}$ **control sample**: Used to estimate the $K_{\mu\nu}$ kinematic tails. The following criteria are applied

- positively identified μ^+ using the Calorimeters;
- photon rejection using LKr, LAV, SAC, IRC;
- track momenta must be within (15, 35) GeV/c.

No RICH identification is used, because the $K_{\mu\nu}$ kinematic tails entering R1 are caused by wrong RICH identification. If the RICH is used for μ^+ identification, only well measured μ^+ will be selected, therefore biasing the kinematic rejection measurement. This sample includes tails from non-gaussian resolution and $K_{\mu\nu(\gamma)}$ decays.

$\boldsymbol{K^{\mathbf{RICH\ (calo)}}_{\mu\nu}}$ **samples**: Used to estimate the RICH (calorimetric) μ^+ rejection. Events are considered if

- the missing mass squared computed using m_{μ^+} must be within $(-0.01,\ 0.01)$ GeV$^2/c^4$.
- the track is positively identified as μ^+ using both RICH and Calorimeters.

A.3 $K^+ \to \pi^0 e^+ \nu_e$ control sample

Control-trigger e^+ tracks are selected from K_{e3} decays to measure particle identification performance with positrons. The selection follows closely the $K_{\pi\nu\bar{\nu}}$ signal selection. The events considered are single-track kaon decays selected according to Section 4.4 and rejected for upstream background Section 4.5.1. Positive identification of the π^0 is used as in Section A.1 with both π^0 photons detected by the LKr. No signals in LAV, IRC and SAC and MUV3 are allowed.

A.4 $K^+ \to \pi^+\pi^+\pi^-$ control sample

Control-trigger $K_{\pi\pi\pi}$ decays are selected, used to study the efficiency for the GTK - STRAW track association. The selection is entirely based on the $K_{\pi\pi\pi}$ kinematics with the following conditions applied:

- all three tracks to be inside the geometrical acceptance of the four STRAW chambers, CHOD, NA62CHOD, LKr and MUV3;
- exactly three track reconstructed by the STRAW detector, each with momentum higher than 10 GeV/c;
- the sum of the charges of the three tracks has to be +1;
- the reconstructed three-track vertex must have a longitudinal position inside the fiducial decay region $105 - 165$ m;
- each track to have matching in the CHOD, NA62CHOD and the LKr, following the procedure described in Section 4.2;

A.5 $K^+ \to \pi^+\nu\bar{\nu}$ candidate decay event characteristics

The observed event in R2 has two L0 primitives in the RICH separated by about 17 ns. One is responsible for the positive L0 trigger condition, the other one with a primitive in coincidence in MUV3. These primitives correspond to two particles reconstructed offline. The event was triggered by the particle associated to the $K^+ \to \pi^+\nu\bar{\nu}$ candidate and its characteristics are shown in Table A.1. The event display in CHOD, LKr and RICH are shown in Figures A.1, A.2, A.3. The additional downstream particle is reconstructed offline 17 ns from the $K_{\pi\nu\bar{\nu}}$ candidate. The track has 48 GeV/c momentum and associated signals in the RICH, CHOD, LKr and MUV3 detectors. The track is consistent with an accidental μ^+.

Trigger	
RICH primitive time [ns]	0.
CHOD primitive time [ns]	0.390
NA62CHOD primitive time [ns]	2.047
K^+	
KTAG, GTK time [ns]	16.012, 16.006
Number of KTAG sectors	7
K^+ momentum [GeV/c]	75.440
K^+ dX/dZ, $dYdZ$ [mrad]	1.199, 0.088
π^+	
STRAW, RICH, CHOD, LKr time [ns]	22.256, 16.052, 16.141, 15.389
π^+ momentum [GeV/c]	15.38
π^+ dX/dZ, $dYdZ$ [mrad]	9.781, -0.917
π^+ position (X,Y) at Trim5; CHOD; LKr [mm]	$(-372.6, 29.8)$; $(240.5, -89.5)$; $(224.6, -91.1)$
RICH radius [mm], mass [GeV/c^2], likelihood	112.06, 0.1378, 1
Energy in LKr, MUV1, MUV2 [GeV]	7.9, 1.8, 0.5
Pion probability in calorimeters	0.99836
Event Kinematics	
m^2_{miss}, $m^2_{\text{miss, RICH}}$, $m^2_{\text{miss, beam}}$ [GeV^2/c^4]	0.03144, 0.03084, 0.03296
Vertex position Z, X, Y [mm]	146216, 62.34, -10.0
Vertex quality: CDA [mm], KTAG-GTK discriminant	1.7, 0.36

Table A.1: *Summary of the $K^+ \to \pi^+ \nu\overline{\nu}$ decay event candidate found in R2.*

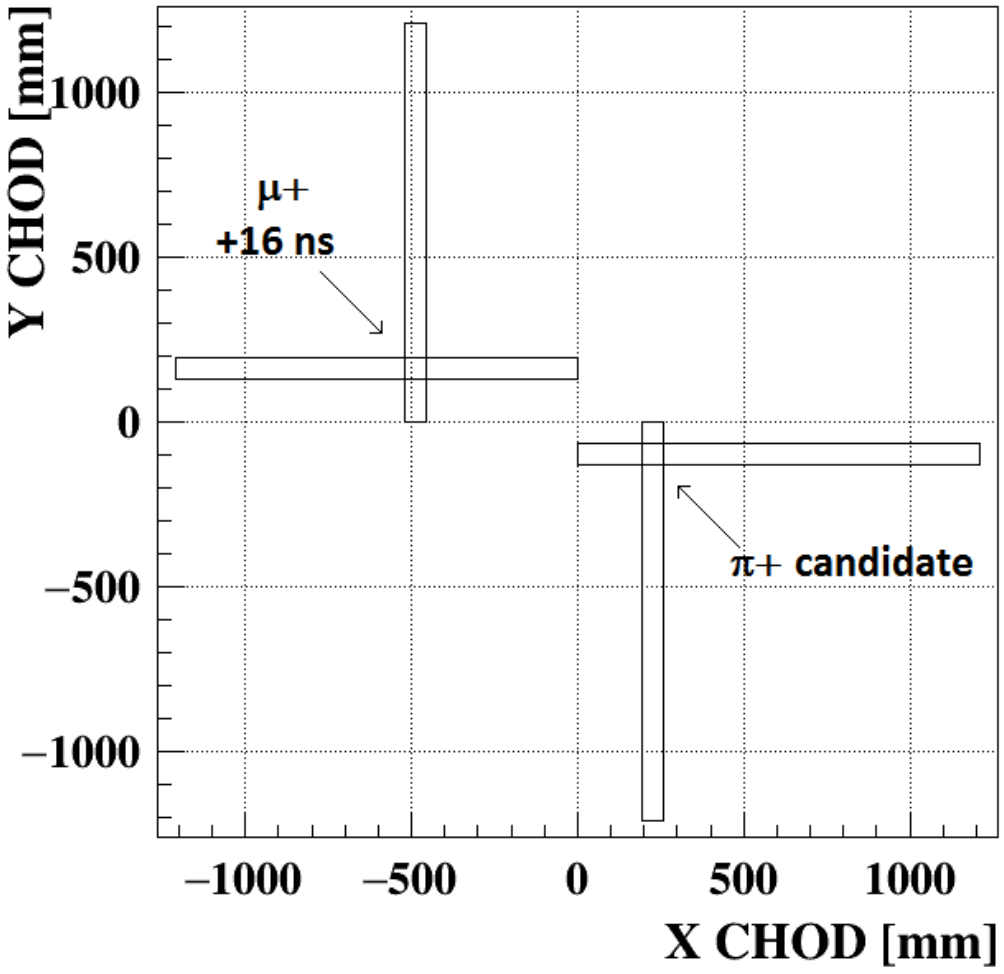

Figure A.1: *CHOD display of the $K^+ \to \pi^+\nu\overline{\nu}$ decay event candidate found in R2.*

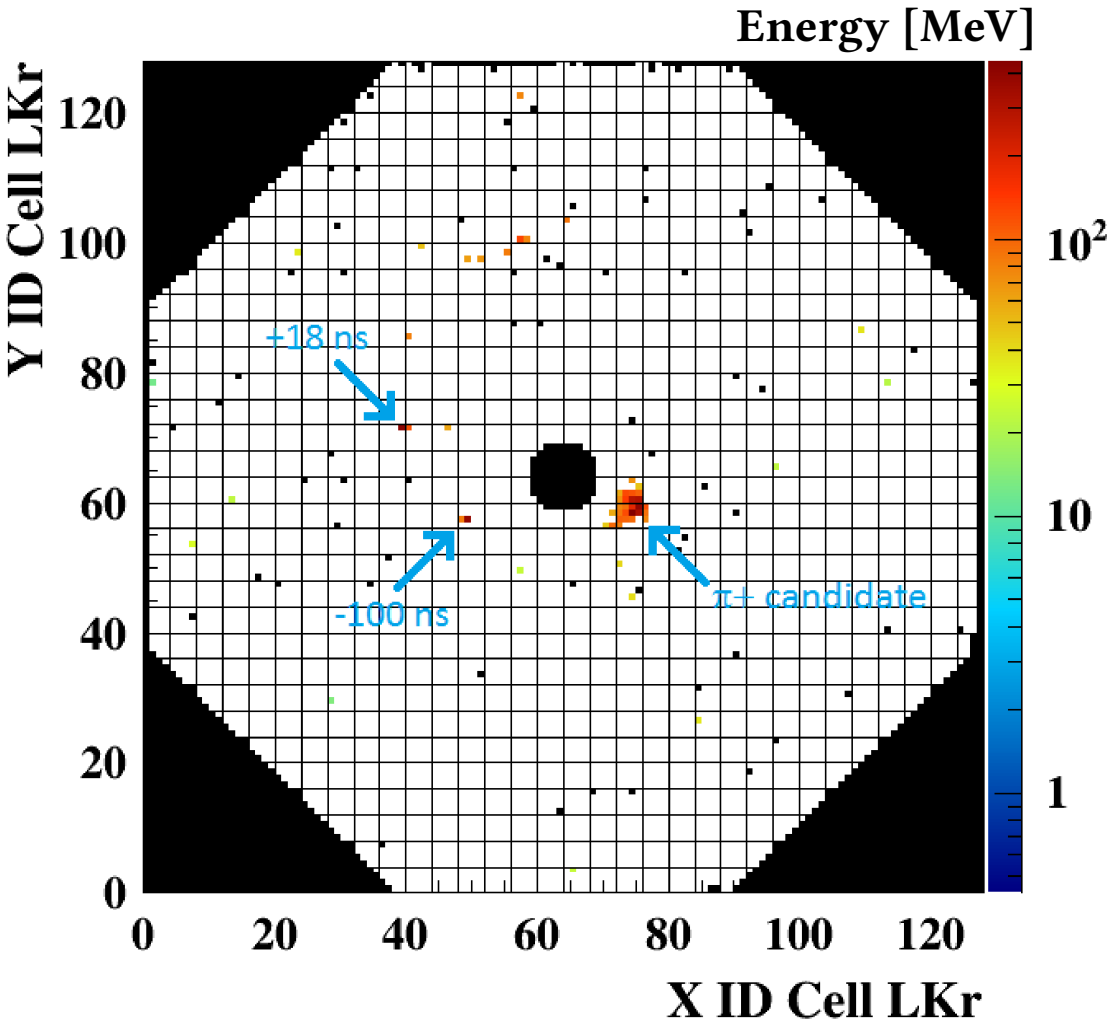

Figure A.2: *LKr display of the $K^+ \to \pi^+ \nu\overline{\nu}$ decay event candidate found in R2.*

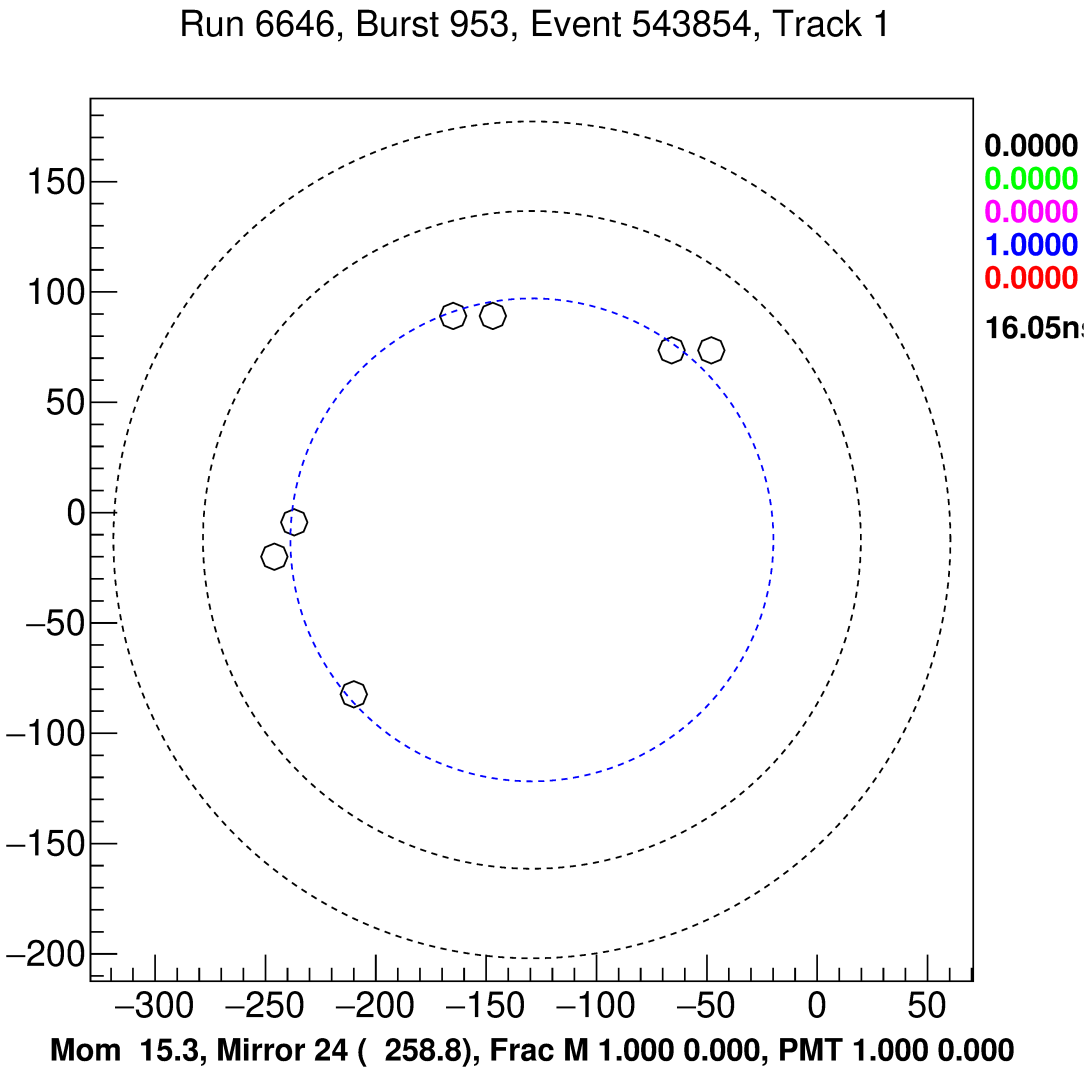

Figure A.3: *Position of the hits in the RICH forming the ring associated to the π^+ track in the observed event in R2, given by the RICH event display. The circles illustrate the positron, muon and pion hypothesis, showing a perfect agreement with the pion hypothesis (the innermost ring).*

References

[1] G. D. Rochester and C. C. Butler, *Evidence for the existence of new unstable elementary particles*, *Nature* **160** (1947) 855.

[2] S. L. Glashow, *Partial-symmetries of weak interactions*, *Nucl. Phys.* **22** (1961) 579 .

[3] S. Weinberg, *A Model of Leptons*, *Phys. Rev. Lett.* **19** (1967) 1264.

[4] A. Salam, *Weak and electromagnetic interactions*, in *8th Nobel Symposium Lerum, Sweden, May 19-25, 1968*, vol. C680519, pp. 367–377, 1968, inspirehep.net/record/53083.

[5] P. W. Higgs, *Broken Symmetries and the Masses of Gauge Bosons*, *Phys. Rev. Lett.* **13** (1964) 508.

[6] F. Englert and R. Brout, *Broken Symmetry and the Mass of Gauge Vector Mesons*, *Phys. Rev. Lett.* **13** (1964) 321.

[7] F. Halzen and A. D. Martin, *Quarks and Leptons: An introductory course in modern particle physics*. (1984).

[8] P. Langacker, *The Standard Model and beyond*. (2010).

[9] J. Charles et al., *CP violation and the CKM matrix: assessing the impact of the asymmetric B factories*, *Eur. Phys. J.* **C 41** (2005) 1.

[10] S. L. Glashow et al., *Weak Interactions with Lepton-Hadron Symmetry*, *Phys. Rev.* **D 2** (1970) 1285.

[11] M. Tanabashi et al., *Review of Particle Physics*, *Chin. Phys.* **C 98** (2018) .

[12] M. Kobayashi and T. Maskawa, *CP-Violation in the Renormalizable Theory of Weak Interaction*, *Progress of Theoretical Physics* **49** (1973) 652.

[13] L. Wolfenstein, *Parametrization of the Kobayashi-Maskawa Matrix*, *Phys. Rev. Lett.* **51** (1983) 1945.

[14] S. Descotes-Genon and P. Koppenburg, *The CKM Parameters*, *Annual Review of Nuclear and Particle Science* **67** (2017) 97.

[15] A. J. Buras, *Weak Hamiltonian, CP violation and rare decays*, in *Probing the standard model of particle interactions. Proceedings, Summer School in Theoretical Physics, Les Houches, France*, pp. 281–539, 1998, hep-ph/9806471.

[16] K. G. Wilson, *Non-Lagrangian Models of Current Algebra*, *Phys. Rev.* **179** (1969) 1499.

[17] K. G. Wilson and W. Zimmermann, *Operator product expansions and composite field operators in the general framework of quantum field theory*, *Comm. in Math. Phys.* **24** (1972) 87.

[18] E. C. G. Sugarshan and R. E. Marshak, *Development of the Theory of Weak Interaction*, in *Proc. Padua-Venice Conf*, 1957.

[19] R. P. Feynman and M. Gell-Mann, *Theory of the Fermi Interaction*, *Phys. Rev.* **109** (1958) 193.

[20] M. Gell-Mann and F. E. Low, *Quantum Electrodynamics at Small Distances*, *Phys. Rev.* **95** (1954) 1300.

[21] K. Symanzik, *Small distance behaviour in field theory and power counting*, *Comm. Math. Phys.* **18** (1970) 227.

[22] C. G. Callan, *Broken Scale Invariance in Scalar Field Theory*, *Phys. Rev.* **D 2** (1970) 1541.

[23] G. 't Hooft, *Dimensional regularization and the renormalization group*, *Nucl. Phys.* **B 61** (1973) 455 .

[24] S. Weinberg, *New Approach to the Renormalization Group*, *Phys. Rev.* **D 8** (1973) 3497.

[25] K. G. Wilson, *Confinement of quarks*, *Phys. Rev.* **D 10** (1974) 2445.

[26] S. Weinberg, *Phenomenological Lagrangians*, *Physica A: Statistical Mechanics and its Applications* **96** (1979) 327 .

[27] J. Gasser and H. Leutwyler, *Chiral perturbation theory: Expansions in the mass of the strange quark*, *Nucl. Phys.* **B 250** (1985) 465 .

[28] A. J. Buras et al., *Waiting for precise measurements of* $K^+ \to \pi^+ \nu\overline{\nu}$ *and* $K_L \to \pi^0 \nu\overline{\nu}$, *Rev. Mod. Phys.* **80** (2008) 965.

[29] V. Cirigliano et al., *Kaon decays in the standard model*, *Rev. Mod. Phys.* **84** (2012) 399.

[30] O. I. Dahl et al., *Strange-Particle Production in* $\pi^- p$ *Interactions from 1.5 to 4.2 GeV/c. II. Two-Body Final States*, *Phys. Rev.* **183** (1969) 1520.

[31] M. K. Gaillard and B. W. Lee, *Rare decay modes of the K mesons in gauge theories*, *Phys. Rev.* **D 10** (1974) 897.

[32] J. Ellis et al., *Implications of recent measurements of B meson mixing and* ϵ'/ϵ_K, *Nucl. Phys.* **B 304** (1988) 205 .

[33] G. Buchalla and A. J. Buras, $K \to \pi\nu\overline{\nu}$ *and high precision determinations of the CKM matrix*, *Phys. Rev.* **D 54** (1996) 6782.

[34] F. Mescia and C. Smith, *Improved estimates of rare K decay matrix elements from* $K_{\ell 3}$ *decays*, *Phys. Rev.* **D 76** (2007) 034017.

[35] J. Brod et al., *Two-loop electroweak corrections for the $K \to \pi\nu\overline{\nu}$ decays*, *Phys. Rev.* **D 83** (2011) 034030.

[36] A. J. Buras et al., *$K^+ \to \pi^+\nu\overline{\nu}$ and $K_L \to \pi^0\nu\overline{\nu}$ in the Standard Model: status and perspectives*, *JHEP* **2015** (2015) 33.

[37] U. Camerini et al., *Experimental Search for Semileptonic Neutrino Neutral Currents*, *Phys. Rev. Lett.* **23** (1969) 326.

[38] J. H. Klems et al., *Limits on the $K^+ \to \pi^+ + \nu + \overline{\nu}$ and $K^+ \to \pi^+ + n\gamma$ Decay Rates*, *Phys. Rev.* **D 4** (1971) 66.

[39] G. D. Cable et al., *Search for Rare K^+ Decays. II. $K^+ \to \pi^+\nu\overline{\nu}$*, *Phys. Rev.* **D 8** (1973) 3807.

[40] Y. Asano et al., *Search for a rare decay mode $K^+ \to \pi^+\nu\overline{\nu}$ and axion*, *Phys. Lett.* **D 107** (1981) 159 .

[41] M. S. Atiya et al., *Search for the decay $K^+ \to \pi^+\nu\overline{\nu}$*, *Phys. Rev. Lett.* **64** (1990) 21.

[42] M. S. Atiya et al., *Search for the Decay $K^+ \to \pi^+\nu\overline{\nu}$*, *Phys. Rev. Lett.* **70** (1993) 2521.

[43] S. Adler et al., *Search for the Decay $K^+ \to \pi^+\nu\overline{\nu}$*, *Phys. Rev. Lett.* **76** (1996) 1421.

[44] A. Artamonov et al., *New Measurement of the $K^+ \to \pi^+\nu\overline{\nu}$ Branching Ratio*, *Phys. Rev. Lett.* **101** (2008) 191802.

[45] A. Artamonov et al., *Study of the decay $K^+ \to \pi^+\nu\overline{\nu}$ in the momentum region $140 < P_\pi < 199$ MeV/c*, *Phys. Rev.* **D 79** (2009) 092004.

[46] J. J. Aubert et al., *Experimental observation of a heavy particle J*, *Phys. Rev. Lett.* **33** (1974) 1404.

[47] J. E. Augustin et al., *Discovery of a narrow resonance in e^+e^- annihilation*, *Phys. Rev. Lett.* **33** (1974) 1406.

[48] C. Albajar et al., *Search for $B^0 - \overline{B^0}$ oscillations at the CERN proton-antiproton collider*, *Phys. Lett.* **B 186** (1987) 247 .

[49] A. Albrecht et al., *Observation of $B^0 - \overline{B^0}$ mixing*, *Phys. Lett.* **B 192** (1987) 245 .

[50] F. Abe et al., *Observation of Top Quark Production in $\overline{p}p$ Collisions with the Collider Detector at Fermilab*, *Phys. Rev. Lett.* **74** (1995) 2626.

[51] G. Buchalla and A. J. Buras, *The rare decays $K \to \pi\nu\overline{\nu}$, $B \to X\nu\overline{\nu}$ and $K \to l^+l^-$: an update*, *Nucl. Phys.* **B 548** (1999) 309 .

[52] J. Brod and M. Gorbahn, *Electroweak corrections to the charm quark contribution to $K^+ \to \pi^+\nu\overline{\nu}$*, *Phys. Rev.* **D 78** (2008) 034006.

[53] G. Isidori et al., *Light-quark loops in $K^+ \to \pi\nu\overline{\nu}$*, *Nucl. Phys.* **B 718** (2005) 319 .

[54] A. J. Buras et al., *Charm quark contribution to $K^+ \to \pi^+ \nu\bar{\nu}$ at next-to-next-to-leading order*, *JHEP* **11** (2006) 002.

[55] A. J. Buras et al., *$K \to \pi\nu\bar{\nu}$ and ϵ'/ϵ in simplified new physics models*, *JHEP* **2015** (2015) 166.

[56] P. Langacker, *The physics of heavy Z' gauge bosons*, *Rev. Mod. Phys.* **81** (2009) 1199.

[57] M. Bordone et al., *Probing lepton-flavour universality with $K \to \pi\nu\bar{\nu}$ decays*, *Eur. Phys. J.* **C 77** (2017) 618.

[58] D. Buttazzo et al., *B-physics anomalies: a guide to combined explanations*, *JHEP* **2017** (2017) 44.

[59] R. Aaij et al., *Test of Lepton Universality Using $B^+ \to K^+ \ell^+ \ell^-$ Decays*, *Phys. Rev. Lett.* **113** (2014) 151601.

[60] R. Aaij et al., *Measurement of the Ratio of the $B^0 \to D^{*-} \tau^+ \nu_\tau$ and $B^0 \to D^{*-} \mu^+ \nu_\mu$ Branching Fractions Using Three-Prong τ-Lepton Decays*, *Phys. Rev. Lett.* **120** (2018) 171802.

[61] C. Lazzeroni et al., *Precision measurement of the ratio of the charged kaon leptonic decay rates*, *Phys. Lett.* **B 719** (2013) 326 .

[62] M. Blanke et al., *Rare K and B decays in a warped extra dimension with custodial protection*, *JHEP* **2009** (2009) 108.

[63] M. Blanke et al., *Quark flavour observables in the Littlest Higgs model with T-parity after LHC Run 1*, *Eur. Phys. J.* **C 76** (2016) 182.

[64] T. Blažek and P. Maták, *Left–left squark mixing, $K^+ \to \pi^+ \nu\bar{\nu}$ and minimal supersymmetry with large* $\tan\beta$, *Int. J. of Mod. Phys.* **A 29** (2014) 1450162.

[65] G. Isidori et al., *Exploring the flavour structure of the MSSM with rare K decays*, *JHEP* **2006** (2006) 064.

[66] S. Fajfer et al., *Footprints of leptoquarks: from $R_{K^{(*)}}$ to $K \to \pi\nu\bar{\nu}$*, *Eur. Phys. J.* **C 78** (2018) 275 [1802.00786].

[67] A. Crivellin et al., *Importance of Loop Effects in Explaining the Accumulated Evidence for New Physics in B Decays with a Vector Leptoquark*, 1807.02068.

[68] Cortina Gil, E. and others, *The beam and detector of the NA62 experiment at CERN*, *JINST* **12** (2017) P05025.

[69] C. Bovet et al., *The CEDAR counters for particle identification in the SPS secondary beams: a description and an operation manual*, 1982. CERN-82-13.

[70] M. Fiorini et al., *High rate particle tracking and ultra-fast timing with a thin hybrid silicon pixel detector*, *Nucl. Instr. Meth.* **A 718** (2013) 270.

[71] F. Ambrosino et al., *CHANTI: a fast and efficient charged particle veto detector for the NA62 experiment at CERN*, *JINST* **11** (2016) P03029.

[72] Ahmet, K. and others, *The OPAL detector at LEP*, *Nucl. Instr. Meth.* **A 305** (1991) 275.

[73] V. Fanti et al., *The beam and detector for the NA48 neutral kaon CP-violation experiment at CERN*, *Nucl. Instr. Meth.* **A 574** (2007) 433.

[74] NA62 Framework, 2018. https://na62-sw.web.cern.ch/doxygen.

[75] S. Agostinelli et al., *Geant4-a simulation toolkit*, *Nucl. Instr. Meth.* **A 506** (2003) 250 .

[76] B. Sciascia and FlaviaNet Kaon Working Group, *Precision tests of the Standard Model with leptonic and semileptonic kaon decays*, *Nucl. Phys.* **B 181-182** (2008) 83 .

[77] J. D. Good, *Pion Spectrum in Radiative $K_{\pi}{}^{+}$ Decay*, *Phys. Rev.* **113** (1959) 352.

[78] N. Christ, *Possible* CP *Violation in $K^{\pm} \to \pi^{\pm}\pi^{0}\gamma$*, *Phys. Rev.* **159** (1967) 1292.

[79] M. McGuigan and A. I. Sanda, *$K \to \pi\pi\gamma$ in the six-quark model*, *Phys. Rev.* **D 36** (1987) 1413.

[80] J. Bijnens et al., *Radiative semileptonic kaon decays*, *Nucl. Phys.* **B 396** (1993) 81 .

[81] C.-H. Chen et al., *Analysis of $K^{+} \to e^{+}\nu_{e}\gamma$ in light-front quark model and chiral perturbation theory of order p^{6}*, *Phys. Rev.* **D 77** (2008) 014004.

[82] C. Gatti, *Monte Carlo simulation for radiative kaon decays*, *Eur. Phys. J.* **C 45** (2006) 417.

[83] V. Cirigliano et al., *Radiative corrections to K_{l3} decays*, *Eur. Phys. J.* **C 23** (2002) 121.

[84] J. R. Batley et al., *Precise tests of low energy QCD from $K^{\pm} \to \pi^{+}\pi^{-}e^{\pm}\nu(K_{e4})$ decay properties*, *Eur. Phys. J.* **C 70** (2010) 635.

[85] E. Barberio and Z. Was, *PHOTOS - a universal Monte Carlo for QED radiative corrections: version 2.0*, *Comp. Phys. Comm.* **79** (1994) 291 .

[86] G. D'Ambrosio and J. Portoles, *Unitarity and vector meson contributions to $K^{+} \to \pi^{+}\gamma\gamma$*, *Phys. Lett.* **B395** (1997) 389.

[87] C. Lazzeroni et al., *Technical Design Report*, July 2010. https://na62.web.cern.ch/na62/Documents/TD_Full_doc_v10.pdf.

[88] A. Sturgess, "NA62 meeting", *Track Momentum Corrrections*, Mar. 2016. https://indico.cern.ch/event/508889/.

[89] R. Veenhof, *Garfield - simulation of gaseous detectors.* http://garfield.web.cern.ch/garfield.

[90] R. E. Kalman, *A New Approach to Linear Filtering and Prediction Problems*, *J. of B. Eng.* **D 82** (1960) .

[91] J. Engelfried, *RICH Likelihoods in NA62, "NA62 meeting"*, Oct. 2015. https://indico.cern.ch/event/452212/.

[92] R. Volpe, *RICH single-ring fit, "NA62 meeting"*, Nov. 2016. https://indico.cern.ch/event/586936/.

[93] V. Duk, *RICH standalone sing-ring fit, "NA62 meeting"*, Nov. 2016. https://indico.cern.ch/event/589944/.

[94] G. Anzivino et. al., *Precise Alignment of the RICH Mirror System of the NA62 Experiment, "NA62 Note"*. https://na62.web.cern.ch/na62/restricted/NotesDoc/NA62-17-03.pdf.

[95] G. Unal, *Reconstruction program for the LKr, "NA62 meeting"*. https://na62.web.cern.ch/na62/restricted/NotesDoc/NA62_15_02.pdf.

[96] R. Aliberti, *Particle identification with the NA62 calorimeters, "NA62 meeting"*, Aug. 2017. https://indico.cern.ch/event/674013/.

[97] M. Perrin-Terrin, *GigaTrackerEvtReco class, "NA62 framework"*. https://na62-sw.web.cern.ch/doxygen.

[98] G.Ruggiero, *Kaon - Pion matching ,"NA62 meeting"*, May 2017. https://indico.cern.ch/event/641378/.

[99] R. Brun and F. Rademakers, *ROOT: An object oriented data analysis framework*, *Nucl. Instr. Meth.* **A 389** (1997) 81.

[100] L.Peruzzo, *Photon efficiency and π^0 rejection, "NA62 meeting"*, Feb. 2018. https://indico.cern.ch/event/703625/contributions/2888904/attachments/1596867/2529872/PhysicsPeruzzo.pdf.

[101] J.Swallow, *Study of the kinematic rejection of $K_{3\pi}$ background decays, "NA62 Note"*. https://na62.web.cern.ch/na62/restricted/NotesDoc/NA62-18-01.pdf.

[102] A. Romano, *L1 trigger efficiency measurement for $K^+ \to \pi^+ \nu\bar{\nu}$, "NA62 meeting"*, Oct. 2017. https://indico.cern.ch/event/674013/contributions/2757487/attachments/1542957/2420473/L1Trigger_PNNWKG_181017.pdf.

[103] R. D. Cousins, J. T. Linnemann and J. Tucker, *Evaluation of three methods for calculating statistical significance when incorporating a systematic uncertainty into a test of the background-only hypothesis for a Poisson process*, *Nucl. Instr. Meth.* **A 595** (2008) 480 .

[104] A. L. Read, *Presentation of search results: the CL_s technique*, *J. of Phys.* **G 28** (2002) 2693.